nature methods

Article

https://doi.org/10.1038/s41592-022-01743-5

Video-based pooled screening yields improved far-red genetically encoded voltage indicators

Received: 28 April 2022

Accepted: 28 November 2022

Published online: 09 January 2023

Check for updates

He Tian[1], Hunter C. Davis[1], J. David Wong-Campos[1], Pojeong Park[1], Linlin Z. Fan[2], Benjamin Gmeiner[1], Shahinoor Begum[1], Christopher A. Werley[3], Gabriel B. Borja[3], Hansini Upadhyay[3], Himali Shah[3], Jane Jacques[3], Yitong Qi[1], Vicente Parot[1,4], Karl Deisseroth[2,5] & Adam E. Cohen[1,6]

Video-based screening of pooled libraries is a powerful approach for directed evolution of biosensors because it enables selection along multiple dimensions simultaneously from large libraries. Here we develop a screening platform, Photopick, which achieves precise phenotype-activated photoselection over a large field of view (2.3 × 2.3 mm, containing >10^3 cells, per shot). We used the Photopick platform to evolve archaerhodopsin-derived genetically encoded voltage indicators (GEVIs) with improved signal-to-noise ratio (QuasAr6a) and kinetics (QuasAr6b). These GEVIs gave improved signals in cultured neurons and in live mouse brains. By combining targeted in vivo optogenetic stimulation with high-precision voltage imaging, we characterized inhibitory synaptic coupling between individual cortical NDNF (neuron-derived neurotrophic factor) interneurons, and excitatory electrical synapses between individual hippocampal parvalbumin neurons. The QuasAr6 GEVIs are powerful tools for all-optical electrophysiology and the Photopick approach could be adapted to evolve a broad range of biosensors.

Genetically encoded biosensors can dramatically advance our understanding of in vivo neural dynamics[1–3], but the development of improved biosensors is often laborious[4,5]. Dynamic parameters such as signal-to-noise ratio (SNR), sensitivity and kinetics are critical for sensor performance. Generally, there is a trade-off between the throughput of a screening system and the richness of information obtained from each variant. On the one hand, pooled screens such as fluorescence-activated cell sorting (FACS) can readily probe libraries of size > 10^6 but they assess only static parameters and thus are ill-suited for the development of dynamic sensors. On the other hand, arrayed screens are compatible with information-rich, video-based readout but require cloning of individually isolated and sequenced variants. Automated microscopy of pooled libraries, followed by optically targeted selection, has recently emerged as a promising strategy for large-scale screens of complex phenotypes[6–11].

Genetically encoded voltage indicators (GEVIs) can report membrane voltage in vivo[8,12–24], and there is substantial interest in improving their performance. A screen of GEVIs must overcome several challenges. First, for transmembrane proteins such as GEVIs, trafficking and protein function often differ substantially between bacteria and

[1]Department of Chemistry and Chemical Biology, Harvard University, Cambridge, MA, USA. [2]Department of Bioengineering, Department of Psychiatry and Behavioral Sciences, Stanford University, Stanford, CA, USA. [3]Q-State Biosciences, Cambridge, MA, USA. [4]Institute for Biological and Medical Engineering, Pontificia Universidad Católica de Chile, Santiago, Chile. [5]Howard Hughes Medical Institute, Chevy Chase, MA, USA. [6]Department of Physics, Harvard University, Cambridge, MA, USA. e-mail: cohen@chemistry.harvard.edu

https://doi.org/10.1038/s41592-022-01743-5

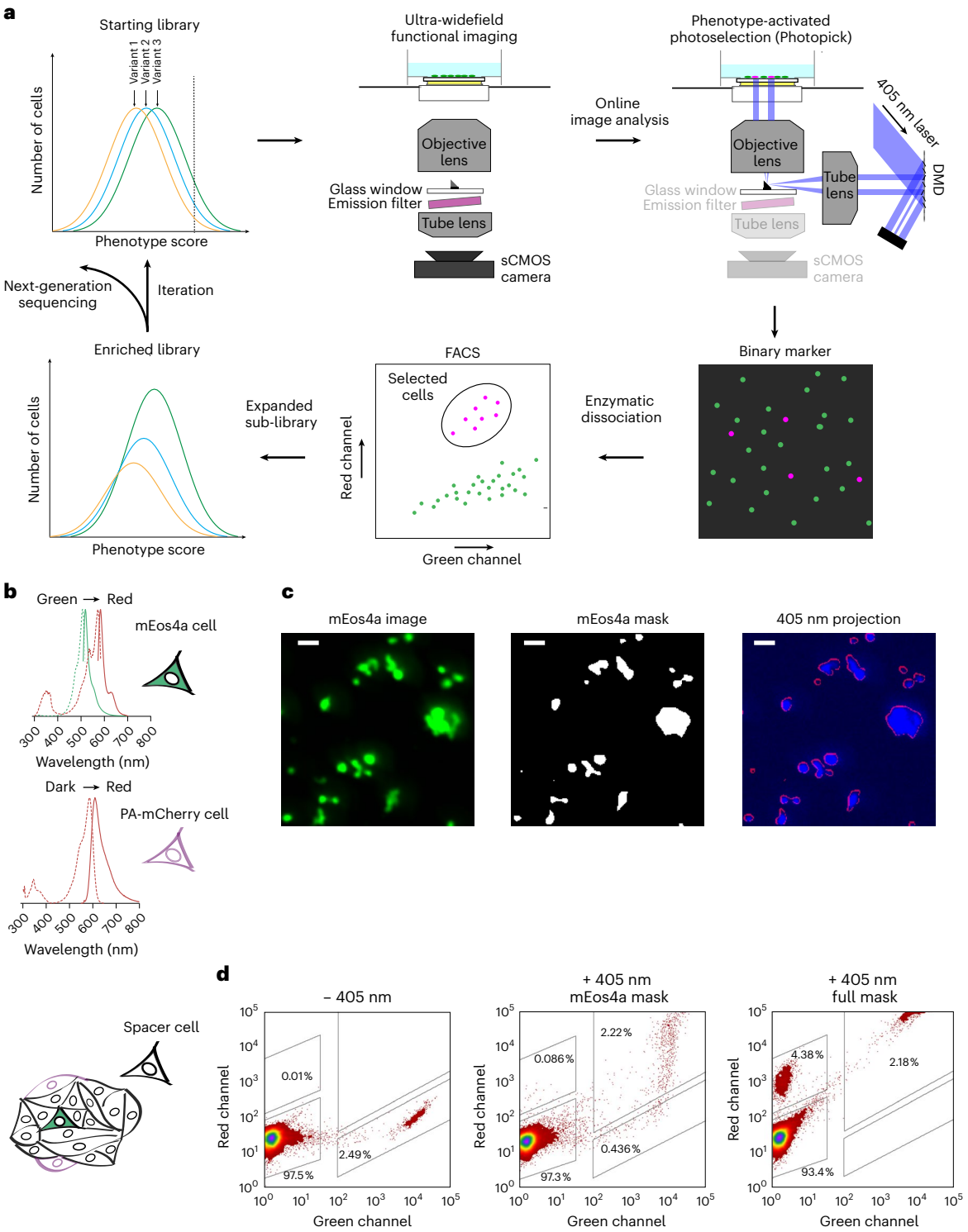

Fig. 1 | Photopick enables video-based pooled screening in mammalian cells. **a**, Photopick comprises a video-based pooled screening pipeline for enrichment of sensor variants with improved performance. **b**, Spectra of phototaggable fluorescent proteins, mEos4a and PA-mCherry, used to validate the optical targeting system. Spectra from FPbase[61]. **c**, Selective phototagging of mEos4a$^+$ cells in a hybrid monolayer of mEos4a$^+$, PA-mCherry$^+$ and non-fluorescent HEK cells. Scale bars, 50 µm. **d**, FACS analyses on the efficiency and fidelity of photoselection (green channel: excitation at 488 nm; red channel: excitation at 561 nm; $n = 2$ trials).

mammalian cells[25]; therefore, it is preferable to screen in mammalian cells. Second, testing of GEVIs requires the induction of reliable membrane potential changes, a challenging task in most stable cell lines. For these reasons, GEVIs are a challenging target for screening.

Here, we present a video-based pooled screening platform that combines ultra-widefield imaging and a phenotype-activated photoselection scheme (Photopick) in mammalian cells. We used this platform to develop new archaerhodopsin 3 (Arch)-derived GEVIs that showed improved SNR (QuasAr6a) and kinetics (QuasAr6b) in cultured neurons and in live mouse brains.

A unique advantage of Arch-derived GEVIs is that they can be combined with blue-shifted channelrhodopsins for simultaneous recording

https://doi.org/10.1038/s41592-022-01743-5

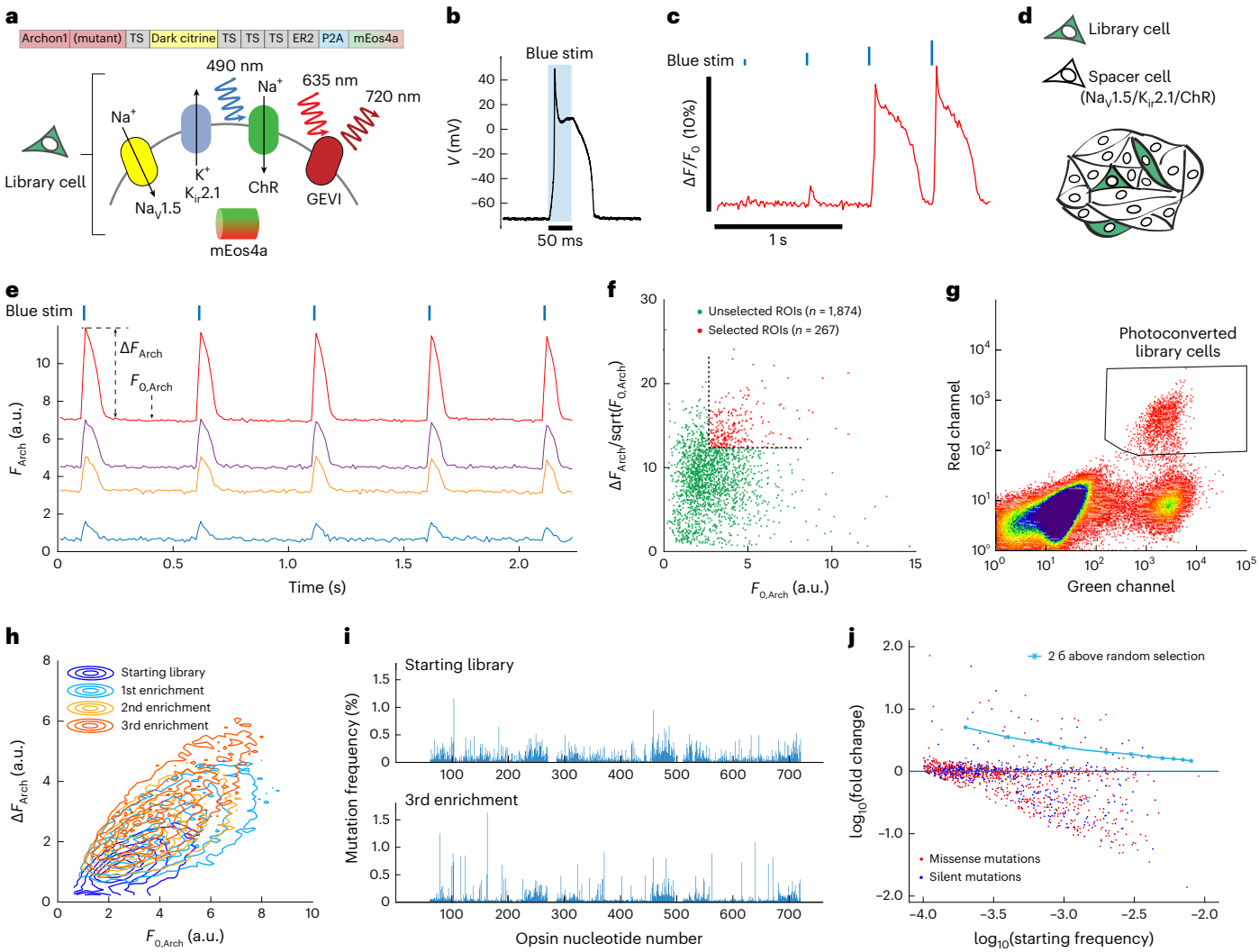

Fig. 2 | Directed evolution of an archaerhodopsin-derived genetically encoded voltage indicator. a, Genetic composition of the library cells. Spiking HEK cells contain a candidate GEVI mutant, channelrhodopsin (ChR) actuator, mEos4a phototag, and $Na_V1.5$ and $K_{ir}2.1$ to enable electrical excitation. Here, TS is the trafficking sequence from $K_{ir}2.1$ (ref. [62]), ER2 is the endoplasmic reticulum export motif from $K_{ir}2.0$ (refs. [63,64]) and P2A is a self-cleaving peptide. **b**, Optogenetically triggered spike of the spiking HEK cell, recorded via whole-cell patch clamp (excitation at 488 nm, 4.4 mW mm^{-2}; see also Extended Data Fig. 2a). Stim, stimulation. **c**, Threshold response of spiking HEK cells to 10 ms increasing optogenetic stimulus strengths, visualized with the voltage-sensitive dye BeRST1 (excitation at 635 nm). **d**, Sample preparation for pooled screening. Library cells were mixed with electrically excitable but non-fluorescent and optically inert spacer cells in approximately a 1:10 ratio. **e**, Examples of fluorescence traces extracted from individual sources in a pooled library screen (Arch fluorescence channel). Precisely timed spikes were evoked by blue light stimulation (blue ticks, excitation at 490 nm, 10 ms). ΔF_{Arch} is calculated as the average baseline-to-peak difference in Arch-channel fluorescence and $F_{0,Arch}$ is the average baseline fluorescence. For the details of image segmentation, see Extended Data Fig. 3c. **f**, Scatter plot of $\Delta F_{Arch}/\sqrt{F_{0,Arch}}$ versus $F_{0,Arch}$ for all of the automatically segmented ROIs in a 2.3 mm × 2.3 mm FOV. The quantity was used as a measure of shot noise-limited SNR. Selection threshold: 50th percentile for $F_{0,Arch}$; 75th percentile for $\Delta F_{Arch}/\sqrt{F_{0,Arch}}$. **g**, Representative FACS data showing three distinct populations: photoconverted library cells; unselected library cells; spacer cells (green channel: excitation at 488 nm; red channel: excitation at 561 nm). **h**, Three rounds of iterative enrichment shifted the population phenotype. **i**, Manhattan plot showing the mutation frequency at each nucleotide in starting and post-screening libraries. **j**, Logarithmic plot of the starting mutation frequency versus the fold change. In this library there were 970 missense mutations and 405 silent mutations.

and perturbation of membrane potentials, that is, all-optical electrophysiology, or Optopatch[26]. With QuasAr6a-based Optopatch we demonstrated in vivo functional connectivity mapping between optically targeted interneurons in neocortical layer 1. With QuasAr6b-based Optopatch we demonstrated optical detection of electrical synapses between parvalbumin neurons. The QuasAr6 GEVIs have also recently been used to map dendritic voltages in acute brain slices[27]. The Photopick pooled screening platform is a powerful approach for high-dimensional optimization of biosensors, and the improved Arch-derived GEVIs can be broadly useful for all-optical interrogation of neural circuits.

Results

Video-based screening and photoselection in mammalian cells

We developed a video-based pooled screening platform for directed evolution of biosensors in mammalian cells. Figure 1a shows the workflow. A phototaggable (photoconvertible, activatable or switchable) fluorescent protein is co-expressed with the mutant library in the host cells. An ultra-widefield imaging system, modified from the Firefly microscope described in ref. [28], records the dynamic responses of $>10^3$ cells per 2.3 mm × 2.3 mm field of view (FOV) with millisecond time resolution. Cells with the desired phenotype are selectively phototagged through patterned Illumination. We calibrated the

micromirror-based optical targeting system to achieve high fidelity and efficiency at cellular resolution (Fig. 1b–d, Extended Data Fig. 1a,d and Supplementary Methods) and found that mEOS4a (ref. [29]), a green-to-red photoconvertible fluorescent protein, had high photoconversion efficiency (Extended Data Fig. 1b,c). The phototagged cells are then sorted and recovered using FACS. The phototagged population is increased to create a sub-library. The phototagged fluorescent protein degrades during culture expansion while fresh fluorescent protein is synthesized, thus resetting the fluorescent marker to its initial state. The screening, tagging and selection process can be iterated to further enrich for the desired phenotype. The shift of the prevalence of candidate reporter genes is quantified with high-throughput (Illumina) sequencing. Our approach is distinguished from earlier image-based screens[6–11] by the ultra-wide FOV, high-speed imaging, and integration with an engineered electrically excitable cell line.

Directed evolution of Arch-derived GEVIs

High-throughput GEVI screening requires a means to induce spikes in membrane potential (see, for example, refs. [19,30]). We used spiking HEK (human embryonic kidney) cells that co-expressed a voltage-gated sodium channel ($Na_V1.5$) and an inward-rectifier potassium channel ($K_{ir}2.1$). In contrast to previous spiking HEK lines[31,32] the $K_{ir}2.1$ was under the control of a doxycycline-inducible promoter to prevent loss of expression upon multiple passages. We also stably expressed a blue-shifted channelrhodopsin, CheRiff, to optogenetically evoke the spikes. The spiking HEK cells produced collective action potential-like spikes when grown in a confluent monolayer and optically stimulated (Methods). Whole-cell patch clamp (Fig. 2b and Extended Data Fig. 2a) and voltage imaging with a red voltage-sensitive dye, BeRST1 (ref. [33]) (Fig. 2c), validated the all-or-none spikes in response to increasing levels of optogenetic stimulation. Conveniently, endogenous gap junction proteins equalized changes of membrane potential across connected cells[34]. Spikes had a narrow distribution of BeRST1 fluorescence changes ($\Delta F/F_0 = 0.25 \pm 0.02$, mean ± s.d.; Extended Data Fig. 2c). Thus, optogenetically triggered and gap junction-coupled spiking HEK cells provided a substrate with uniform action potentials.

For the starting template we chose the GEVI Archon1[35], which has been well validated in vivo[18,20,21]. To test the baseline variability across cells expressing Archon1, we made a monoclonal Archon1-Citrine spiking HEK cell line. Compared with BeRST1, the GEVI had substantially larger cell-to-cell variability in response to optogenetically induced spikes ($\Delta F/F_0 = 0.23 \pm 0.10$, mean ± s.d., $n = 20{,}900$ cells; Extended Data Fig. 2d), including outliers (the top 1% of cells had $\Delta F/F_0 > 0.54$), which is likely to be due to variations in trafficking. Due to the long positive tail in baseline single-cell sensitivity, we concluded that a pooled screen should select for population-level enrichment in genotype frequency rather than picking individual high-performing cells. Implementation of an enrichment (as opposed to outlier) screen requires many-fold coverage of the genetic diversity of the library, and selection of sufficient cells such that shifts in genotype frequency reflect mean genotype performance.

Given that the voltage-sensing mechanism of rhodopsin-derived GEVIs is not fully understood[36–38], a structure-guided approach might miss functionally important mutations. Beneficial mutations were previously found throughout the scaffold (Supplementary Fig. 1)[26,35]. For these reasons we introduced random mutations throughout the opsin using error-prone polymerase chain reaction (Fig. 2a, Extended Data Fig. 2e and Methods). The library included >10^3 variants (Fig. 2j), although non-uniform mutation rates led to variable mutation frequency.

We developed a bicistronic vector to co-express single copies of GEVI mutants and mEos4a, and introduced these into spiking HEK cells via low-titer lentiviral transduction (multiplicity of infection ~0.01; Fig. 2a, Extended Data Fig. 3e and Methods). Expressing cells were enriched by FACS and mixed with CheRiff-expressing spiking HEK cells lacking a GEVI ('spacer' cells) at a ratio of ~1:10 (Fig. 2d). The spacer cells homogenized the membrane potential via gap junction coupling and created gaps between the library cells to facilitate image segmentation and photoselection.

From each round of selection, 60,000–100,000 cells (30,000–50,000 cells per dish, two dishes per round) were scanned, corresponding to 40–100 copies per variant. For each cell we calculated baseline brightness, F_0, and fluorescence change, ΔF, induced by an optogenetically triggered action potential (Fig. 2e). We used the quantity $\Delta F/F_0$ as a measure of the shot noise-limited SNR. To select mutants that were both sensitive and bright, we set thresholds at ΔF > 50th percentile and $\Delta F/F_0$ > 75th percentile. Approximately 12.5% of cells were selected for photoconversion (Fig. 2f and Extended Data Fig. 2f,g). We avoided over-stringent selection so that the outcome was not dominated by outliers.

The cells were then dissociated and sorted based on their fluorescent markers. Three populations were observed in FACS (Fig. 2g): spacer cells ($green^-$, red^-), unconverted library cells ($green^+$, red^-) and photoconverted library cells ($green^+$, red^+). The photoconverted library cells were recovered and then the population was increased for more screening. After three rounds of enrichment we observed that the population had shifted towards higher F_0 and higher ΔF (Fig. 2h). We sequenced the opsin mutations and analyzed the fractional changes in single nucleotide polymorphism prevalence relative to the starting library (to control for variations in initial mutation frequency; Fig. 2i,j). Although the majority of single nucleotide polymorphisms were either unaffected or depleted, some missense mutations were positively selected above the 2σ threshold determined from a stochastic stimulation (Methods).

Fig. 3 | Characterization of QuasAr6a and QuasAr6b in neurons in culture and slice. a, Homology model of QuasAr6a and QuasAr6b on the archaerhodopsin 3 crystal structure (Protein Data Bank: 6GUY), with the retinal chromophore (pink) and mutated residues for creating QuasAr6a and QuasAr6 from Archon1 highlighted (green, mutations shared by QuasAr6a and 6b; blue, A238S for QuasAr6a; light blue, R237I for QuasAr6b). **b**, Confocal image of Citrine fluorescence (*z*-projection) from QuasAr6a-Citrine (left; $n = 5$ cells) and QuasAr6b-Citrine (right; $n = 5$ cells) expressed in cultured rat hippocampal neurons. Scale bars, 50 µm. **c**, Fluorescence versus voltage curves for QuasAr6a ($n = 3$ cells) and QuasAr6b ($n = 4$ cells) measured under voltage clamp in cultured neurons. Fluorescence is measured relative to F_0 at the holding potential −70 mV. Error bars, s.d. **d**, Example traces from high-throughput Optopatch measurements using QuasAr6a or QuasAr6b combined with CheRiff-CFP in cultured rat hippocampal neurons. In the magnified views below, the circles indicate the automatically detected spike peaks. **e**, Spike raster of the Optopatch measurements for five Arch-derived GEVIs at the highest titers tested. The GEVIs carried either TS-EGFP-ER2 or TS-Citrine-TS × 3-ER2 tags. **f**, Average number of neurons with SNR > 3 per FOV with different GEVIs, as a function of virus titer. **g**, Cumulative probability distribution of SNR for different GEVIs at the highest virus titer. The fraction of cells with borderline SNR (between 3 and 4) was 6% QuasAr6a-Citrine, 3% QuasAr6b-Citrine, 21% Archon1-EGFP and 13% Archon1-Citrine. **h**–**j**, Comparison of optical spike widths (full width measured at 80% below the action potential peak) (**h**), voltage sensitivity (**i**), and per-molecule brightness (**j**) at the highest lentivirus titer ($n = 405, 583, 843, 596$ cells for Archon1-EGFP, Archon1-Citrine, QuasAr6a-Citrine, QuasAr6b-Citrine). Error bars, s.e.m. *$P = 0.01–0.05$; **$P = 0.001–0.01$; ****$P < 0.0001$ (two-sided Student's *t*-test without correction for multiple comparisons). **k**, Concurrent fluorescence (frame rate, 1 kHz) and current clamp recordings (acquisition rate, 100 kHz) in acute brain slice of mouse layer 2/3 cortical neurons expressing somQuasAr6a-EGFP. The spikes were evoked via steady current injection. The 100 kHz electrical trace was downsampled to reveal the low-pass filtering effect of the 1 kHz acquisition rate. **l**, Overlay of spike-triggered average waveform for the optical and electrical traces. **m**, Raw fluorescence versus the subthreshold voltage. **n**–**p**, Similar to **k**–**m**, but for somQuasAr6b-EGFP.

https://doi.org/10.1038/s41592-022-01743-5

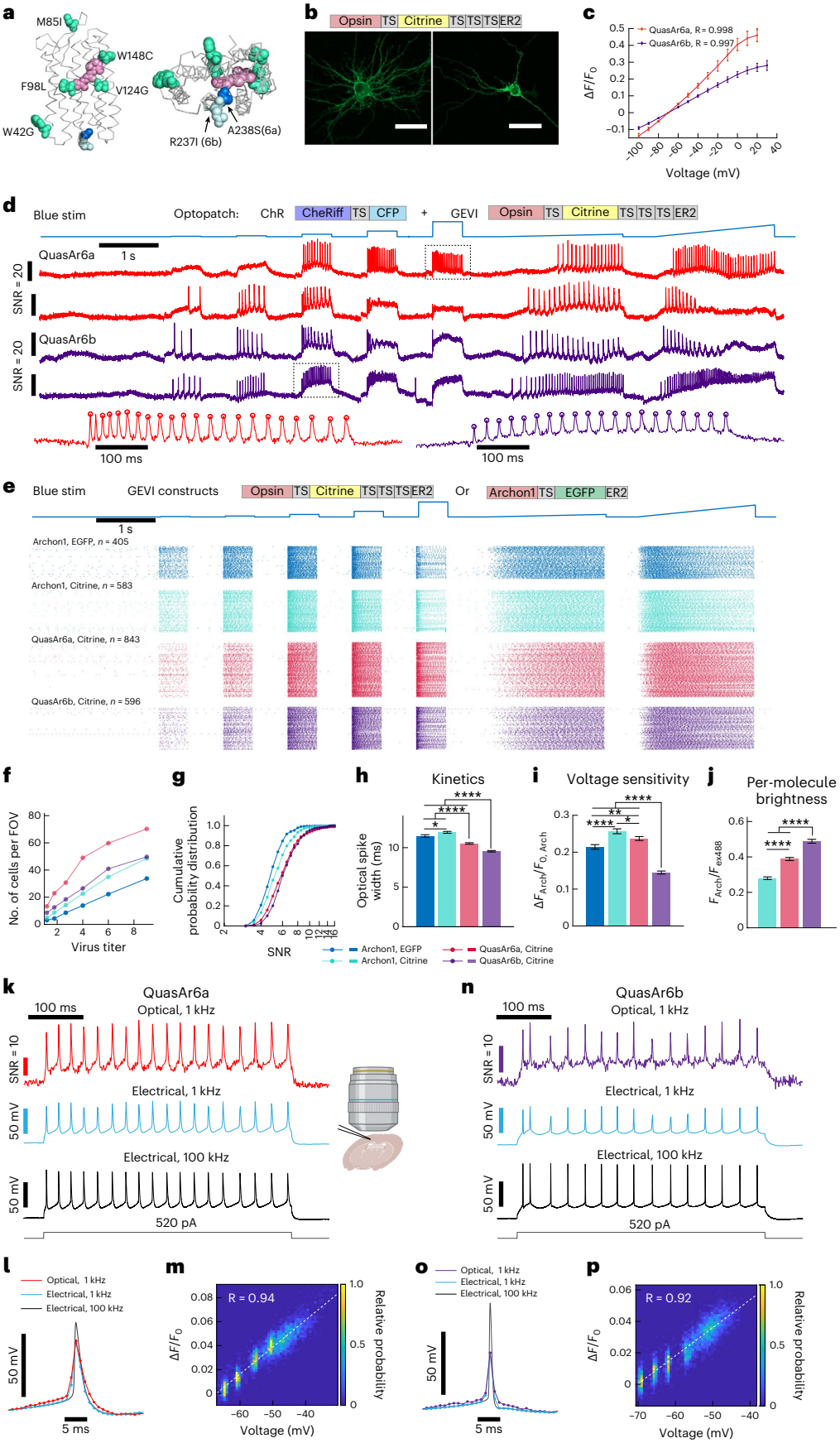

Engineering of QuasAr6a and QuasAr6b

The sequencing results (Fig. 2i,j) provided a short list of candidate mutations. We first created a panel of single missense mutants and screened them in HEK cells for total expression and ratio of brightness of the GEVI to the attached fluorescent protein tag, as a measure of per-molecule GEVI brightness (Extended Data Fig. 4c,d). We prioritized mutations that enhanced per-molecule brightness because we reasoned that this photophysical property is more likely to be conserved between cell types, whereas trafficking or total expression may be more context dependent.

When we sought to combine these mutations, we found that combining two mutations that were close in three-dimensional space often resulted in detrimental effects on trafficking. Therefore, we combined distant mutations based on the archaerhodopsin 3 structure (Protein Data Bank 6GUY) and tested different combinations of mutations that enhanced per-molecule brightness (W42G, V124G, R237I, A238S) and expression level in HEK cells (M85I, F98L, W148C). To our knowledge, most of these sites have not been previously explored in Arch-based GEVIs (Extended Data Fig. 3b). We arrived at two new GEVIs (Fig. 3a and Supplementary Fig. 2): QuasAr6a (Archon1 + W42G/M85I/F98L/V124G/W148C/A238S) and QuasAr6b (Archon1 + W42G/M85I/F98L/V124G/W148C/R237I). These two constructs differed in A238S versus R237I. We found that R237I improved the activation and deactivation kinetics.

The original Archon1 construct consists of the opsin, a trafficking sequence (TS), followed by an enhanced green fluorescent protein (EGFP) tag and an endoplasmic reticulum export signal (ER2) (TS-EGFP-ER2). We previously found that a combination of Citrine and multiple repeats of trafficking sequence (TS-Citrine-TS × 3-ER2) improved the voltage imaging SNRs in cultured neurons[16]. Thus, for subsequent characterization in cultured cells, the QuasAr6a and QuasAr6b opsins carried this optimized Citrine tag.

Characterization of QuasAr6a and QuasAr6b in HEK293T cells

We performed biophysical characterization of QuasAr6a-Citrine and QuasAr6b-Citrine expressed in HEK293T cells (Extended Data Fig. 4). Both showed excellent membrane localization (Extended Data Fig. 4a). Compared with the template Archon1, QuasAr6a had enhanced per-molecule brightness (1.7-fold; Extended Data Fig. 4b), similar voltage sensitivity (73 ± 8% over 100 mV for QuasAr6a, n = 5 cells; 70 ± 13% over 100 mV for Archon1, n = 4 cells; mean ± s.d.; Extended Data Fig. 4c) and similar kinetics at 30 °C (QuasAr6a: $\tau_{(on,\ fast)}$ = 1.8 ± 0.5 ms, $\tau_{(off,\ fast)}$ = 1.3 ± 0.5 ms, n = 7 cells; Archon1: $\tau_{(on,\ fast)}$ = 2.2 ± 0.3 ms, $\tau_{(off,\ fast)}$ = 1.6 ± 0.3 ms, n = 6 cells; Extended Data Fig. 4d,e). QuasAr6b had enhanced per-molecule brightness (2.0-fold) and smaller fractional voltage sensitivity (24 ± 4% over 100 mV, n = 4 cells, mean ± s.d.; Extended Data Fig. 4c), but faster on and off-kinetics at 30 °C ($\tau_{(on,\ fast)}$ = 0.8 ± 0.2 ms, $\tau_{(off,\ fast)}$ = 0.8 ± 0.3 ms, n = 7 cells; Extended Data Fig. 4d,e). Both QuasAr6a and QuasAr6b had a linear fluorescence–voltage relationship from −70 mV to 30 mV (Extended Data Fig. 4c) and excellent photostability (Extended Data Fig. 6f). We also found negligible photocurrent under blue or red illumination for QuasAr6a or QuasAr6b (Extended Data Fig. 4g,h).

Characterization of QuasAr6a and QuasAr6b in neurons

In cultured rat hippocampal neurons, both QuasAr6a and QuasAr6b showed efficient membrane localization (Fig. 3b). QuasAr6a and QuasAr6b had a fractional voltage sensitivity of 43 ± 4% and 27 ± 3% (mean ± s.d.), respectively, from −70 mV to +20 mV (Fig. 3c). To obtain robust statistics on the sensor performance, we used a high-throughput all-optical electrophysiology platform that could perform voltage imaging of >100 cultured neurons in parallel at a 1 kHz frame rate[39]. We compared four Arch-derived GEVIs: Archon1-Citrine, QuasAr6a-Citrine, QuasAr6b-Citrine and Archon1-EGFP that carried a TS-EGFP-ER2 tag as described in the original report[35]. Each of these GEVIs was paired with CheRiff via a bicistronic lentiviral expression vector to enable Optopatch measurement of neuronal excitability (Fig. 3d,e). We tested each construct at six viral titers, four replicate wells for each condition. At the highest titer we measured between 405 and 843 cells for each construct, for a total of 2,427 single-cell voltage imaging recordings.

Neurons were automatically segmented using an activity-based segmentation[40]. Cells were included in the analysis if the single-trial, single-spike SNR (that is, the ratio of spike height to standard deviation of baseline noise) exceeded 3 (Methods). Given that the neurons in all of the wells were plated at the same density, the number of recorded cells per FOV was an indicator of sensor performance (Fig. 3f). Across the titers, QuasAr6a consistently gave 2.1–4-fold more neurons with SNR above threshold per FOV (average of 70 neurons per FOV at highest titer, n = 12 FOVs) compared with Archon1-EGFP (average of 34 neurons per FOV at highest titer), and at least 1.5-fold more above-threshold neurons per FOV compared with Archon1-Citrine (average of 49 neurons per FOV at highest titer). QuasAr6b also outperformed Archon1-EGFP by 1.5–2.2-fold (average of 50 neurons per FOV at highest titer) and yielded comparable numbers of above-threshold neurons per FOV as Archon1-Citrine.

Of the neurons above threshold, QuasAr6a and 6b both produced significantly higher average SNR compared with either Archon1-Citrine or Archon1-EGFP (Fig. 3g and Extended Data Fig. 5a). For Archon1, substituting the TS-EGFP-ER2 tag with the TS-Citrine-TS × 3-ER2 tag improved voltage sensitivity by ~20% across the titers and hence gave higher SNR (Fig. 3g and Extended Data Fig. 5c), which is likely to be due to improved trafficking (see ref. [16], Extended Data Fig. 1). For each GEVI type, expression level did not affect measured spike width (Extended Data Fig. 5g–j), suggesting that GEVI expression did not affect the basic biophysical properties of the cells. The optical spike widths (full width at 80% below the action potential peak) reported for both QuasAr6a (10.4 ± 0.1 ms; mean ± s.e.m., n = 843 neurons) and QuasAr6b (9.5 ± 0.1 ms, n = 596 neurons) were smaller than the spike widths for Archon1-Citrine (11.9 ± 0.1 ms, n = 583 neurons) and Archon1-EGFP (11.4 ± 0.1 ms, n = 583 neurons; Fig. 3h and Extended Data Fig. 5b). We attribute the spike broadening relative to typical

Fig. 4 | Characterization of somQuasAr6a- and somQuasAr6b-based Optopatch in vivo. Recordings were performed with a ×25 objective (NA = 1.05). **a**,**b**, Simultaneous optogenetic stimulation and voltage imaging (996 Hz) in layer 1 NDNF cells (visual cortex) expressing somQuasAr6a- or somQuasAr6b-based Optopatch in anesthetized mice. A magnified view of the boxed regions is shown on the right. **c**, Comparison of in vivo SNR of somQuasAr6a (n = 32 cells, two animals), somQuasAr6b (n = 29 cells, two animals) and somArchon1 (n = 23 cells, two animals) in NDNF cells. NS, not significant, two-sided Wilcoxon rank-sum test. **d**, Comparison of optical spike FWHM of optogenetically triggered spikes in NDNF cells, imaged with somQuasAr6a (n = 32 cells, two animals), somQuasAr6b (n = 29 cells, two animals) and somArchon1 (n = 23 cells, two animals) at a 1 kHz frame rate. NS, not significant, two-sided Wilcoxon rank-sum test. **e**, Spike-triggered average fluorescence waveforms of the optogenetically triggered spikes in NDNF cells measured with somQuasAr6a, somQuasAr6b and somArchon1. **f**, Double-ramp Optopatch measurements in hippocampal parvalbumin cells (voltage imaging at 1,973 Hz) in anesthetized mice. A magnified view of the boxed regions is shown on the right. **g**, Comparison of the in vivo SNR of QuasAr6b (n = 24 cells, three animals) and Archon1 in parvalbumin cells (n = 25 cells, two animals), two-sided Wilcoxon rank-sum test. **h**, Comparison of optical spike FWHM of optogenetically triggered spikes in parvalbumin cells, imaged with somQuasAr6b and somArchon1 at a 2 kHz frame rate, two-sided Wilcoxon rank-sum test. **i**, Spike-triggered average fluorescence waveforms of the optogenetically triggered spikes in parvalbumin cells measured with somQuasAr6b and somArchon1. In the box plots the central mark indicates the median, the bottom edge indicates the 25th percentile, the top edge indicates the 75th percentile and the whiskers indicate the most extreme data points excluding outliers. +, outliers.

https://doi.org/10.1038/s41592-022-01743-5

in vivo measurements to the fact that the cultured neuron data were acquired at room temperature.

Despite having slightly lower sensitivity at the highest titer tested, at most titers the voltage sensitivity of QuasAr6a-Citrine was comparable to that of Archon1-Citrine and outperformed Archon1-EGFP (Fig. 3i and Extended Data Fig. 5c). The voltage sensitivity of QuasAr6b was lower than that of Archon1-Citrine or QuasAr6a-Citrine by 40–45% (Fig. 3i and Extended Data Fig. 5c). Nonetheless, the superior brightness and 1.5-fold greater expression of QuasAr6b compensated for its lower voltage sensitivity, to give a higher SNR. QuasAr6a and QuasAr6b had enhanced per-molecule brightness ($F_{Arch}/F_{excitation\ at\ 488}$, that is, the ratio of baseline fluorescence in the Arch channel to the baseline fluorescence

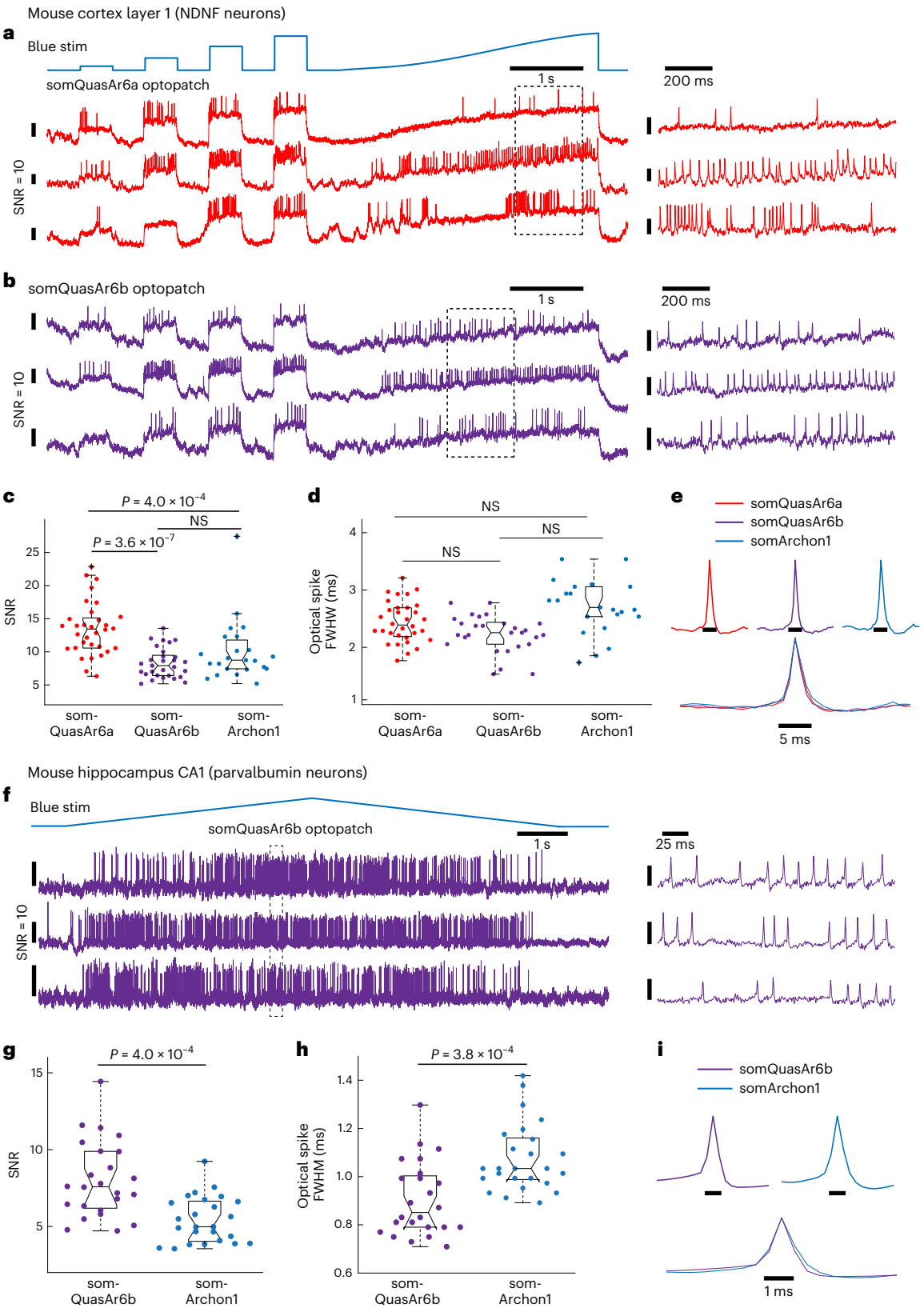

in the Citrine channel) compared with Archon1 (1.4-fold and 1.7-fold, respectively; Fig. 3j and Extended Data Fig. 5d).

We then tested QuasAr6a and QuasAr6b in acute mouse brain slices. To resolve individual neurons, we designed soma-targeted versions of QuasAr6a and QuasAr6b by appending a $K_V2.1$ trafficking motif to the carboxy terminus[16,18,41,42]. For the soma-targeted Arch-derived GEVIs, we have not systematically evaluated whether the choice of fluorescent protein tag makes a difference for their in vivo performance. To stay consistent with the recent reports[18,20], the somQuasAr6a and somQuasAr6b constructs carried an EGFP tag as an expression marker. For optogenetic activation in tissue, we used a soma-localized version of CheRiff, somCheRiff[16]. We made a Cre-dependent adeno-associated virus vector, AAV2/9, for somQuasAr6a and somQuasAr6b and the corresponding bicistronic Optopatch constructs. We sparsely expressed the Optopatch constructs in mouse cortex and hippocampus. Confocal imaging confirmed that somQuasAr6a/b and somCheRiff trafficked well in vivo and were largely restricted to soma and proximal dendrites (Extended Data Fig. 6).

Patch clamp recordings of somQuasAr6a- or somQuasAr6b-expressing cortical neurons in brain slices showed that these GEVIs did not detectably affect membrane electrical properties or excitability (Extended Data Fig. 7). Concurrent fluorescence imaging and current clamp recordings showed that somQuasAr6a and someQuasAr6b reported the membrane potential with high fidelity (Fig. 3k–p). The spike-triggered average optical and electrical spike waveforms had high correlation when both were sampled at 1 kHz (QuasAr6a, R = 0.97 ± 0.02, n = 6 cells; QuasAr6b, R = 0.984 ± 0.004, n = 7 cells; Fig. 3i,o). The fluorescence correlated linearly with the subthreshold membrane potentials (QuasAr6a, R = 0.94; QuasAr6b, R = 0.92; Fig. 3m,p).

The fluorescence of several Arch-based GEVIs is modulated by blue light[8,16]; therefore, we assessed this effect in QuasAr6a and QuasAr6b (Extended Data Fig. 10). Under blue light intensity used for optogenetic stimulation (488 nm, 60 mW cm^{-2}), blue light modulation of the fluorescence was <3% (Extended Data Fig. 10a–f). Illumination with sixfold stronger blue light (370 mW cm^{-2}) led to small fluorescence enhancement of QuasAr6a and QuasAr6b (QuasAr6a, 7 ± 2%; QuasAr6b, 12 ± 2%; Extended Data Fig. 10g). Overall, QuasAr6a and QuasAr6b can be combined with optogenetic stimulation with negligible crosstalk under most circumstances. For strong stimuli time-locked to a subthreshold voltage response, corrections for crosstalk may be necessary.

Validation of QuasAr6a and QuasAr6b in vivo

Next, we compared the in vivo performance of the QuasAr6 GEVIs. For one-photon voltage imaging in tissue, structured illumination partially overcomes the effects of background autofluorescence and light scattering. We previously characterized different structured illumination schemes in detail (see Fig. 5 of ref. [8]). To achieve the highest SNR, we used a holographic structured illumination microscope that patterned the 635 nm light for voltage imaging (Extended Data Fig. 8a,b) and the 488 nm light for targeted optogenetic stimulation (see Fig. 1 and Supplementary Figs. 1 and 2 of ref. [20]). Cells were recorded one at a time in head-fixed, anesthetized mice (Fig. 4 and Extended Data Fig. 8).

We first compared somQuasAr6a, somQuasAr6b and somArchon1 in cortical neuron-derived neurotrophic factor (NDNF) cells. In the cortex, NDNF marks GABAergic neurogliaform cells that are mostly restricted to the topmost 100 µm of layer 1 (refs. [43–45]). We expressed Optopatch constructs based on somQuasAr6a, somQuasAr6b or somArchon1 in the visual cortex of NDNF-Cre$^{+/-}$ mice (Fig. 4a–e). Optopatch constructs gave single-spike SNRs of 13.5 ± 4.0 for somQuasAr6a (mean ± s.d., n = 32 cells, two animals), 8.3 ± 2.3 for somQuasAr6b (mean ± s.d., n = 29 cells, two animals) and 9.3 ± 2.8 for somArchon1 (mean ± s.d., n = 22 cells, two animals; Fig. 4c). In the samples expressing somQuasAr6b and somArchon1, many cells were near the analysis cut-off of SNR = 4, suggesting that the underlying distributions of SNR may have had a lower mean than reported above. All three GEVIs reported spike waveforms with similar optical spike widths (Fig. 4d,e; somQuasAr6a, 2.4 ± 0.4 ms; somQuasAr6b, 2.3 ± 0.3 ms; somArchon1, 2.7 ± 0.5 ms; mean ± s.d.). SomQuasAr6a reliably detected spikes in NDNF cells after 200 seconds of continuous illumination (Extended Data Fig. 9a).

We next compared somQuasAr6b and somArchon1 in fast-spiking hippocampal parvalbumin neurons. These interneurons provide strong perisomatic inhibition of nearby pyramidal cells[46] but have been difficult to target via patch clamp in the live mouse hippocampus[47]. The narrow spikes of parvalbumin neurons (full width at half-maximum (FWHM) < 0.5 ms)[48] impose an additional challenge for optical detection. We explored whether the fast variant QuasAr6b could enable accurate detection of these spikes. We injected AAV2/9 for Cre-dependent somQuasAr6b-Optopatch and somArchon1-Optopatch into the hippocampal CA1 region of parvalbumin-Cre$^{+/-}$ transgenic mice (Extended Data Fig. 6c). The overlying cortical tissue was removed and replaced with a cannula window[16,49].

We performed voltage imaging at a 2 kHz frame rate for positive parvalbumin neurons expressing the Optopatch constructs in the stratum oriens (Fig. 4f–l and Extended Data Fig. 8c). somQuasAr6b had a higher SNR (×25 objective: 8.0 ± 2.5, n = 24 cells, three animals; ×10 objective: 7.9 ± 2.2, n = 20 cells, three animals; mean ± s.d.) and narrower optical FWHM (0.87 ± 0.11 ms, mean ± s.d.) than Archon1 (×25: SNR, 5.4 ± 1.5, n = 23 cells, two animals; ×10: SNR, 5.5 ± 1.0; optical FWHM, 1.1 ± 0.15 ms, n = 24 cells, two animals).

We also imaged the optogenetically triggered spikes with somQuasAr6b at a frame rate of 4 kHz (n = 13 cells, two animals, Extended Data Fig. 8d). The mean spike half-width reduced from 0.91 ms at 2 kHz to 0.71 ms at 4 kHz (Extended Data Fig. 8e,f), approaching the spike width measured by patch clamp (0.49 ± 0.04 ms)[48]. QuasAr6b reported the parvalbumin spikes for up to 200 seconds of imaging (Extended Data Fig. 9b). Thus, somQuasAr6b is a fast and high-SNR sensor suited for reporting sub-millisecond voltage dynamics.

Fig. 5 | Optical dissection of inhibitory connections between NDNF interneurons in visual cortex. a, Schematic diagram of two-cell Optopatch in NDNF interneurons. Small open circles indicate inhibitory synapses. **b**, Optogenetic stimulation waveform for probing inhibitory connections in a pair of optically targeted NDNF cells. Scale bar, 10 µm. A cell designated as presynaptic was activated by ramp stimulation. The postsynaptic cell was depolarized with a constant step stimulation to increase the driving force for inhibitory currents. Then the roles of presynaptic and postsynaptic were reversed. **c**, Optopatch revealed strong mutual inhibition between a pair of NDNF neurons (inter-soma distance r = 69 µm). Top to bottom: representative traces, raster plots for five consecutive trials; spike rate estimated using the BAKS. **d**, For the cell pair in **c**, change of spike rate after the onset of the first presynaptic spike (dashed line) or at the corresponding time in the control epoch. **e**,**f**, Similar to **c**,**d**, for a pair of NDNF cells with weaker inhibitory connections (inter-soma distance r = 111 µm). **g**, Average of all of the postsynaptic cells (n = 51 cells). Shading in **c**–**g**, s.e.m. **h**, The strong inhibitory connections and the weak inhibitory connections had similar presynaptic spike rates. The postsynaptic inhibition strength was quantified by the relative post-stimulation rate in the postsynaptic cell, defined as the ratio of the minimum spike rate in the postsynaptic cell in the window 0–100 ms after the first presynaptic spike, to the average spike rate during the window −100 ms to −10 ms before the first presynaptic spike. A cut-off of 0.6 was chosen to separate strong (n = 32) and weak (n = 19) inhibitory connections. The presynaptic spike rate was defined as the average spike rate in the 0–100 ms window after the first presynaptic spike. In the box plots the central mark indicates the median, the bottom edge indicates the 25th percentile, the top edge indicates the 75th percentile and the whiskers indicate the most extreme data points excluding outliers. NS, not significant, two-sided Wilcoxon rank-sum test. **i**, Two-way inhibition strength for 22 pairs of cells. The inhibition strength was quantified by the relative post-stimulation rate.

https://doi.org/10.1038/s41592-022-01743-5

Mapping functional connections between NDNF cells

An optical method that probes cell-to-cell functional connectivity in vivo would be a powerful tool for systems neuroscience. The laterally projecting axon arbors of NDNF cells form a short-range, mutually inhibitory network[20,43,45]. The role of this lateral inhibition is not well understood. We previously showed that transient optogenetic activation of a population of layer 1 interneurons suppressed the spiking of a nearby cell[20]. However, it was unclear how much of an effect that activation of a single layer 1 interneuron would have on its neighbors, or how cell-to-cell connection strengths were distributed.

The improved SNR of somQuasAr6a cells permitted us to record from multiple layer 1 NDNF cells simultaneously, and thereby to correlate activity of putative pre- and post-synaptic cells. In pairs of layer 1 NDNF cells, we arbitrarily designated one as 'presynaptic' and one as 'postsynaptic' (Fig. 5a,b). The postsynaptic cell was optogenetically stimulated with a 1 second step of blue light to depolarize the cell and

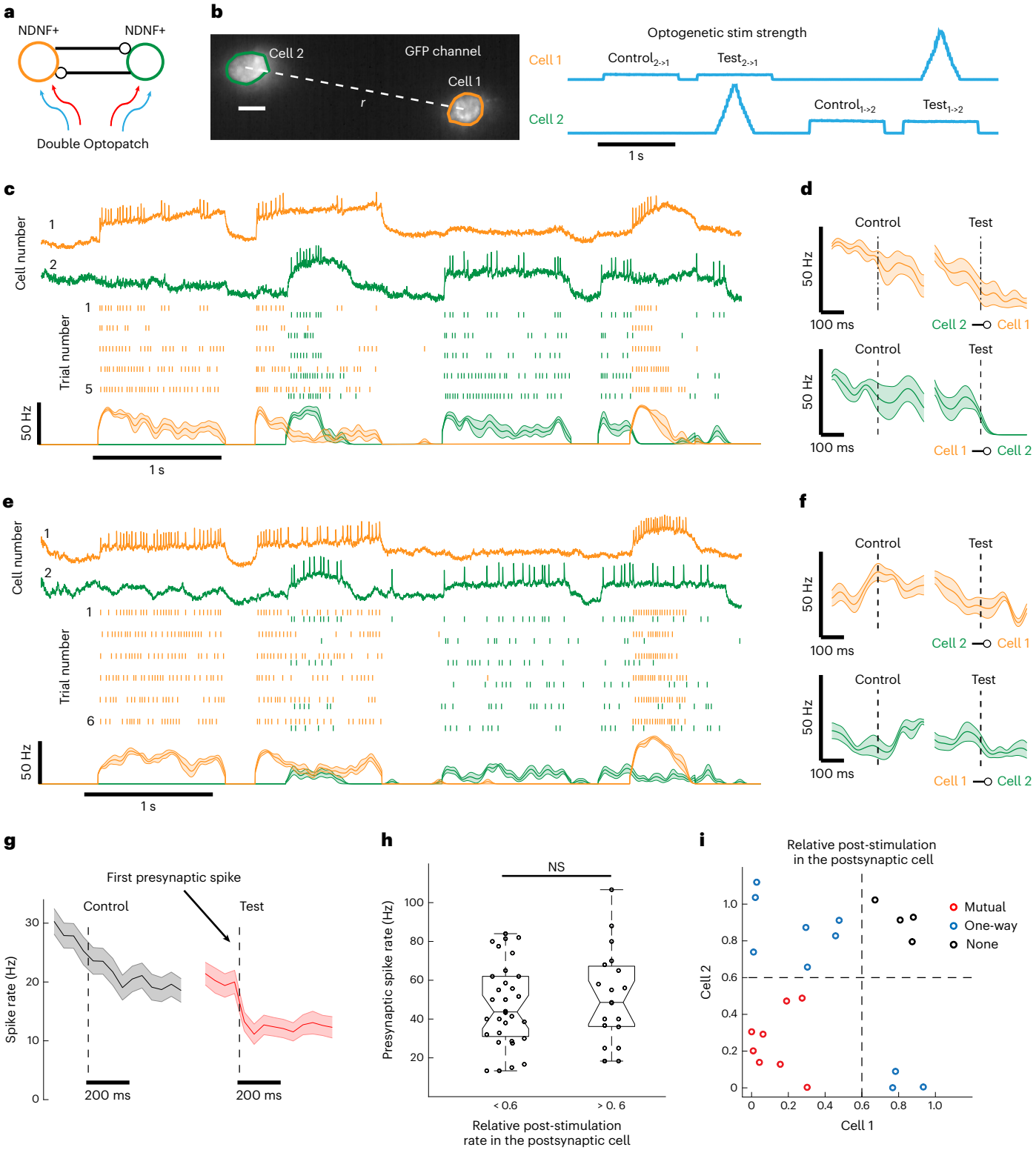

https://doi.org/10.1038/s41592-022-01743-5

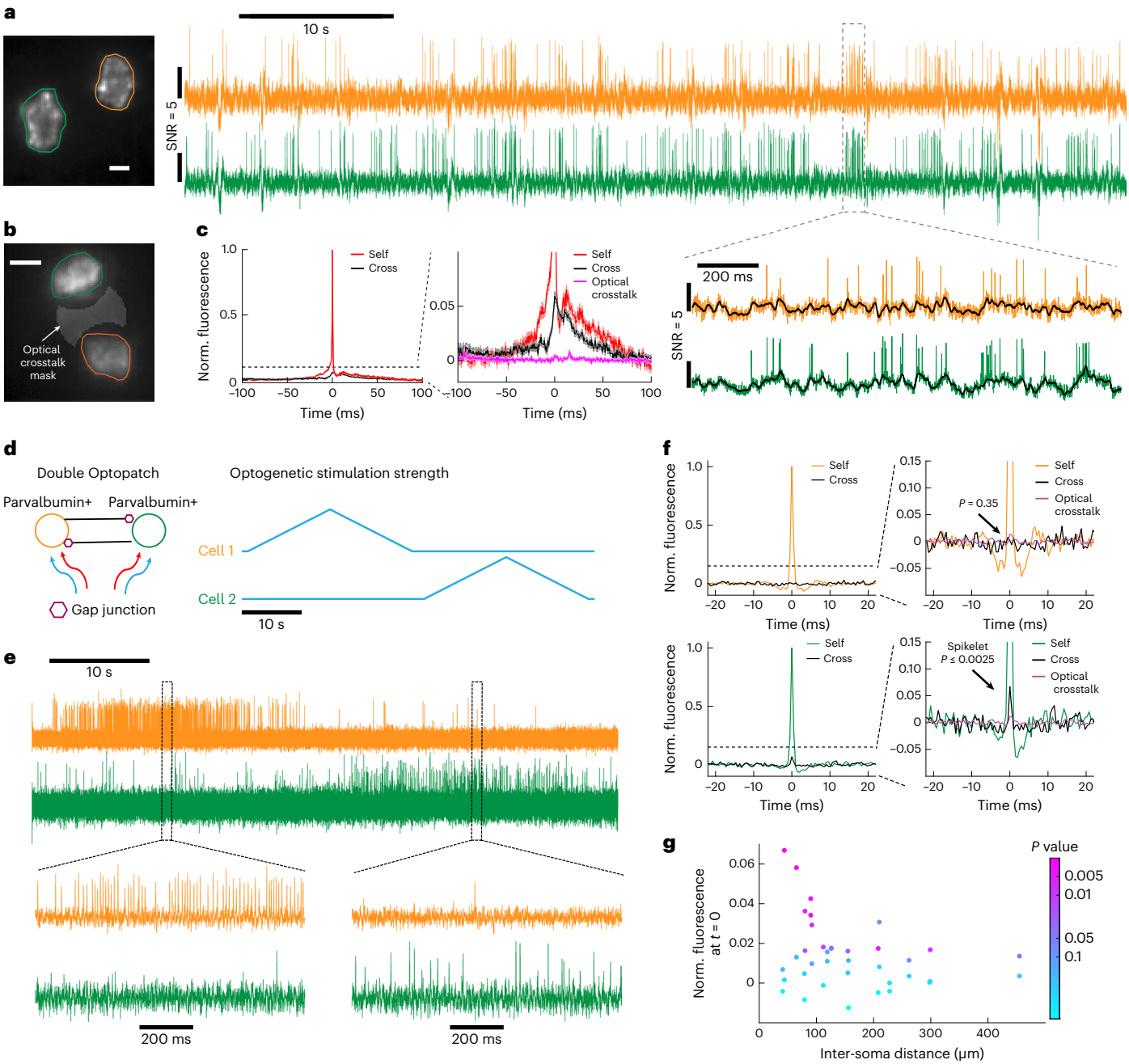

Fig. 6 | Detection of electric coupling between hippocampal parvalbumin cells. a, Simultaneous recording of spontaneous dynamics in two parvalbumin neurons in a lightly anesthetized mouse. To accommodate two parvalbumin neurons in the 2 kHz recording zone of the sCMOS camera, the recording was performed with a ×10 objective (NA = 0.6; $n = 31$ pairs from two animals). Scale bar, 10 μm. **b**, Fluorescence traces were extracted from cell masks and from an intervening mask to characterize optical crosstalk. Scale bar, 20 μm. **c**, Self- and cross-STVW for events in which the spike maxima in each cell were separated by >10 ms ($n = 31$ pairs from two animals). **d**, Double Optopatch experiment to probe the gap junction connections between parvalbumin cells. **e**, Example fluorescence traces of the double Optopatch experiment. **f**, In a pair of parvalbumin cells 44 μm apart, a gap junction-mediated spikelet was observed in the cross-STVW in one cell but not in the other. See Supplementary Methods for the definition of *P* value. **g**, Cross-STVW fluorescence at $t = 0$ (normalized (norm.) to the postsynaptic spike height) versus inter-soma distance ($n = 19$ pairs from five animals).

thereby increase the driving force for inhibitory currents. The presynaptic cell was simultaneously stimulated with a blue light ramp to evoke spiking when the stimulus crossed an optical rheobase threshold. This protocol enabled us to distinguish the effects of presynaptic spiking from blue light crosstalk.

We optically monitored the voltage in both cells to observe whether there was a change in the spike rate of the postsynaptic cell following the first spike in the presynaptic cell. As control measurements, we included epochs without presynaptic stimulation. We then swapped the blue light waveforms between the pair to test the connectivity in the other direction (Fig. 5b). For each pair of cells we performed 2–7 trials. We used a Bayesian adaptive kernel smoother (BAKS)[50] to estimate the instantaneous spike rate. We performed these measurements in anesthetized mice to minimize background voltage fluctuations.

We performed double Optopatch experiments on 30 pairs of cells from four animals, in which the inter-soma distance ranged from 46 μm to 216 μm. Figure 5c,d shows a pair with strong reciprocal inhibition, while Fig. 5e,f shows a pair exhibiting weaker, one-way inhibition.

To accurately test for a synaptically driven decrease in spike rate, we restricted analysis to postsynaptic cells in which direct optogenetic stimulation evoked a spike rate above 5 Hz (n = 51 cells, 22 pairs in which both cells spiked above 5 Hz). Activation of a putative presynaptic cell reduced the mean spike rate of its neighbor from 20 ± 2 Hz to 11 ± 1.7 Hz (mean ± s.e.m., Fig. 5g). The connections that showed strong inhibition had a comparable presynaptic spike rate (n = 32 connections, 47 ± 21 Hz, mean ± s.d.) to the connections that showed weak inhibition (n = 19 connections, 52 ± 24 Hz, mean ± s.d.; Fig. 5h). There was no correlation between presynaptic spike rate and strength of postsynaptic inhibition (R = 0.07), confirming that absence of inhibition was not due to absence of presynaptic activity.

We found that 36% of the pairs (8 of 22) showed reciprocal mutual inhibition, 45% (10 of 22) showed one-way inhibition, and the rest showed no inhibition (4 of 22; Fig. 5i). A combinatorial calculation (Methods) indicated that existence of a connection from cell A to B did not affect the probability of connection from B to A. Thus, although the inhibitory connections between NDNF cells were strong (~45% spike rate suppression), consistent with the results in acute slice[44], this inhibitory effect was not always reciprocal. A key next step will be to relate the functional connectivity maps to the responses of the network to naturalistic sensory and modulatory inputs.

Mapping gap junction-mediated spikelets in parvalbumin cells

Voltage imaging provided a unique opportunity to analyze the correlated voltage dynamics between parvalbumin cells. We recorded pairs of hippocampal parvalbumin neurons (Fig. 6a) and calculated the mean self- and cross-spike-triggered voltage waveform (STVW). For the cross-STVW we restricted analysis to events in which only one cell spiked (spike peaks in the two cells separated by >10 ms), to avoid spurious contributions from near-coincident spikes. For cell 1 → 2 cross-STVW the cell 2 voltage showed little depolarization for $\tau < 0$, had a sharp jump near $\tau = 0$, and then relaxed closely following the waveform of cell 1 for $\tau > 0$ (Fig. 6c). Control experiments using a non-cell region 2 confirmed that the signals were not due to scattered fluorescence from cell 1 (Fig. 6b,c).

The appearance of a low-pass-filtered copy of the cell 1 waveform in cell 2, even when cell 2 did not spike, suggested gap junction-mediated coupling. However, there remained a possibility that the cross-STVW waveform had a contribution from shared synaptic inputs. We therefore used optogenetic stimulation to trigger spikes alternately in each cell and recorded the spiking and subthreshold dynamics in both (Fig. 6d–g and Extended Data Fig. 10). Given that the presynaptic spike times were independent of subthreshold dynamics, this approach eliminated any possible contribution of shared synaptic inputs to the cross-STVWs.

We calculated the self- and cross-STVWs in both directions for 19 parvalbumin pairs with inter-soma distances from 41 to 455 µm (164 ± 108 µm, mean ± s.d.; Fig. 6g). With regard to the pairs separated by <100 µm we observed a subset (5 of 7 pairs) with statistically significant spikelets ($P < 0.05$; amplitudes greater than 2% of the action potential amplitude), with an average amplitude of 4.0 ± 1.7% (mean ± s.d.; Methods). Of these five pairs, two pairs had reciprocal connections and three pairs were unidirectional. We did not observe any such spikelets for pairs separated by >100 µm. These results are consistent with in vivo dual patch clamp recordings of gap junction-coupled cerebellar Golgi cells[51] and support the interpretation that short-range gap junctional coupling was present in a subset of the hippocampal parvalbumin cells.

Discussion

Pooled screens offer the practical advantages of lower cost and higher throughput compared with arrayed screens[6–11,35,52], and are robust to artifacts from well-to-well variability[53]. However, pooled screens can be sensitive to spurious outliers if only a small number of cells are selected. We previously developed a phototagging technique (Photostick)[54], in which a small number of cells in the pooled library were photocrosslinked to the dish and later retrieved with pipette aspiration. This approach was suitable for screening for qualitatively distinct phenotypes such as non-linear photoactivation[8]. In contrast, to screen for quantitative improvements in a continuously variable phenotype, much larger-scale selections were needed. Several photoselection-based pooled screening strategies have been demonstrated[6,7,9,10]. Our work demonstrated the feasibility of pooled screening in directed evolution of biosensors along multiple dimensions. Here, the wide-field optics of the Photopick system enabled multifold coverage of the mutant library while targeted photoconversion achieved a high photoselection efficiency and fidelity. High-throughput sequencing was a key tool for genotype enrichment analysis. In this application, a practical challenge was that the screened cells needed to be embedded in a confluent monolayer to support collective action potentials, which precluded aspiration-based mechanical separation[8,35,55].

Similar photoselection methodology could be used to optimize fluorescent sensors of other modalities or enable cell tagging in vivo[56]. To achieve spectral compatibility with blue or green reporters, one could mark target cells with a dark-to-green (for example, PA-GFP) or dark-to-red (for example, PA-mCherry) fluorescent protein instead of the green-to-red mEos4a fluorescent protein we used here. The Photopick platform is in principle compatible with any imaging-based assay of cellular structure or dynamics. Potential applications include forward genetic screens, for example, for genes that affect cell migration, chemotaxis or responses to mechanical or metabolic perturbations.

In prior GEVI engineering efforts, mutations were introduced randomly into the scaffold[26,35] or targeted to specific regions[5,19,22,30] or 'hotspots'[24]. To our surprise, most of the newly identified mutations in QuasAr6 were located on the protein surface, which is likely to be indicative of the critical importance of membrane trafficking. This observation may be relevant to the engineering of other sensors based on transmembrane scaffolds. An internal mutation arose at R237, which is homologous to bacteriorhodopsin R227. Bacteriorhodopsin R227 is a key component of the intramolecular proton uptake pathway[57,58]. This role in connecting the titratable Schiff base to the cytoplasm could potentially explain why mutation of this residue to neutral isoleucine accelerated voltage-sensing kinetics in QuasAr6b.

Our data highlight the interdependence of SNR and sensor kinetics as well as the importance of cell type- and system-specific characterization. In the fast-spiking parvalbumin neurons, the faster sensor QuasAr6b exhibited better SNR despite its lower steady-state voltage sensitivity, compared with Archon1. In NDNF cells and cultured neurons, QuasAr6a with its larger voltage sensitivity and slower kinetics outperformed QuasAr6b. Both GEVIs remain substantially dimmer than other far-red fluorescent indicators, limiting the total number of neurons that can be recorded simultaneously in vivo. Development of brighter far-red GEVIs, based either on archaerhodopsin 3 or on other mechanisms, remains an important goal.

For functional connectivity mapping in the mammalian brain, targeted perturbations can distinguish genuine connections from the effects of shared inputs. Multi-cell patch clamp measurements in vivo are technically demanding[47,51,59,60]. All-optical electrophysiology provides an alternate approach but requires voltage imaging and optogenetic manipulation to be crosstalk free. Given that all known channelrhodopsins have substantial photocurrents in the blue part of the spectrum, crosstalk is minimized by combining a blue-shifted channelrhodopsin with a voltage indicator excited at 590 nm or longer. Thus far, only the combination of far-red Arch-derived GEVIs with blue-shifted channelrhodopsins has demonstrated sufficient spectral orthogonality to meet this standard. In our proof-of-concept all-optical connectivity mapping experiments, both voltage imaging and optogenetic stimulation were integral for probing chemical and electric synapses. For studies of spontaneous network dynamics it will be important to extend the measurements to awake animals. Together, QuasAr6a and QuasAr6b, with their improved in vivo performance and

spectral compatibility with blue-shifted channelrhodopsins, open many possibilities for understanding the relation between neural circuitry and network dynamics.

Online content

Any methods, additional references, Nature Portfolio reporting summaries, source data, extended data, supplementary information, acknowledgements, peer review information; details of author contributions and competing interests; and statements of data and code availability are available at https://doi.org/10.1038/s41592-022-01743-5.

References

1. Lin, M. Z. & Schnitzer, M. J. Genetically encoded indicators of neuronal activity. *Nat. Neurosci.* **19**, 1142–1153 (2016).
2. Yang, W. & Yuste, R. In vivo imaging of neural activity. *Nat. Methods* **14**, 349–359 (2017).
3. Kim, T. H. & Schnitzer, M. J. Fluorescence imaging of large-scale neural ensemble dynamics. *Cell* **185**, 9–41 (2022).
4. Tian, L. et al. Imaging neural activity in worms, flies and mice with improved GCaMP calcium indicators. *Nat. Methods* **6**, 875–881 (2009).
5. Chen, T. W. et al. Ultrasensitive fluorescent proteins for imaging neuronal activity. *Nature* **499**, 295–300 (2013).
6. Hasle, N. et al. High-throughput, microscope-based sorting to dissect cellular heterogeneity. *Mol. Syst. Biol.* **16**, e9442 (2020).
7. Lee, J. et al. Versatile phenotype-activated cell sorting. *Sci. Adv.* **6**, eabb7438 (2020).
8. Chien, M. P. et al. Photoactivated voltage imaging in tissue with an archaerhodopsin-derived reporter. *Sci. Adv.* **7**, eabe3216 (2021).
9. Kanfer, G. et al. Image-based pooled whole-genome CRISPRi screening for subcellular phenotypes. *J. Cell Biol.* **220**, e202006180 (2021).
10. Yan, X. et al. High-content imaging-based pooled CRISPR screens in mammalian cells. *J. Cell Biol.* **220**, e202008158 (2021).
11. Lawson, M. & Elf, J. Imaging-based screens of pool-synthesized cell libraries. *Nat. Methods* **18**, 358–365 (2021).
12. Akemann, W., Mutoh, H., Perron, A., Rossier, J. & Knopfel, T. Imaging brain electric signals with genetically targeted voltage-sensitive fluorescent proteins. *Nat. Methods* **7**, 643–649 (2010).
13. Knopfel, T. Genetically encoded optical indicators for the analysis of neuronal circuits. *Nat. Rev. Neurosci.* **13**, 687–700 (2012).
14. Gong, Y. et al. High-speed recording of neural spikes in awake mice and flies with a fluorescent voltage sensor. *Science* **350**, 1361–1366 (2015).
15. Marshall, J. D. et al. Cell-type-specific optical recording of membrane voltage dynamics in freely moving mice. *Cell* **167**, 1650–1662 (2016).
16. Adam, Y. et al. Voltage imaging and optogenetics reveal behaviour-dependent changes in hippocampal dynamics. *Nature* **569**, 413–417 (2019).
17. Abdelfattah, A. S. et al. Bright and photostable chemigenetic indicators for extended in vivo voltage imaging. *Science* **365**, 699–704 (2019).
18. Piatkevich, K. D. et al. Population imaging of neural activity in awake behaving mice. *Nature* **574**, 413–417 (2019).
19. Villette, V. et al. Ultrafast two-photon imaging of a high-gain voltage indicator in awake behaving mice. *Cell* **179**, 1590–1608 (2019).
20. Fan, L. Z. et al. All-optical electrophysiology reveals the role of lateral inhibition in sensory processing in cortical layer 1. *Cell* **180**, 521–535 (2020).
21. Böhm, U. L. et al. Voltage imaging identifies spinal circuits that modulate locomotor adaptation in zebrafish. *Neuron* **110**, 1211–1222 (2022).
22. Kannan, M. et al. Dual-polarity voltage imaging of the concurrent dynamics of multiple neuron types. *Science* **378**, eabm8797 (2022).
23. Evans, S. W. et al. A positively tuned voltage indicator reveals electrical correlates of calcium activity in the brain. Preprint at *bioRxiv* https://doi.org/10.1101/2021.10.21.465345 (2021).
24. Abdelfattah, A. S. et al. Sensitivity optimization of a rhodopsin-based fluorescent voltage indicator. Preprint at *bioRxiv* https://doi.org/10.1101/2021.11.09.467909 (2021).
25. Herwig, L. et al. Directed evolution of a bright near-infrared fluorescent rhodopsin using a synthetic chromophore. *Cell Chem. Biol.* **24**, 415–425 (2017).
26. Hochbaum, D. R. et al. All-optical electrophysiology in mammalian neurons using engineered microbial rhodopsins. *Nat. Methods* **11**, 825–833 (2014).
27. Landau, A. T. et al. Dendritic branch structure compartmentalizes voltage-dependent calcium influx in cortical layer 2/3 pyramidal cells. *eLife* **11**, e76993 (2022).
28. Werley, C. A., Chien, M. P. & Cohen, A. E. Ultrawidefield microscope for high-speed fluorescence imaging and targeted optogenetic stimulation. *Biomed. Opt. Express* **8**, 5794–5813 (2017).
29. Paez-Segala, M. G. et al. Fixation-resistant photoactivatable fluorescent proteins for CLEM. *Nat. Methods* **12**, 215–218 (2015).
30. Kannan, M. et al. Fast, in vivo voltage imaging using a red fluorescent indicator. *Nat. Methods* **15**, 1108–1116 (2018).
31. Park, J. et al. Screening fluorescent voltage indicators with spontaneously spiking HEK cells. *PLoS ONE* **8**, e85221 (2013).
32. Zhang, H., Reichert, E. & Cohen, A. E. Optical electrophysiology for probing function and pharmacology of voltage-gated ion channels. *eLife* **5**, e15202 (2016).
33. Huang, Y. L., Walker, A. S. & Miller, E. W. A photostable silicon rhodamine platform for optical voltage sensing. *J. Am. Chem. Soc.* **137**, 10767–10776 (2015).
34. McNamara, H. M. et al. Geometry-dependent arrhythmias in electrically excitable tissues. *Cell Syst.* **7**, 359–370 (2018).
35. Piatkevich, K. D. et al. A robotic multidimensional directed evolution approach applied to fluorescent voltage reporters. *Nat. Chem. Biol.* **14**, 352–360 (2018).
36. Maclaurin, D., Venkatachalam, V., Lee, H. & Cohen, A. E. Mechanism of voltage-sensitive fluorescence in a microbial rhodopsin. *Proc. Natl Acad. Sci. USA* **110**, 5939–5944 (2013).
37. Penzkofer, A., Silapetere, A. & Hegemann, P. Photocycle dynamics of the archaerhodopsin 3 based fluorescent voltage sensor QuasAr1. *Int. J. Mol. Sci.* **21**, 160 (2019).
38. Penzkofer, A., Silapetere, A. & Hegemann, P. Photocycle dynamics of the Archaerhodopsin 3 based fluorescent voltage sensor Archon2. *J. Photochem. Photobiol. B* **225**, 112331 (2021).
39. Werley, C. A. et al. All-optical electrophysiology for disease modeling and pharmacological characterization of neurons. *Curr. Protoc. Pharmacol.* **78**, 11.20.1–11.20.24 (2017).
40. Buchanan, E. K. et al. Penalized matrix decomposition for denoising, compression, and improved demixing of functional imaging data. Preprint at *bioRxiv* https://doi.org/10.1101/334706 (2019).
41. Lim, S. T., Antonucci, D. E., Scannevin, R. H. & Trimmer, J. S. A novel targeting signal for proximal clustering of the Kv2.1 K+ channel in hippocampal neurons. *Neuron* **25**, 385–397 (2000).
42. Baker, C. A., Elyada, Y. M., Parra, A. & Bolton, M. M. Cellular resolution circuit mapping with temporal-focused excitation of soma-targeted channelrhodopsin. *eLife* **5**, e14193 (2016).
43. Abs, E. et al. Learning-related plasticity in dendrite-targeting layer 1 interneurons. *Neuron* **100**, 684–699 (2018).
44. Schuman, B. et al. Four unique interneuron populations reside in neocortical layer 1. *J. Neurosci.* **39**, 125–139 (2019).

45. Anastasiades, P. G., Collins, D. P. & Carter, A. G. Mediodorsal and ventromedial thalamus engage distinct L1 circuits in the prefrontal cortex. *Neuron* **109**, 314–330 (2021).
46. Ferguson, B. R. & Gao, W. J. PV interneurons: critical regulators of E/I balance for prefrontal cortex-dependent behavior and psychiatric disorders. *Front. Neural Circuits* **12**, 37 (2018).
47. Jouhanneau, J. S., Kremkow, J. & Poulet, J. F. A. Single synaptic inputs drive high-precision action potentials in parvalbumin expressing GABA-ergic cortical neurons in vivo. *Nat. Commun.* **9**, 1540 (2018).
48. Antonoudiou, P., Tan, Y. L., Kontou, G., Upton, A. L. & Mann, E. O. Parvalbumin and somatostatin interneurons contribute to the generation of hippocampal gamma oscillations. *J. Neurosci.* **40**, 7668–7687 (2020).
49. Dombeck, D. A., Harvey, C. D., Tian, L., Looger, L. L. & Tank, D. W. Functional imaging of hippocampal place cells at cellular resolution during virtual navigation. *Nat. Neurosci.* **13**, 1433–1440 (2010).
50. Ahmadi, N., Constandinou, T. G. & Bouganis, C. S. Estimation of neuronal firing rate using Bayesian adaptive kernel smoother (BAKS). *Plos ONE* **13**, e0206794 (2018).
51. van Welie, I., Roth, A., Ho, S. S., Komai, S. & Hausser, M. Conditional spike transmission mediated by electrical coupling ensures millisecond precision-correlated activity among interneurons in vivo. *Neuron* **90**, 810–823 (2016).
52. Feldman, D. et al. Optical pooled screens in human cells. *Cell* **179**, 787–799 (2019).
53. Mansoury, M., Hamed, M., Karmustaji, R., Al Hannan, F. & Safrany, S. T. The edge effect: a global problem. The trouble with culturing cells in 96-well plates. *Biochem. Biophys. Rep.* **26**, 100987 (2021).
54. Chien, M. P., Werley, C. A., Farhi, S. L. & Cohen, A. E. Photostick: a method for selective isolation of target cells from culture. *Chem. Sci.* **6**, 1701–1705 (2015).
55. Binan, L. et al. Opto-magnetic capture of individual cells based on visual phenotypes. *eLife* **8**, e45239 (2019).
56. Lee, D., Kume, M. & Holy, T. E. Sensory coding mechanisms revealed by optical tagging of physiologically defined neuronal types. *Science* **366**, 1384–1389 (2019).
57. Zimanyi, L., Cao, Y., Needleman, R., Ottolenghi, M. & Lanyi, J. K. Pathway of proton uptake in the bacteriorhodopsin photocycle. *Biochemistry* **32**, 7669–7678 (1993).
58. Brown, L. S. et al. The proton transfers in the cytoplasmic domain of bacteriorhodopsin are facilitated by a cluster of interacting residues. *J. Mol. Biol.* **239**, 401–414 (1994).
59. Ferrarese, L. et al. Dendrite-specific amplification of weak synaptic input during network activity in vivo. *Cell Rep.* **24**, 3455–3465 (2018).
60. Jouhanneau, J. S. & Poulet, J. F. A. Multiple two-photon targeted whole-cell patch-clamp recordings from monosynaptically connected neurons in vivo. *Front. Synaptic Neurosci.* **11**, 15 (2019).
61. Lambert, T. J. FPbase: a community-editable fluorescent protein database. *Nat. Methods* **16**, 277–278 (2019).
62. Hofherr, A., Fakler, B. & Klocker, N. Selective Golgi export of Kir2.1 controls the stoichiometry of functional Kir2.x channel heteromers. *J. Cell Sci.* **118**, 1935–1943 (2005).
63. Stockklausner, C., Ludwig, J., Ruppersberg, J. P. & Klocker, N. A sequence motif responsible for ER export and surface expression of Kir2.0 inward rectifier K(+) channels. *FEBS Lett.* **493**, 129–133 (2001).
64. Gradinaru, V. et al. Molecular and cellular approaches for diversifying and extending optogenetics. *Cell* **141**, 154–165 (2010).

Methods

DNA constructs

Constructs (Supplementary Table 1) were generated using the standard molecular cloning techniques. All of the new constructs and their sequences are available from Addgene.

Virus packaging

All of the lentivirus preparations were made in house using the second-generation lentivirus packaging system (Supplementary Methods). The high-titer QuasAr6a and Optopatch AAV2/9 viruses were obtained from the Janelia Vector Core or packaged in house (Supplementary Table 1). AAV2/9.hSyn::Cre.WPRE was obtained from UPenn Vector Core.

Engineering monoclonal spiking HEKs

The CheRiff-CFP$^+$ tet-on spiking HEK cells express $Na_V1.5$, rtTA3, CheRiff-CFP constitutively, as well as Kir2.1-CFP under a tetracycline-inducible promoter CMVtight (Supplementary Methods). After monoclonal selection the CheRiff-CFP$^+$ spiking HEK clones were optically screened for spiking behavior. The spikes were evoked with optogenetic stimulation (excitation at 490 nm) and visualized using a voltage-sensitive dye (BeRST, excitation at 635 nm)[33]. To obtain consistent experimental results we used only low passage-number cells and kept a master plate free of doxycycline.

Photopick screening of Arch-based GEVIs

The Photopick system was upgraded from a previously reported optical system[28] (Supplementary Methods). Before each screening experiment the digital micromirror device (DMD) projection of the 405 nm laser was recalibrated (Supplementary Methods).

Random mutations were introduced into the Archon1 opsin sequence through error-prone polymerase chain reaction. Single copies of the mutant GEVI were stably integrated into the CheRiff-CFP + tet-on spiking HEK cells via low-titer lentivirus infection (Supplementary Methods). The library cells were mixed with CheRiff-CFP$^+$ spiking HEK cells (spacer cells) at a ratio of 1:10. The mixed cells were plated in glass-bottomed dishes (Cellvis) homogenously (500,000 cells in a 14 mm well). The cells were allowed to grow for 40–50 h in Dox$^+$ medium to form a monolayer. Before imaging, the medium was replaced with the extracellular buffer containing 125 mM NaCl, 2.5 mM KCl, 3 mM $CaCl_2$, 1 mM $MgCl_2$, 15 mM HEPES and 30 mM glucose (pH 7.3).

In the 2.3 mm × 2.3 mm FOV (500 × 500 pixels), first, an mEos4a-channel image was taken (excitation, 490 nm LED, Thorlabs, M490L3; emission, GFP emission filter, 540/50 Semrock FF01-540/50). Next, the spiking HEK cell monolayer was broadly stimulated with the 490 nm pulses (2 mW mm^{-2}, 10 ms) from the top, and the voltage responses to optogenetic stimulations were recorded under the pseudo-TIRF (total internal reflection fluorescence) configuration (index-matching immersion oil Olympus, Z-81114; excitation, 635 nm laser, 100 W cm^{-2}; emission, Arch-emission filter, long-pass 700 nm; sampling rate:100 Hz). Each experiment run consisted of eight repeats (five blue light pulses with the red laser on, followed by five blue light pulses with the red laser off).

The 500 × 500 pixel FOV was segmented based on the mEOS-channel (excitation, 490 nm LED) image using standard Matlab image processing steps (Supplementary Methods). The Arch-channel movie (eight consecutive repeats) was first averaged over time, and then corrected for blue light crosstalk (via the time-average of the red laser-off epoch) and red-light excitation profile, and corrected for background fluorescence via spatial filtering (Matlab imtophat). The average intensity traces were extracted from each region of interest and corrected for photobleaching. The baseline fluorescence intensity was assigned as F_0. The averaged baseline-to-peak difference was assigned as ΔF. We used $\Delta F_{Arch}/\sqrt{F_{0,Arch}}$ as a proxy of shot noise-limited SNR.

A DMD mask was generated to illuminate the selected regions of interest (ROIs) for phototagging (excitation, 405 nm, 40 mW cm^{-2}, 10 min). Then the dish was moved to screen the next FOV. In a typical experimental run, the spiking HEK cells responded robustly to optogenetic stimulation throughout a time course of 6 h. A total of 20–25 FOVs were scanned to achieve good coverage of the entire dish, and each FOV contained 2,000–4,000 ROIs. From a single dish, 30,000–50,000 cells were scanned.

The cells were then trypsinized (1% trypsin, 5 min at 37 °C) to lift them from the dish and carefully transferred into a 15 ml Falcon tube. The cells were gently centrifuged to remove the trypsin and washed once with extracellular buffer. Then the cells were resuspended in the extracellular buffer and processed using FACS (Supplementary Fig. 1 and Methods) in less than 1 h after resuspension. The photoconverted cells were collected into fresh DMEM10 medium and cultured under the standard HEK cell culture condition to increase the population.

In each round of enrichment, two dishes (~90,000 library cells) were screened. After this, 7–10 days later, the enriched libraries from the two dishes were combined at a proportion corresponding to the number of originally collected cells and processed in the next round of enrichment. The remaining library cells were preserved in liquid nitrogen for sequencing. The frequency of mutations was analyzed with Illumina sequencing (Supplementary Methods).

Characterization of single mutants in HEK293T cells

The HEK293T cells expressing wild-type Archon1 or the single mutants were characterized on the ultra-widefield microscope ($F_{Citrine}$: excitation at 490 nm, GFP emission filter; F_{Arch}: excitation at 635 nm, Cy5 emission filter). The cells that were outliers for brightness (more than three standard deviations from the mean) in the Citrine channel or in the Arch channel were removed in the violin plot.

Concurrent imaging and electrophysiology of HEK293T cells

The GEVIs (Archon1, QuasAr6a, QuasAr6b) were cloned into the lentiviral FCMV (FUGW vector with the UbC promoter replaced by a cytomegalovirus (CMV) promoter) vector (HT63, HT103, HT110). HEK cells were infected at a low titer (multiplicity of infection < 0.1) and purified by FACS.

All imaging and electrophysiology experiments were performed in extracellular buffer. Concurrent whole-cell patch clamp and high-magnification fluorescence recordings were acquired on a custom-built, dual-view, inverted epifluorescence microscope equipped with an electrophysiology module described previously[16]. Filamented glass micropipettes were pulled to a tip resistance of 5–8 MΩ, and filled with internal solution containing 125 mM potassium gluconate, 8 mM NaCl, 0.6 mM $MgCl_2$, 0.1 mM $CaCl_2$, 1 mM EGTA, 10 mM HEPES, 4 mM Mg-ATP and 0.4 mM Na-GTP (pH 7.3), adjusted to 295 mOsm with sucrose. Whole-cell patch clamp recordings were performed with a MultiClamp 700B amplifier (Molecular Devices), filtered at 2 kHz with the internal Bessel filter and digitized with a National Instruments PCIE-6323 acquisition board at 10 kHz.

The GEVI fluorescence was excited by a 635 nm laser (420 W cm^{-2} unless otherwise indicated) filtered with a dichroic (Semrock; FF640-FDi01-25×36) and a Cy5-long-pass filter (708/75), and imaged with an sCMOS (scientific complementary metal oxide semiconductor) camera (Hamamatsu, ORCA-Flash 4.0). The citrine fluorescence was excited with a 488 nm laser (100–200 mW cm^{-2} unless otherwise indicated), filtered with a GFP filter (Semrock 525/30), and imaged with an EMCCD camera (Andor iXonEM+ DU-897E). All of the fluorescence recordings in Extended Data Fig. 4 (except for parts d and e) were performed at room temperature with a high-magnification water immersion objective (Olympus, ×60, numerical aperture (NA) 1.2). For photocurrent measurement, higher intensities at 635 nm (1,500 W cm^{-2}) and 488 nm (124 W cm^{-2}) were used to enhance any potential photocurrents. For the kinetics measurements (Extended

Data Fig. 4d,e) the glass-bottomed culture dish was maintained at 30 °C with a temperature controller (Warner Instruments, TC-344B). An air objective (Olympus, ×20, NA 0.8; excitation intensity of 635 nm laser: 330 W cm^{-2}) was used instead to reduce heat dissipation to the objective.

The Arch fluorescence recordings for voltage sensitivity measurements and for kinetics measurements were acquired at a frame rate of 996 Hz and 2,443 Hz, respectively. In the kinetics measurement, the fluorescence responses from 50 pulses of 100 ms voltage steps (−70 mV to +30 mV, 5 Hz, 50% duty cycle) were averaged for each cell and fitted with a biexponential model to calculate the fast and slow components of the activation and deactivation kinetics.

High-throughput imaging of hippocampal neurons

Primary E18 (embryonic day 18) rat hippocampal neurons (21,000 per cm^2; dissociated from fresh, never frozen, BrainBits cat. no. SDEHP) were cocultured with primary rat glia (27,000 per cm^2) in custom 96-well plates (ibidi GmbH; low-absorption, low-autofluorescence cyclic olefin copolymer (COC) foil substrate and clear COC walls). To minimize variations between samples, neurons were seeded from a single pool of cells. Lentivirus for Archon1-EGFP, Archon1-Citrine (HT075), QuasAr6b-Citrine (HT111) and QuasAr6b-Citrine (HT114) was packaged in parallel under identical conditions. Neurons were transduced after 6 days in culture with 0.33 µl lentivirus encoding CheRiff-EBFP2 driven by the synapsin promoter, and varying doses (1.19 µl, 1.78 µl, 2.67 µl, 4 µl, 6 µl, 9 µl) of the voltage sensor variants, also driven by the synapsin promoter. Each condition was replicated in four wells. Three FOVs were measured for each well.

Functional Optopatch imaging was performed after 14 days in culture on the Firefly microscope[65] (see Supplementary Methods for the detailed imaging and optogenetic stimulation protocol). The imaging system was fully automated and ran with no human intervention. The whole plate was scanned automatically with motorized stages so that the three FOVs in each well were evenly spaced. Focus was also automatically adjusted for each FOV.

Spiking neurons were automatically detected and segmented using a principal component analysis–independent component analysis (PCA–ICA)-based Matlab code[39]. The algorithm identifies spatially compact sets of pixels (neuron masks) that co-vary in time with action potential positive-going voltage transients. Sources for which the action potential height did not exceed the baseline noise by at least a factor of 3 were discarded.

Characterization of QuasAr6a and QuasAr6b in brain slice

For the acute slice experiment (Fig. 3k–p, Extended Data Fig. 7 and Supplementary Fig. 3), expression was achieved through intracranial injection of QuasAr6a/b AAVs ($2–3 \times 10^{12}$ genome copies per ml Optopatch + 10^{11} genome copies per ml hSyn-Cre, diluted in PBS) in newborn (postnatal day 0–1) wild-type CD1 pups. For intracranial injection, cryo-anesthetized pups were injected in the left hemisphere, 1.0 mm lateral and 1.0 mm anterior to lambda, starting from a −1.0 mm depth. Diluted virus (40 nl, 60 nl min^{-1}) was injected at 0.1 mm increments as the pipette was withdrawn.

Coronal brain slices (350 µm) were prepared from CD1 mice of either sex between postnatal days 14 and 25. Standard whole-cell recording was performed at 34 °C during continuous perfusion at 2 ml min^{-1} with artificial cerebrospinal fluid. Cortical layer 2/3 neurons were visualized using a custom-built microscope described below. The whole-cell internal solution consisted of 8 mM NaCl, 130 mM $KMeSO_3$, 10 mM HEPES, 5 mM KCl, 0.5 mM EGTA, 4 mM Mg-ATP, 0.3 mM Na_3-GTP. The pH was adjusted to 7.2–7.3 with KOH and osmolarity was set to 290–295 mOsm l^{-1}. Borosilicate glass pipettes were used with a resistance of 3–5 MΩ (1B150F-4; WPI). Patch clamp recordings were acquired and filtered at 10 kHz with the internal Bessel filter using a Multiclamp 700B (Molecular Devices) and digitized with a PCIE-6323 data acquisition device (National Instruments) at 100 kHz. During the recording, the perfusion buffer was maintained at 33–34 °C with an in-line heater. Following the whole-cell configuration, membrane capacitance and membrane resistance were estimated under voltage clamp mode. Measurements of resting membrane potential, rheobase and spike rates were made under current clamp mode. Rheobase was defined as the minimum current step (in 500 ms duration) required to elicit at least one spike. Whole-cell recordings were monitored and analyzed in Matlab.

The voltage imaging optical system was originally described in ref. [16] with a few modifications (Supplementary Methods). The Arch-channel fluorescence was acquired with a ×25 water immersion objective (Olympus XLPLN25XSVMP2), at 996.3 Hz (1 kHz) with an sCMOS camera (Hamamatsu ORCA-Flash 4.0). The control software generated a metadata output for precise mapping between the amplifier readout and the camera frame counts. In the analysis in which the 100 kHz current clamp recordings were downsampled to 1 kHz, the membrane potential readouts in the same camera frame were averaged and aligned with the camera frame timing.

Immunostaining of the slice and confocal imaging

Expression was achieved through intracranial injection of AAVs (5×10^{12} genome copies per ml Optopatch + 10^{11} genome copies per ml hSyn-Cre) in postnatal day 0–2 wild-type C57BL/6J pups. Coronal slices were prepared with the injected pups 21 days after virus injection. The slices were fixed in 1% paraformaldehyde for 3–4 h and immunostained to visualize the HA tag (primary antibody: HA Tag recombinant rabbit monoclonal antibody, ThermoFisher, RM305, 2,000× dilution; second antibody: goat anti-Rabbit IgG (H + L) cross-adsorbed secondary antibody conjugated with Cyanine5, ThermoFisher, A10523, 500× dilution). The mounted slices (VECTASHIELD Antifade Mounting Medium H-1000, Vectorlabs, H-1000-10) were imaged on LSM880 Airyscan (excitation at 488 nm for EGFP; excitation at 635 nm for Cy5).

In vivo voltage imaging

The cranial window surgery for imaging layer 1 cortex and hippocampus CA1 was based on previously published protocols[16,49,66] (Supplementary Methods). The imaging set-up was originally described in ref. [20] with a few modifications (Supplementary Methods).

Head-fixed animals were imaged in various degrees of anesthesia or full wakefulness. For imaging experiments under deep anesthesia, 1–1.5% isoflurane was supplied, and the dose was adjusted throughout the imaging session to maintain a stable breathing rate. For imaging experiments under light anesthesia, animals were first given chlorprothixene (0.2 mg ml^{-1}, 5 µl g^{-1} mouse weight). In the imaging session, 0.4–0.7% isoflurane was supplied to keep the animal in a state of semi-wakefulness, with occasional body movements. In all experiments involving anesthesia the animal was kept on a heating pad (WPI, ATC2000) to maintain stable body temperature at 37 °C, and their eyes were kept moist using ophthalmic eye ointment. A typical imaging session lasted 1–2 h, after which the animal generally recovered within 5 min. For imaging experiments under full wakefulness, the animal was first habituated to head restraint in a body tube prior to the imaging sessions, and no extra heating was necessary.

Imaging was performed with a ×25 water immersion objective (Olympus XLPLN25XWMP2, 2 mm working distance, NA = 1.05), or a ×10 water immersion objective (Olympus XLPLN10XSVMP, 8 mm working distance, NA = 0.6). To ensure a stable water interface between the window and the ×10 objective, a 3D-printed adapter hat was attached to the headplate temporarily with vacuum grease during the imaging session.

For voltage imaging, red laser excitation was targeted to the cell membrane or whole soma with holographic optics (see Supplementary Table 3 for the light intensity, patterning method and frame rate). In our experience, membrane-focal illumination gives better SNR when a high-NA objective (for example, ×25, NA = 1.05) was used and the cells

show little motion. When the cells were experiencing stronger movement, soma-targeted illumination helped to reduce motion artifacts.

Optogenetic stimulation with patterned blue light

For optogenetic stimulation, the DMD patterned the blue light to target the soma. The structural image in the GFP channel was excited with a low level of blue light (<1 mW mm^{-2}) and imaged with a GFP emission filter. The pixel bitmap containing the region of interest masks was created based on the GFP channel image. When the experiments required the blue light intensity to change globally for all of the ROIs, the blue intensity was modulated with an acousto-optic tunable filter upstream of the DMD, with a range from 0 to 25 mW mm^{-2}. When the experiments involved different blue light waveforms for different ROIs (for example, experiments in Fig. 5), the intensity was controlled by randomly switching on a fraction of pixels within the region of interest. The pre-defined sequence of pixel bitmaps was loaded into the on-board RAM (random access memory) on the DMD and timed with digital pulses sent from the data acquisition board to the DMD.

Double Optopatch in NDNF$^+$ cells

For the double Optopatch experiments on NDNF$^+$ neurons, the blue light intensity was modulated by randomly switching on a fraction of DMD pixels in each cell mask. For each ramp stimulation, a series of DMD masks were generated and displayed on the DMD as a movie. By varying the fractions of 'on' pixels independently for each cell mask, different optogenetic stimulation waveforms and strengths could be achieved for each cell.

Before the two-way inhibitory connection test, the two optically targeted cells were sequentially stimulated with varying blue light intensities (upward linear ramp followed by downward linear ramp, maximum intensity 25 mW mm^{-2}) to ensure that both cells responded to the optogenetic activation, and the stimulation was specific to the intended cell. Due to possible light scatter from one-photon optogenetic activation, we avoided closely spaced cell pairs (<40 µm). Because both the intrinsic firing pattern and the maximum firing rate of NDNF$^+$ cells, as well as the expression level of somCheRiff, could be variable from one cell to another, we typically adjusted the strength of optogenetic stimulation to achieve a maximal spiking rate in the 'presynaptic' cell of up to 50 Hz at the maximum of the ramp stimulation. The strength of optogenetic stimulation for the 'postsynaptic' cell was set to be approximately half of its maximum spike rate.

Data analysis

Data were analyzed and plotted with homemade code written in MATLAB. The detailed methods are described in Supplementary Information, which includes the following sections: extracting the voltage-sensitive fluorescence from in vitro and ex vivo imaging; extracting the voltage-sensitive fluorescence from in vivo imaging; spike detection and trace normalization; calculation of spike SNRs and waveforms; estimation of spike rate with BAKS; test for bias for or against reciprocal connections among NDNF cells; estimate of optical crosstalk between parvalbumin pairs; and quantifying the gap junction-induced spikelet in parvalbumin cells.

Statistics

Statistical tests were performed in MATLAB (MathWorks). For two-sample comparisons of a single variable, a two-tailed Student's *t*-test was used when the sample size was >50 (high-throughput Optopatch in cultured neurons). For datasets in which the sample size was small ($n < 40$) or had a non-Gaussian distribution, the two-sided Wilcoxon rank-sum test was used. When calculating the in vivo GEVI metrics (Fig. 4 and Extended Data Fig. 8), outliers (value that is more than three scaled median absolute deviations) were excluded. For the hippocampal parvalbumin recordings, the SNR were calculated separately for cells imaged with the ×25 or the ×10 objectives, while for the optical spike widths, the two sets of data were pooled together. The in vivo experiments were not randomized, and the investigators were not blinded to the experimental conditions. Sample size was as large as practical. Recordings of non-spiking neurons were excluded from analysis.

Materials availability

Plasmids encoding QuasAr6a or QuasAr6b are available from Addgene. The tet-on spiking HEK cells are available from ATCC (cat. nos. crl-3479 and crl-3480).

Reporting summary

Further information on research design is available in the Nature Portfolio Reporting Summary linked to this article.

Data availability

Data used in the study are available upon reasonable request to A.E.C.

References

65. Nguyen, C. et al. Simultaneous voltage and calcium imaging and optogenetic stimulation with high sensitivity and a wide field of view. *Biomed. Opt. Express* **10**, 789–806 (2019).
66. Goldey, G. J. et al. Removable cranial windows for long-term imaging in awake mice. *Nat. Protoc.* **9**, 2515–2538 (2014).

Acknowledgements

The authors thank B.L. Sabatini and O. Yizhar for advice and discussion; C. Dulac for the PV-Cre mouse line; M. Andermann and J. Fernando for advice on cranial window surgery; T.D. Green, K. Williams, Urs Böhm, A. Preecha, H. Dahche, Y. Adam and G. Testa-Silva for technical assistance and advice; E.M. Moult for advice on statistics; M.P. Chien for advice on pooled screening; E. Miller for the BeRST1 dye; B. Arnold from Harvard FAS Informatics for assistance with Illumina sequencing data analysis; the Bauer Core Facility at Harvard University for FACS service; the Biopolymers Facility at Harvard Medical School for next-generation sequencing; and Harvard Center for Biological Imaging (RRID:SCR_018673) for infrastructure and support on confocal imaging. This work was supported by the Howard Hughes Medical Institute (A.E.C. and K.D.), NIH grants 1RF1MH117042 and 1R01NS126043 (A.E.C.), a Vannevar Bush Faculty Fellowship N00014-18-1-2859 (A.E.C.), a National Science Foundation QuBBE QLCI grant OMA-2121044 (A.E.C.), a Helen Hay Whitney Fellowship (L.Z.F.) and a Merck fellowship from the Life Science Research Foundation (J.D.W.-C.).

Author contributions

H.T. and A.E.C. conceived and designed the study. H.T. designed all of the experiments and conducted the experiments except for the high-throughput Optopatch assay in cultured neurons and electrophysiology in acute slice. B.G. and V.P. assisted with the optics on the ultra-widefield microscope for pooled screening. H.C.D, H.T. and J.D.W.-C. improved the structured illumination microscope for in vivo imaging based on an earlier version built by L.Z.F. H.C.D. developed the Matlab control software for the structured illumination microscope. H.T., C.A.W. and G.B.B. designed the high-throughput Optopatch experiment in cultured neurons for characterizing GEVIs. H.U, H.S. and J.J. performed the high-throughput Optopatch assay. P.P. performed electrophysiological experiments in acute brain slice. Y.Q. assisted with the in vivo imaging experiments. S.B. prepared the cultured neurons for GEVI characterization and performed the mouse husbandry. L.Z.F. and K.D. contributed to the in vivo validation of the GEVIs in the early stage. H.T. and A.E.C. analyzed the data and wrote the manuscript. A.E.C. supervised the research.

Competing interests

A.E.C. is a founder of Q-State Biosciences. A.E.C. and H.T. filed a patent on the genetically encoded voltage indicators described in this study. All other authors have no competing interests.

Additional information

Extended data are available for this paper at https://doi.org/10.1038/s41592-022-01743-5.

Supplementary information The online version contains supplementary material available at https://doi.org/10.1038/s41592-022-01743-5.

Correspondence and requests for materials should be addressed to Adam E. Cohen.

Peer review information *Nature Methods* thanks Srdjan Antic, Xue Han, and the other, anonymous, reviewer for their contribution to the peer review of this work. Primary Handling Editor: Rita Strack, in collaboration with the *Nature Methods* team.

https://doi.org/10.1038/s41592-022-01743-5

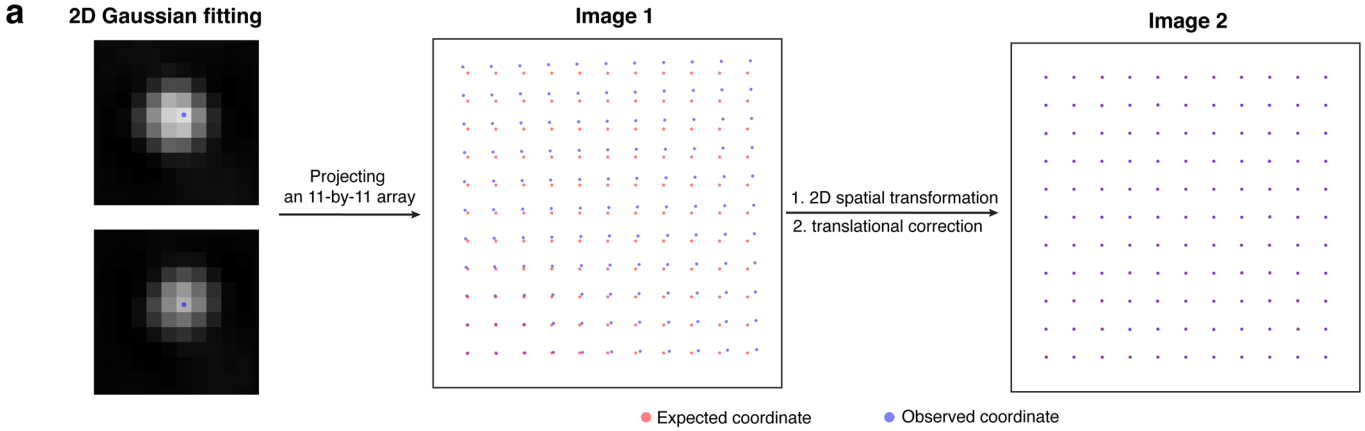

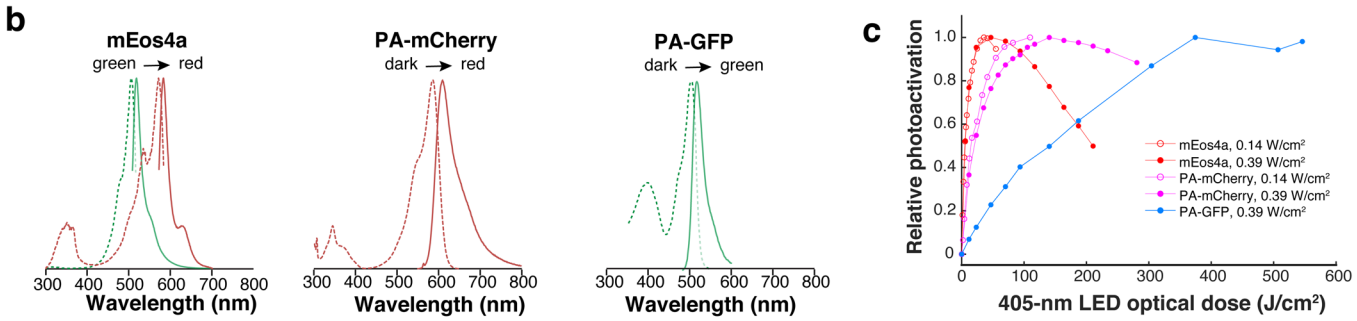

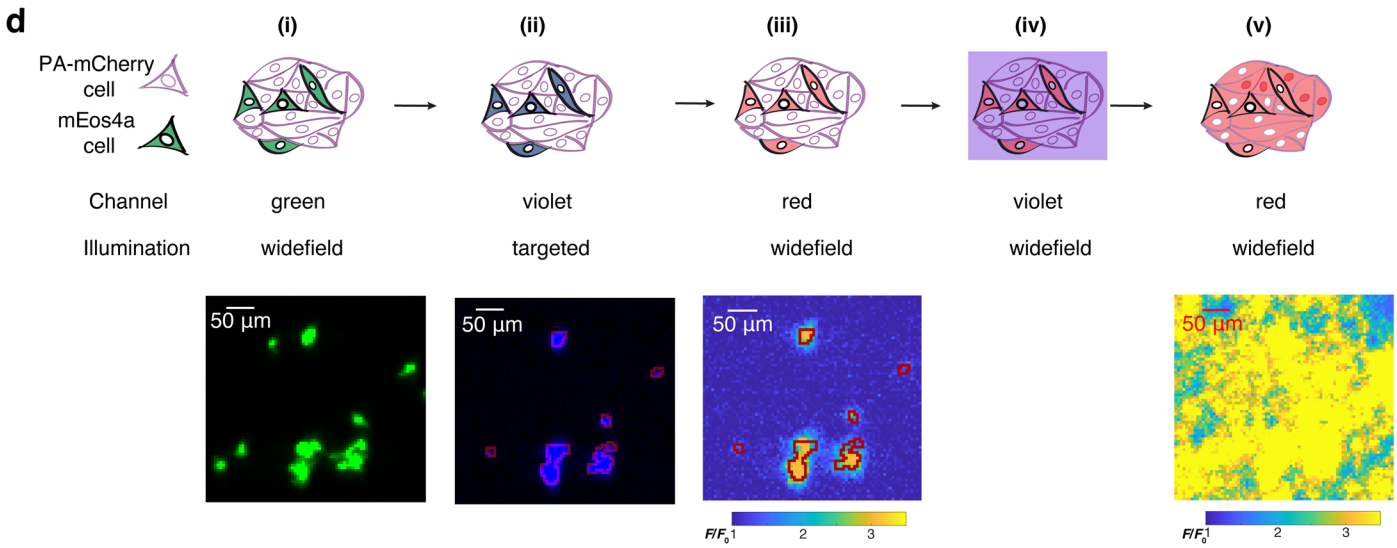

Extended Data Fig. 1 | Calibration of Photopick, an imaging-based method for isolating mammalian cells from pooled culture (Related to Fig. 1). a. Procedure for registering the DMD and camera pixels. An 11 × 11 grid of spots was projected onto a homogeneous exposure target. The observed locations in the camera were used to develop a piecewise-linear transformation to map DMD pixels onto camera pixels. In this example, the registration reduced the average projection error from 11.6 pixels to 0.22 pixels. **b.** Fluorescence excitation and emission spectra of three phototaggable FPs, PA-GFP, PA-mCherry, and mEos4a. For mEos4a, the spectra are given in the pre-activation state (green) and post-activation state (red). For the other FPs, the activated spectra are shown. **c.** Phototransformation efficiency vs. optical dose of 405-nm LED light. The decreased signal under prolonged illumination is due to photobleaching. **d.** Selective phototagging of mEos4a$^+$ cells embedded in PA-mCherry$^+$ cells (mEos4a$^+$:PA-mCherry$^+$ = 1:20; n = 1 trial). Based on the green channel image (i), a mEOS4a mask was created for targeted photoconversion of mEos4a with violet (ii). The red channel image shows that the phototagging was highly specific (iii). The monolayer of cells was then broadly illuminated with violet light (iv) to drive the photoactivation of PA-mCherry$^+$ cells (v). Targeted violet illumination of the mEos4$^+$ cells resulted in selective phototagging of mEos4a$^+$ cells but not surrounding PA-mCherry$^+$ cells.

https://doi.org/10.1038/s41592-022-01743-5

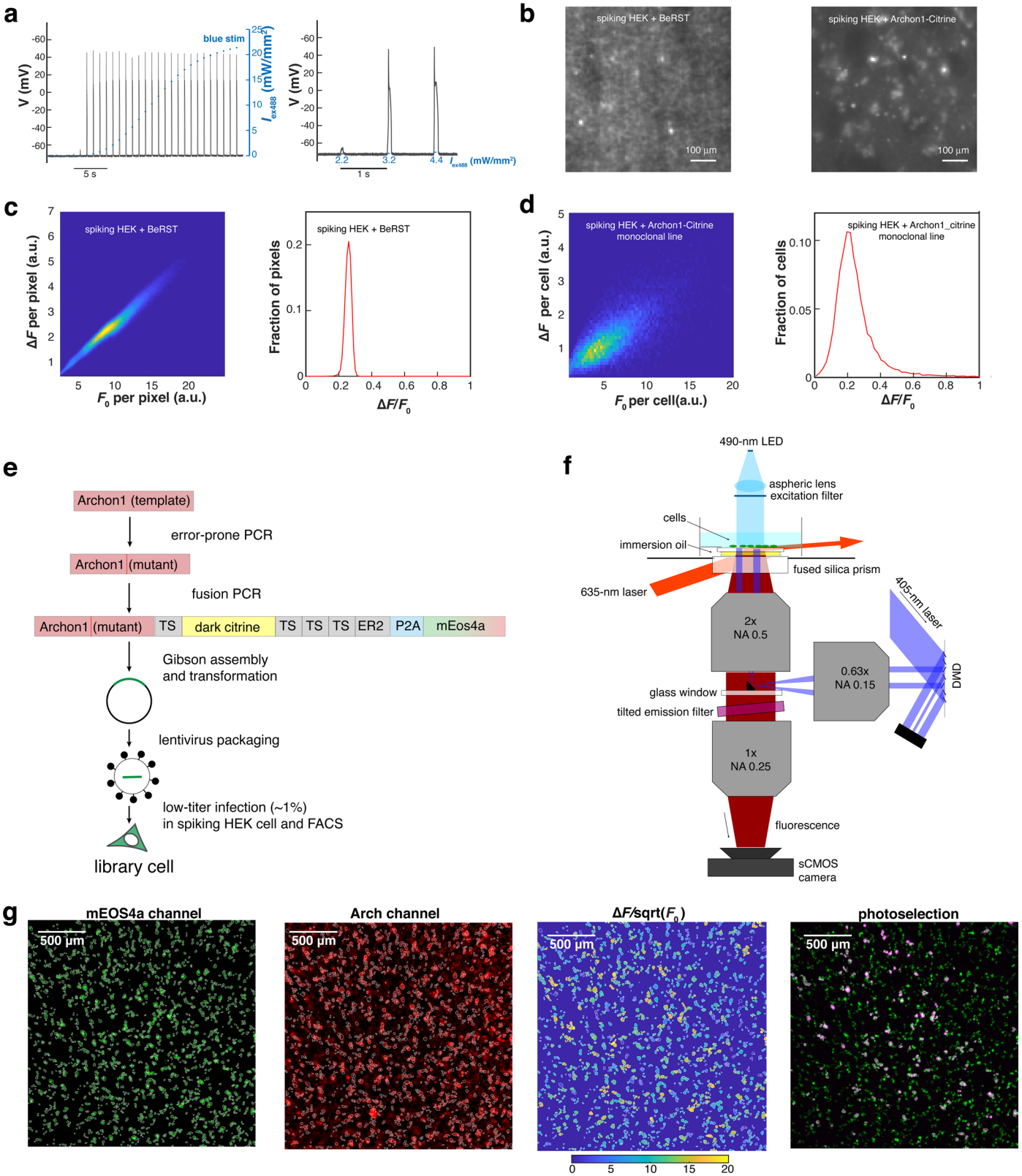

Extended Data Fig. 2 | See next page for caption.

https://doi.org/10.1038/s41592-022-01743-5

Extended Data Fig. 2 | Video-based pooled screen for mutations that enhance the performance of Arch-derived GEVIs (Related to Fig. 2). a. Current clamp measurement of membrane potential in spiking HEK cells reveals 'all-or-none' spiking in response to increasing optogenetic stimulation ($n = 2$ trials; exc. 488 nm). Left: membrane potential in response to optical stimuli of increasing strength (0–22 mW/mm^2). Right: enlarged view showing the threshold transition. **b**. Fluorescence image (exc. 635 nm) of spiking HEK cell monolayer stained with BeRST1 (left) or expressing Archon1-Citrine (right). In the Archon1-Citrine image, the presence of the spacer cells (spiking HEK cells that did not express Archon1-Citrine) enabled individual cells to be resolved. **c**. Distribution of membrane potential changes in a spiking HEK cell monolayer, reported via imaging of a voltage-sensitive dye BeRST1, plotted for each pixel. Left: heatmap of ΔF vs. F_0 for all pixels in a 2.3 × 2.3 mm FOV (500 × 500 pixels). Right: histogram of $\Delta F/F_0$. The distribution had a fractional width (S.D./mean) of 8% (mean 0.25, S.D. 0.02; 99th percentile: 0.29). **d**. Distribution of Archon1 baseline brightness (F_0) and voltage sensitivity ($\Delta F/F_0$) in a monoclonal Archon1-expressing spiking HEK cell monolayer, plotted for each cell ($n = 20900$ cells). Left: heatmap of ΔF vs. F_0 for all cells in a 2.3 × 2.3 mm FOV (500 × 500-pixels). Right: histogram of $\Delta F/F_0$. The distribution had a fractional width (S.D./mean) of 43% (mean 0.23, S.D. 0.10; 99th percentile: 0.54), substantially broader than the distribution for BeRST1. **e**. Workflow for the generation of the library cells. **f**. Optical system for video-based pooled screening. **g**. Image analysis for a representative FOV (the same as shown in Fig. 2e, f). The example was, from left to right: 1) ROIs generated by 'Watershed' image segmentation in the mEos4a channel (exc: 490 nm; EGFP emission filter). 2) Baseline fluorescence (F_0) image in the Arch channel (exc: 635 nm; Arch emission filter). 3) Heatmap of $\Delta F/\sqrt{F_0}$ for individual ROIs. Here $\Delta F/\sqrt{F_0}$ is used as a proxy for shot noise limited for SNR. 4) Overlay of the patterned violet light (pseudo-color red; exc. 405 nm; CFP emission filter) and mEos4a image (exc: 490 nm; EGFP emission filter).

https://doi.org/10.1038/s41592-022-01743-5

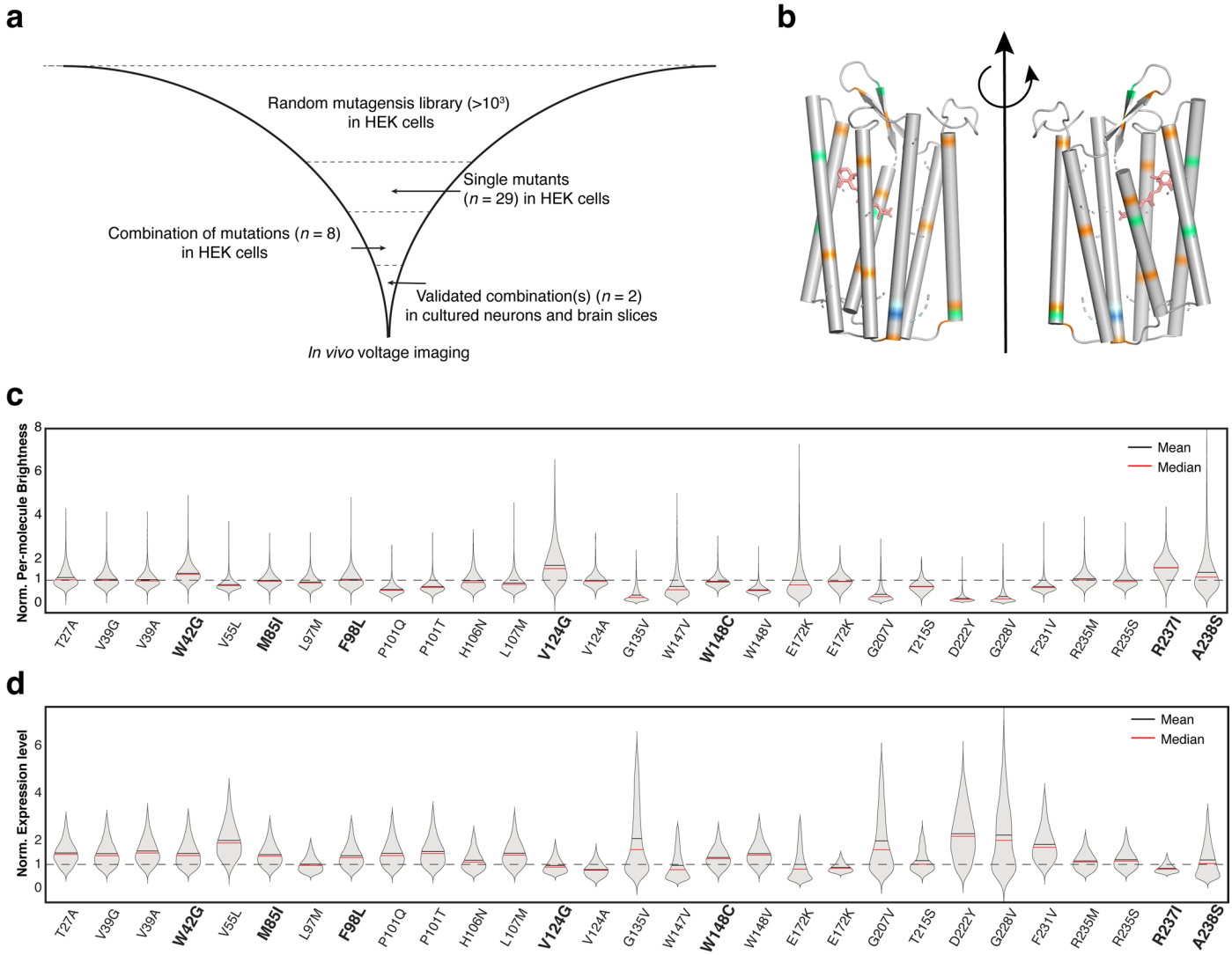

Extended Data Fig. 3 | Engineering QuasAr6a and QuasAr6b (Related to Fig. 2). **a**. Pipeline for engineering improved GEVIs. **b**. Comparison of the previously reported mutations (*orange*),[26,34] and newly identified mutations in this study (lime-green, pale cyan and blue assigned in accordance with Fig. 3a). **c**. Violin plot for the per-molecule brightness ($F_{Arch}/F_{Citrine}$) of single mutants expressed in HEK cells. The per-molecule brightness was normalized by the average per-molecule brightness of Archon1-Citrine in HEK cells. The residues selected for engineering QuasAr6a/b are shown in bold. **d**. Violin plot for the expression level ($F_{Citrine}$) of single mutants expressed in in HEK cells. The values were normalized to the average expression level of Archon1-Citrine in HEK cells.

https://doi.org/10.1038/s41592-022-01743-5

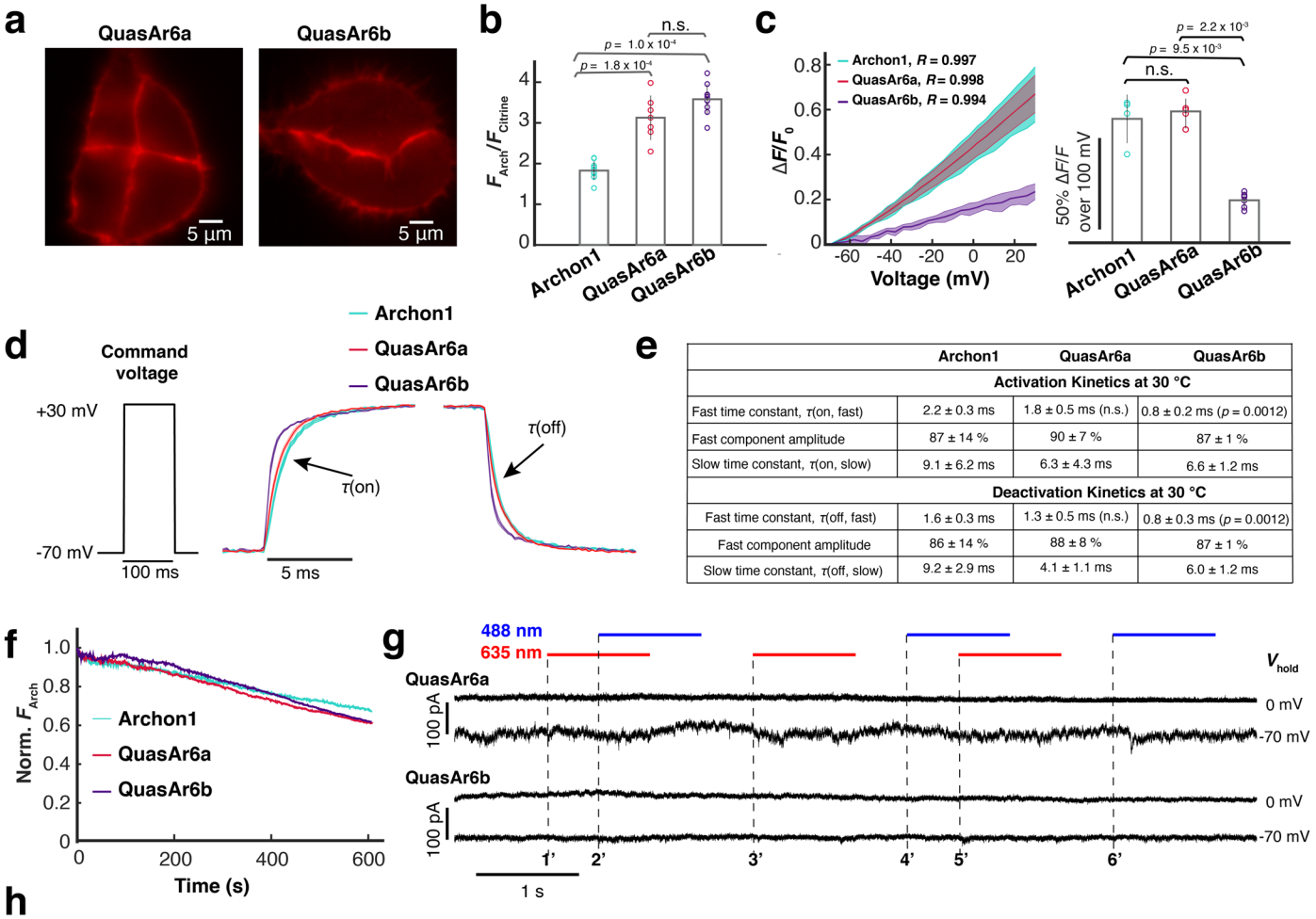

	Archon1	QuasAr6a	QuasAr6b
Activation Kinetics at 30 °C			
Fast time constant, τ(on, fast)	2.2 ± 0.3 ms	1.8 ± 0.5 ms (n.s.)	0.8 ± 0.2 ms (p = 0.0012)
Fast component amplitude	87 ± 14 %	90 ± 7 %	87 ± 1 %
Slow time constant, τ(on, slow)	9.1 ± 6.2 ms	6.3 ± 4.3 ms	6.6 ± 1.2 ms
Deactivation Kinetics at 30 °C			
Fast time constant, τ(off, fast)	1.6 ± 0.3 ms	1.3 ± 0.5 ms (n.s.)	0.8 ± 0.3 ms (p = 0.0012)
Fast component amplitude	86 ± 14 %	88 ± 8 %	87 ± 1 %
Slow time constant, τ(off, slow)	9.2 ± 2.9 ms	4.1 ± 1.1 ms	6.0 ± 1.2 ms

h

	Holding potential (mV)	Steady holding current (pA)				Transient change in holding current (pA)			
		Dark	Red only	Blue only	Blue + red	Red on	Blue on	Red after blue	Blue after red
QuasAr6a	0	12 ± 6	14 ± 5	10 ± 5	13 ± 6	+ 0.3	+ 0.7	+ 0.1	+ 0.5
	-70	-172 ± 13	-180 ± 11	-175 ± 15	-184 ± 9	- 8.3	-1.1	+1.6	- 4.4
QuasAr6b	0	34 ± 6	38 ± 6	31 ± 5	39 ± 6	- 0.9	+ 0.1	- 0.2	+ 0.2
	-70	-23 ± 4	-25 ± 4	-25 ± 4	-26 ± 4	-1.1	+1.4	-1.6	-1.6

Extended Data Fig. 4 | Characterization of QuasAr6a-Citrine and QuasAr6b-Citrine in HEK293T cells (Related to Fig. 3). **a**. Arch-channel (exc: 635 nm, em: 670–746 nm) fluorescence images of QuasAr6a-Citrine and QuasAr6b-Citrine expressed in HEK cells (n > 20 cells for each construct). **b**. Relative brightness per molecule of Archon1-Citrine (n = 10 cells), QuasAr6a-Citrine (n = 7 cells), and QuasAr6b-Citrine (n = 10 cells) measured as a ratio of whole-cell F_{Arch} to $F_{Citrine}$. n.s. not significant, p > 0.05; ***p : 0.0001- 0.001 (two-sided Wilcoxon rank-sum test). The brightness per molecule was calculated as the ratio of Arch-channel fluorescence (exc. 635 nm; 420 W/cm^2) to Citrine-channel fluorescence (exc. 488 nm; 0.1 W/cm^2). **c**. Voltage sensitivity measured by concurrent voltage clamp and fluorescence in HEK cells. Left: Fractional fluorescence change vs. membrane voltage; shading: S.D. Right: Voltage sensitivity (ΔF/F per 100 mV: Archon1-Citrine, n = 4 cells; QuasAr6a-Citrine, n = 5 cells; QuasAr6b-Citrine, n = 6 cells). n.s. not significant, p > 0.05; **p: 0.01 - 0.05 (two-sided Wilcoxon rank-sum test). Error bars mean ± S.D. **d**. Voltage step-response kinetics measured by recording the average fluorescence change during a 100-ms voltage step from −70 mV to +30 mV (Archon1-Citrine, n = 6 cells; QuasAr6a-Citrine, n = 7 cells; QuasAr6b-Citrine, n = 7 cells); shading: SEM. Measurements were performed at 30 °C and a frame rate of 2,443 Hz. **e**. Summary of the step-response kinetic data at 30 °C, fitted with a biexponential model. Compared with Archon1, QuasAr6b showed significant improvement in both activation and deactivation kinetics. **p: 0.01 - 0.05 (two-sided Wilcoxon rank-sum test). **f**. Photobleaching by 635 nm laser (420 W/cm^2) over 10 min (n = 2 cells for each construct). All constructs showed < 40% photobleaching over 10 min. S.D. **g**. Voltage clamp measurement of HEK cells expressing QuasAr6a or QuasAr6b showed negligible photocurrents under either 488 nm, 635 nm or combined illumination at either −70 mV or 0 mV holding potentials (488 nm: 124 W/cm^2; 635 nm: 1500 W/cm^2). All photocurrents were less than the variability in baseline holding current and were < 10 pA (in most cases < 2 pA). The onsets of red or blue illumination are indicated with dashed lines and numbered sequentially. **h**. Summary of the photocurrent measurement in **g**. All values are mean ± S.D. Transient changes in the holding current were calculated as the differences of the mean holding currents during the 20-ms epochs before and after the light was turned on. Red-on: average of 1′ and 3′; Blue-on: average of 4′ and 6′; Red after blue: 5′; Blue after red: 2′.

https://doi.org/10.1038/s41592-022-01743-5

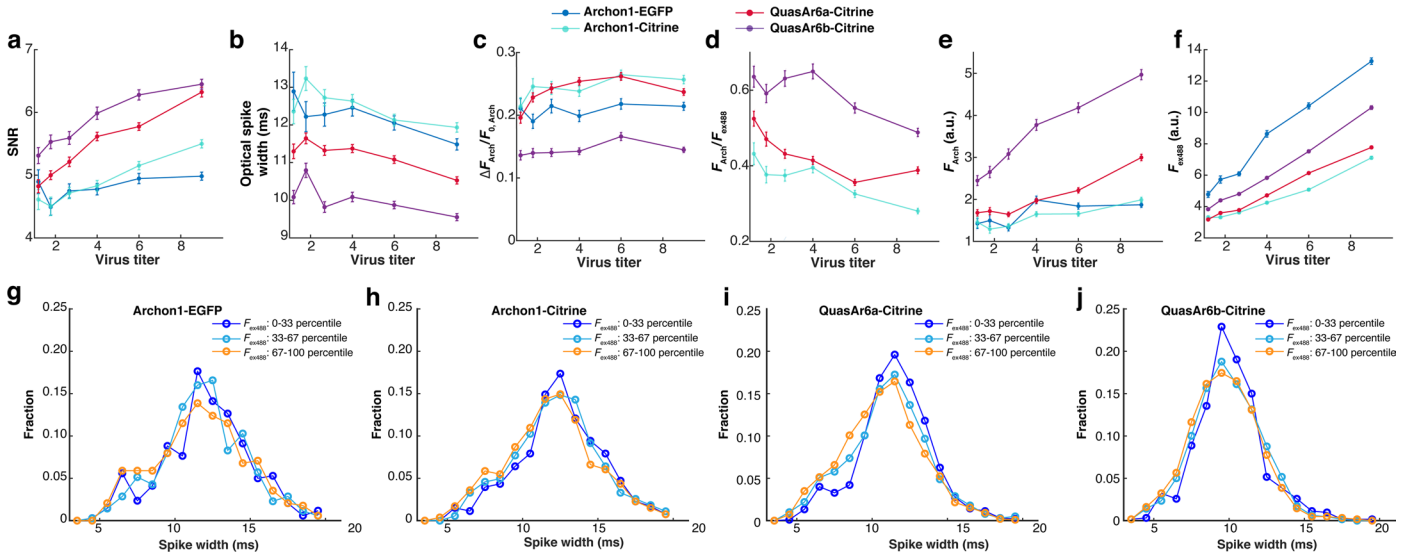

k

Relative titer	Archon1-EGFP		Archon1-Citrine		QuasAr6a-Citrine		QuasAr6b-Citrine	
	total	well-average	total	well-average	total	well-average	total	well-average
1.19	37	9.3 ± 2.6	59	14.7 ± 3.4	159	39 ± 13	103	25.8 ± 5.9
1.78	52	13 ± 4.7	104	26 ± 13	275	69 ± 11	150	38 ± 15
2.67	103	26 ± 3	170	43 ± 13	369	92 ± 6	221	55 ± 7
4	166	41 ± 17	271	68 ± 20	588	147 ± 11	318	80 ± 5
6	267	67 ± 11	419	105 ± 5	717	179 ± 12	491	123 ± 10
9	405	101 ± 13	583	146 ± 16	843	211 ± 14	596	149 ± 8

Extended Data Fig. 5 | Metrics of GEVI performance in high-throughput Optopatch assay in cultured neurons (Related to Fig. 3). **a**. SNR: spike height divided by the root mean square (RMS) baseline noise. **b**. Optical spike width: full width measured at 80% below the action potential peak. Note offset vertical axis. **c**. $\Delta F_{Arch}/F_{0,Arch}$: voltage sensitivity as a ratio of the increase in fluorescence during a spike to the baseline fluorescence. **d**. F_{Arch}/F_{ex488}: per-molecule brightness as a ratio of baseline fluorescence in the Arch channel to the baseline fluorescence in the Citrine channel. The data for Archon1-EGFP were omitted because EGFP and Citrine fluorescence are not directly comparable. **e**. $F_{0,Arch}$: baseline fluorescence in the Arch channel (exc: 635 nm). **f**. F_{ex488}: baseline fluorescence in the Citrine channel (exc: 488 nm). In all measurements, the relative titers (from low to high) were: 1.19, 1.78, 2.67, 4, 6, 9. Each data point represents the average from 4 wells. The intensive properties (**b, c, d**) are largely insensitive to virus titer while the extensive properties (**a, e, f**) scale with virus titer. Error bars: SEM. **g-j**. Distribution of spike widths for neurons with low (0–33 percentile), medium (33–67 percentile) and high (67–100 percentile) expression level (F_{ex488}). The distributions were similar across expression levels, for all GEVIs. **k**. Cell counts in high-throughput Optopatch assay. The total and well-average (mean ± S.D.) number of optically detected spiking cells, for each combination of GEVI construct and virus titer. At the higher titers, the well-to-well variations in detected cells within a given condition were ~10%, much smaller than the 200–300% differences between GEVI variants.

https://doi.org/10.1038/s41592-022-01743-5

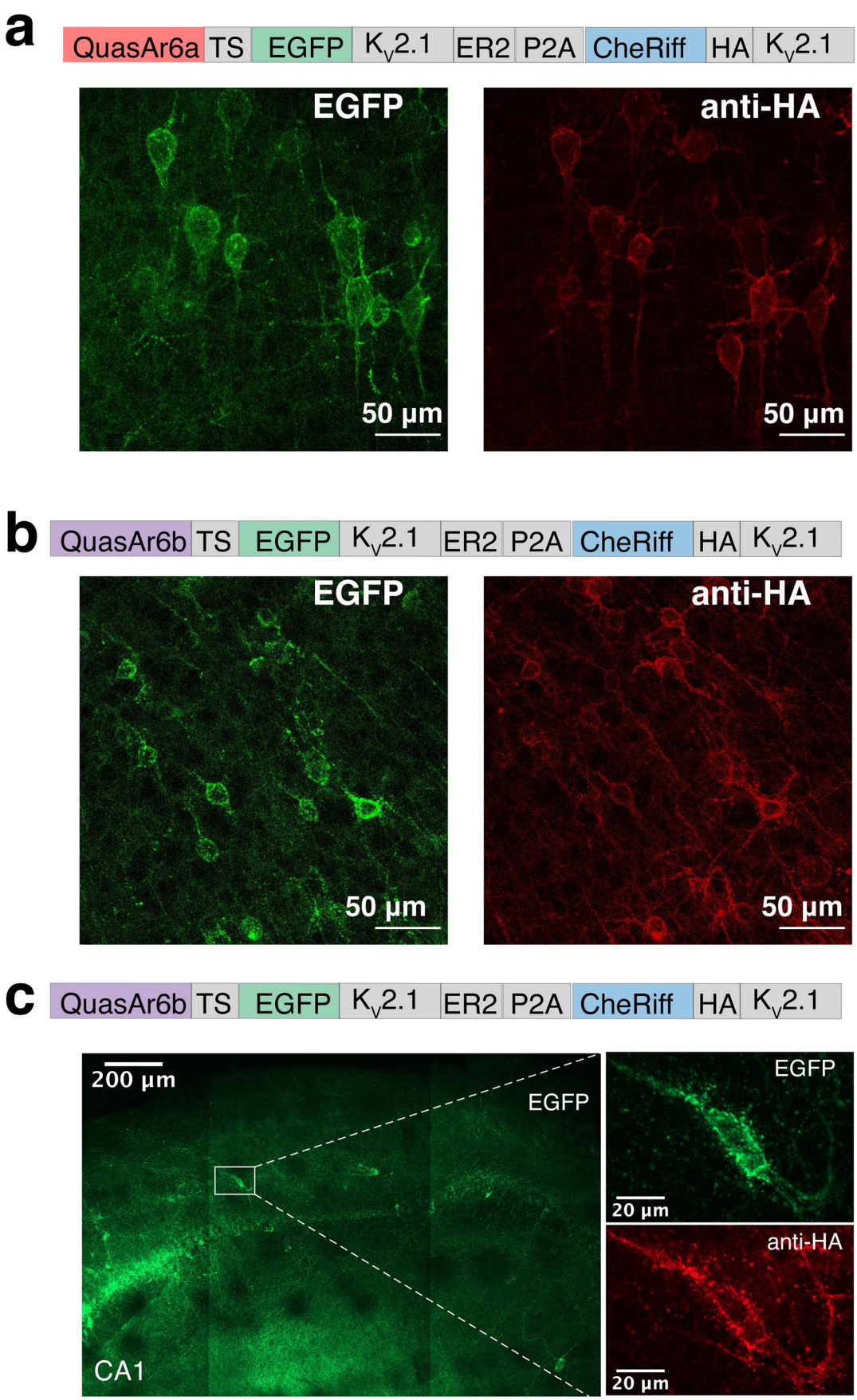

Extended Data Fig. 6 | See next page for caption.

https://doi.org/10.1038/s41592-022-01743-5

Extended Data Fig. 6 | Expression of somQuasAr6a- and somQuasAr6b-based Optopatch in mouse brain (Related to Fig. 3). a, b. Confocal images showing bicistronic expression of soma-targeted QuasAr6a-EGFP (somQuasAr6a) in L5 somatosensory cortex or soma-targeted QuasAr6b-EGFP (somQuasAr6b) with somCheRiff-HA in L5 cingulate cortex. The expression of GEVIs was visualized in the EGFP channel and the expression of CheRiff in the Cy5 channel (anti-HA immunostaining). **c.** Confocal images showing bicistronic expression of soma-targeted QuasAr6b-EGFP (somQuasAr6b) with somCheRiff-HA in hippocampal PV cells in a PV-Cre$^+$ mouse.

https://doi.org/10.1038/s41592-022-01743-5

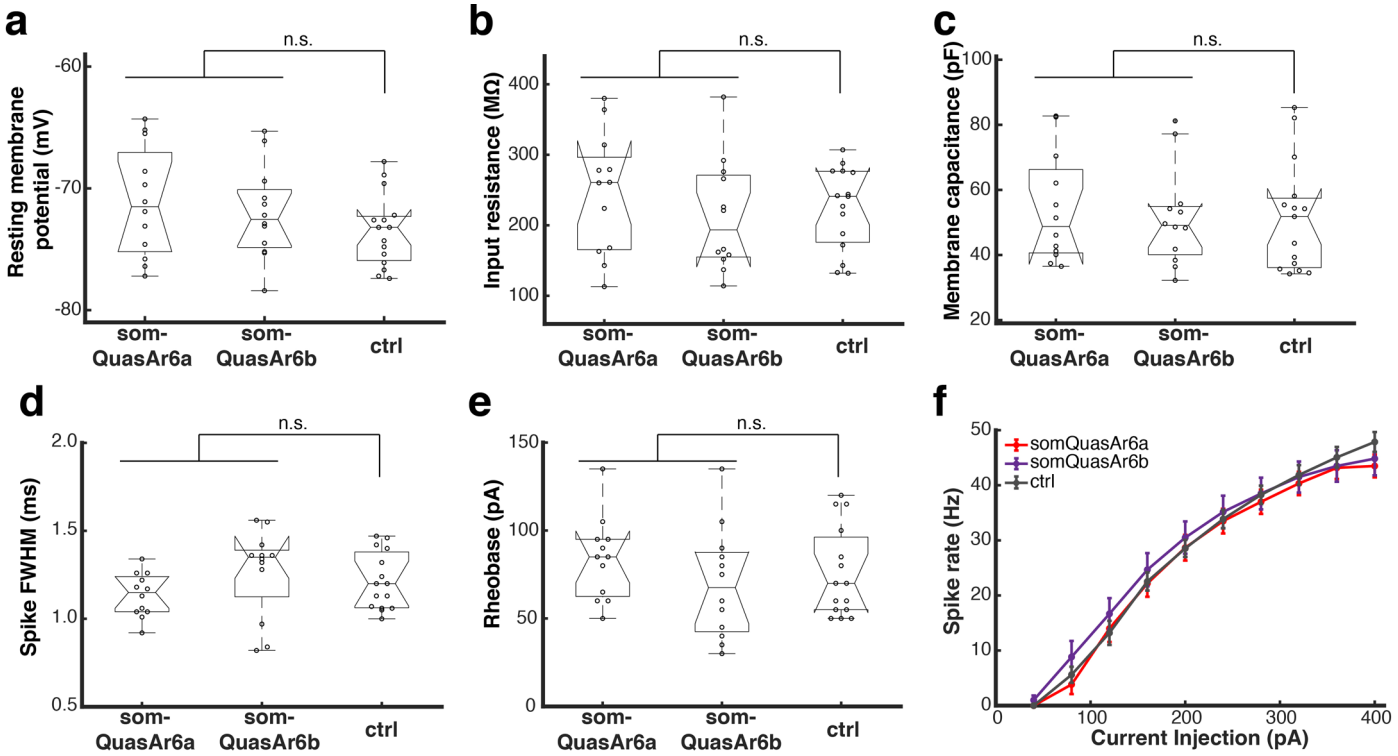

Extended Data Fig. 7 | Effect of GEVI expression on membrane electrical properties and excitabilities (Related to Fig. 3). Mouse L2/3 cortical neurons expressing Arch-based GEVIs were measured by patch clamp in acute slices (somQuasAr6a, $n = 2$ animals, 12 cells; somQuasAr6b, $n = 2$ animals, 12 cells). Non-expressing cells from the same slices were used as the control ($n = 4$ animals, 15 cells). Box plots: central mark indicates median, bottom edge 25th percentile, top edge 75th percentile, whiskers most extreme data points excluding outliers, '+' symbol outliers. n.s., not significant, two-sided Wilcoxon rank-sum test. Error bars in **f**: SEM.

https://doi.org/10.1038/s41592-022-01743-5

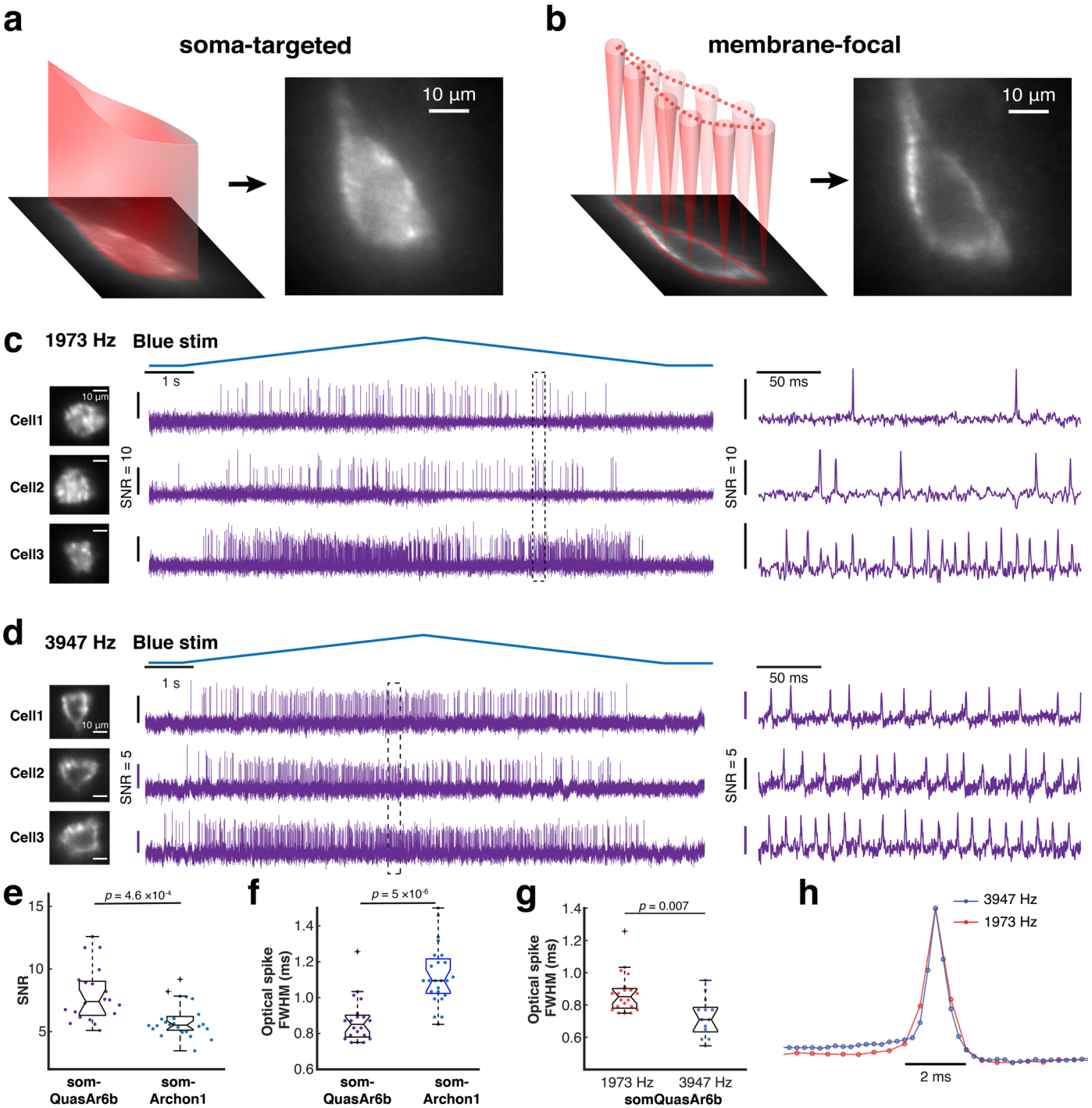

Extended Data Fig. 8 | Optopatch in hippocampal PV cells (Related to Fig. 4). **a, b**. Two ways of patterning 635-nm light to the cell with a spatial light modulator (SLM). Left: soma-targeted. Right: membrane-focal. The cell shown here was a hippocampal PV neuron (imaged with 25x, NA = 1.05 objective). Compared to whole-soma illumination, membrane-focal illumination provides improved shot noise-limited SNR but greater sensitivity to motion artifacts. **c**, **d**. Representative Optopatch traces of somQuasAr6b+ PV cells, recorded at 2 kHz (1973 Hz) and 4 kHz (3947 Hz) with a 10× objective (NA 0.6). Magnified views of the boxed regions are shown on the right. For the 2 kHz-imaging experiment, soma-targeted illumination was used. For the 4 kHz-imaging experiment, membrane-focal illumination was used. Due to this difference in the optical configuration, the SNRs from these two datasets were not compared in the analysis. **e**. Comparison of the in vivo SNR of QuasAr6b (n = 20 cells, 3 animals) and Archon1 in PV cells (n = 24 cells, 2 animals), two-sided Wilcoxon rank-sum test. **f**. Comparison of optical spike full width at half-maximum (FWHM) of optogenetically triggered spikes in PV cells, imaged with somQuasAr6b and somArchon1 at a 2 kHz frame rate, two-sided Wilcoxon rank-sum test. **g**. Comparison of optical spike FWHM of optogenetically triggered spikes in PV cells, imaged with somQuasAr6b a 2 kHz (n = 20 cells, 3 animals) and 4 kHz (n = 13 cells, 2 animals) frame rate, two-sided Wilcoxon rank-sum test. **h**. Spike-triggered average fluorescence waveform of optogenetically trigged spikes recorded with somQuasAr6b a 2 kHz (n = 20 cells, 3 animals) and 4 kHz (n = 13 cells, 2 animals) frame rate.

https://doi.org/10.1038/s41592-022-01743-5

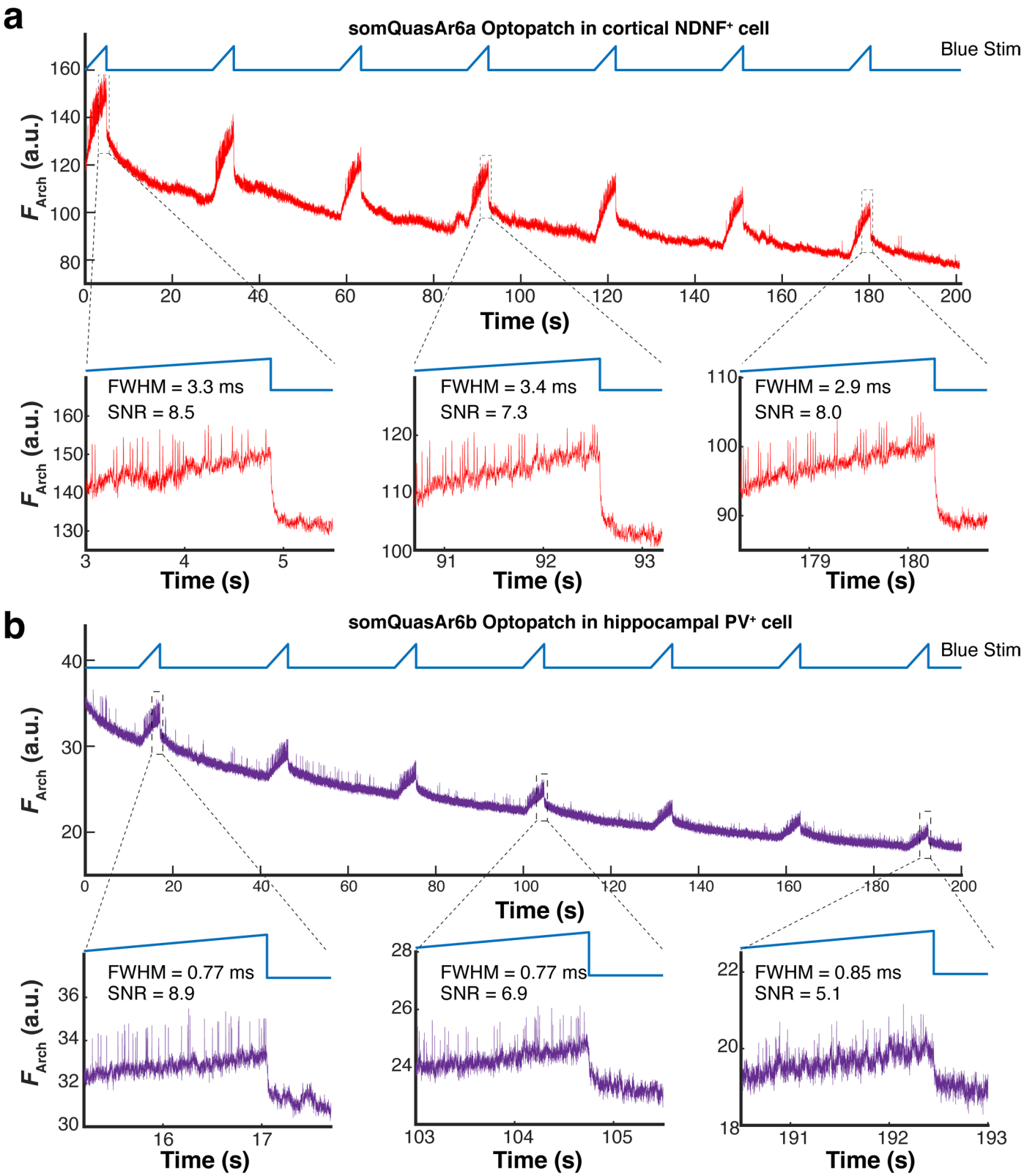

Extended Data Fig. 9 | Photostability of QuasAr6a and QuasAr6b in vivo (Related to Fig. 4). a. Raw Arch-channel fluorescence trace without baseline or photobleaching correction of a Layer 1 NDNF cell (visual cortex) expressing QuasAr6a-based Optopatch, imaged for 200 seconds at 1 kHz ($n = 2$ cells). The 635-nm power delivered to the cell was 4 mW. **b.** Raw Arch-channel fluorescence trace of a hippocampal PV cell expressing QuasAr6b-based Optopatch, imaged for 200 seconds at 2 kHz ($n = 2$ cells). The 635-nm power delivered to the cell was 8 mW. The measurement was done in anesthetized animals. The fluorescence traces were the raw traces directly extracted from cell mask and not corrected for background. The SNR and FWHM was calculated for the all the optogenetically evoked spikes in the magnified region.

https://doi.org/10.1038/s41592-022-01743-5

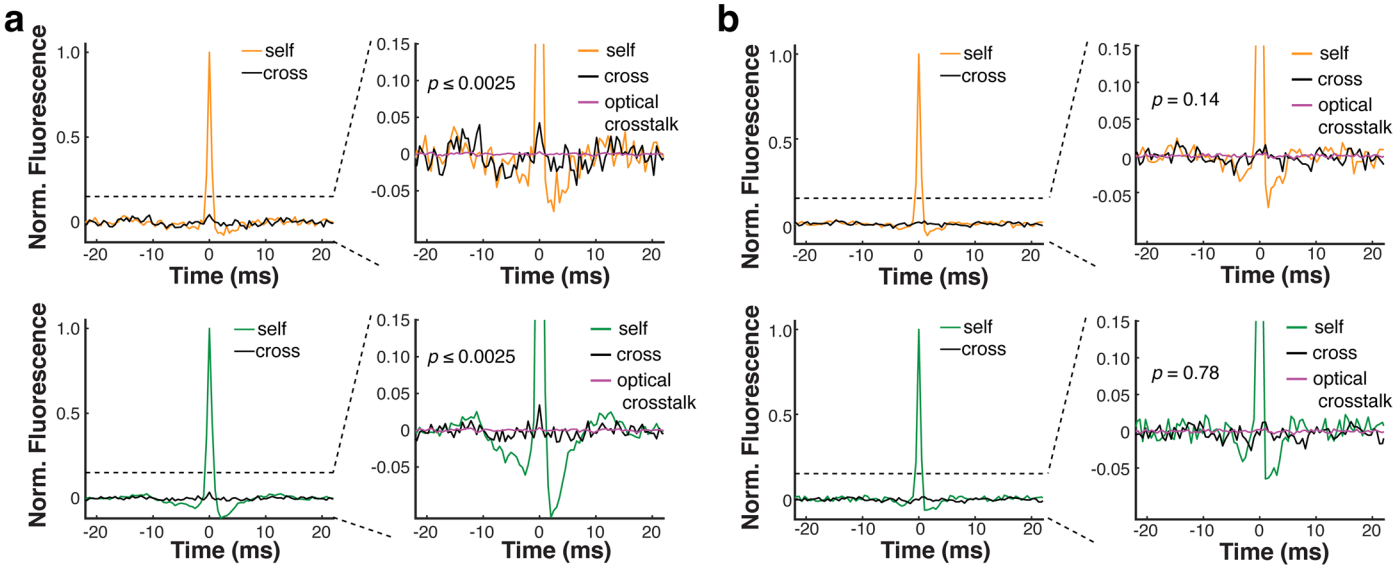

Extended Data Fig. 10 | Additional examples of electrical coupling between hippocampal PV cells (Related to Fig. 6). a. An example where gap junction-induced spikelets were detected between PV pairs in both directions. The inter-soma distances were 90 µm. **b.** An example where no gap junction-induced spikelet was detected between the PV pair (inter-soma distance = 298 µm).

nature methods

Article

https://doi.org/10.1038/s41592-022-01743-5

Video-based pooled screening yields improved far-red genetically encoded voltage indicators

In the format provided by the authors and unedited

Contents

REAGENT or RESOURCE	SOURCE	IDENTIFIER
Bacterial and Virus Strains		
AAV2/9.hSyn::Cre.WPRE	UPenn Vector Core	N/A
AAV2/9.hSyn::DiO:SomQuasAr6a-EGFP.WPRE	In house	N/A
AAV2/9.hSyn::DiO:SomQuasAr6b-EGFP.WPRE	In house	N/A
AAV2/9.hSyn::DiO:SomQuasAr6a-EGFP-P2A-somCheRiff-HA.WPRE	Janelia Viral Tools	N/A
AAV2/9.hSyn::DiO:SomQuasAr6b-EGFP-P2A-somCheRiff-HA.WPRE	Janelia Viral Tools	N/A
AAV2/9.hSyn::DiO:SomArchon1-EGFP-P2A-somCheRiff-HA.WPRE	Janelia Viral Tools	N/A
Chemicals, Peptides, and Recombinant Proteins		
doxycycline hyclate	Sigma	Cat# D9891
Blasticidin S	Sigma	Cat# 203350
Puromycin dihydrochloride from *Streptomyces alboniger*	Sigma-Aldrich	Cat# P7255
Geneticin® Selective Antibiotic (G418 Sulfate)	ThermoFisher	Cat# 11811023
HA Tag recombinant rabbit monoclonal antibody	ThermoFisher	Cat# RM305
goat anti-Rabbit IgG (H+L) cross-adsorbed secondary antibody conjugated with Cy-5	ThermoFisher	
Experimental Models: Cell Lines		
HEK293T	ATCC	ATCC CRL-3216
tet-on spiking HEK cell	This work	ATCC CRL-3479
CheRiff-EGFP tet-on spiking HEK cell	This work	ATCC CRL-3480
CheRiff-CFP tet-on spiking HEK cell	This work	N/A
Experimental Models: Organisms/Strains		
C57BL/6 wild-type mice	Charles River	Strain Code 027

NDNF-Cre transgenic mice	Jackson Lab	Stock #028536
PV-Cre transgenic mice	Catherine Dulac	Stock #017320
Recombinant DNA constructs		
TDG004 pLenti_CMVtight_Kir2.1-CFP	This work	Addgene #178820
pLenti-CMV-rtTA3-Blast	Eric Campeau	Addgene #26429
HT028 FCMV_CheRiff-EGFP	This work	Addgene #178821
HT041 FCMV_CheRiff-CFP	This work	Addgene #136636
HT063 FCMV_Archon1-Citrine	This work	
HT075 Fsyn_FAS(Cre-off) Archon1-Citrine	This work	
HT091 FCMV_Archon1-dark citrine_P2A_mEos4a	This work	
HT103 FCMV_QuasAr6a-Citrine	This work	Addgene #178822
HT110 FCMV_QuasAr6b-Citrine	This work	Addgene #178823
HT111 Fsyn_FAS(Cre off)_QuasAr6a-Citrine	This work	Addgene #178824
HT114 Fsyn_FAS(Cre-off)_QuasAr6b-Citrine	This work	Addgene #178825
HT107 pAAV_hSyn-DiO-SomQuasAr6a_EGFP-P2A-somCheRiff_HA	This work	Addgene #178826
HT109 pAAV_hSyn-DiO-SomQuasAr6a_EGFP	This work	Addgene # 190878
HT115 pAAV_hSyn-DiO-SomQuasAr6b_EGFP-P2A-somCheRiff_HA	This work	Addgene #178827
HT116 pAAV_hSyn-DiO-SomQuasAr6a_EGFP	This work	Addgene # 190879
Software and Algorithms		
MATLAB R2016b - 2020a	Mathworks	Matlab
Labview 2014, 2015	National Instruments	Labview
FCS Express 7 Research	De Novo Software	FCS Express
NoRMCorre	[1]	https://github.com/flatironinstitute/NoRMCorre

Others		
Custom-designed ultra-widefield microscope	2	N/A
Custom-designed structured illumination microscope	3	N/A

Supplementary Table 1. List of reagents and materials

	Cell type	Constructs tested	Set-up	Metrics	Related Figures
In vitro	HEK293T cells	1.QuasAr6a-Citrine 2.QuasAr6b-Citrine 3.Archon1-Citrine	High-magnification, widefield inverted microscope + electrophysiology	per-molecule brightness; voltage sensitivity (F-V); kinetics; photostability; non-linear photophysics	Extended Data Fig.4b-f Supplementary Figure 3g
In vitro	HEK293T cells	1.QuasAr6a-Citrine 2.QuasAr6b-Citrine	High-magnification, widefield inverted microscope + electrophysiology	trafficking; photocurrent	Extended Data Fig.4a,g,h
In vitro	Rat hippocampal neurons	1.QuasAr6a-Citrine 2.QuasAr6b-Citrine	Confocal microscope	trafficking	Fig.3b
In vitro	Rat hippocampal neurons	1.QuasAr6a-Citrine 2.QuasAr6b-Citrine	High-magnification, widefield inverted microscope + electrophysiology	voltage sensitivity (F-V);	Fig.3c
In vitro	Rat hippocampal neurons	1.QuasAr6a-Citrine 2. QuasAr6b-Citrine 3. Archon1-Citrine 4. Archon1-EGFP (co-expression with CheRiff-CFP)	low-magnification, widefield inverted microscope	SNR; optical spike width; voltage sensitivity ($\Delta F/F_0$ per spike); expression level; brightness; per-molecule brightness	Fig.3d-j; Extended Data Fig.5
Ex vivo	Mouse cortical and hippocampal PV neurons, fixed slice	1. somQuasAr6a-P2A- somCheRiff_HA 2. somQuasAr6b-P2A-somCheRiff_HA	Confocal microscope	expression and trafficking	Extended Data Fig.6
Ex vivo	Mouse cortical neurons in acute slice	1.somQuasAr6a-EGFP 2.somQuasAr6b-EGFP	High-magnification, widefield upright microscope + electrophysiology	impact on cell electrophysiological properties; optical spike waveform; non-linear photophysics;	Fig.3k-p; Extended Data Fig.7; Supplementary Figure 3g
In vivo	Mouse cortex, NDNF+ neurons	1.somQuasAr6a-P2A-somCheRiff_HA 2. somQuasAr6b-P2A-somCheRiff_HA 3. somArchon1-P2A-somCheRiff_HA	Structured illumination upright microscope	SNR; optical spike widths; optical spike waveform; photostability	Fig.4a-e; Extended Data Fig.9
In vivo	Mouse hippocampus CA1, PV+ neurons	1.somQuasAr6b-P2A-somCheRiff_HA 2.somArchon1-P2A-somCheRiff-HA	Structured illumination upright microscope	SNR; optical spike widths; optical spike waveform; photostability	Fig.4f-l; Extended Data Fig.8,9

Supplementary Table 2. Summary of the experiments characterizing QuasAr6a and QuasAr6b.

Cell type	Related Figures	Objective	Patterning	Intensity (Exc. 635; mW)	Frame rate (Hz)
NDNF	Fig. 4a-e	25x	Membrane-focal	5	996
NDNF	Fig. 5	25x	Soma-targeted	3~4	996
PV	Extended Data Fig.9	25x	Soma-targeted	4	996
PV	Fig. 4f-i	25x	Membrane-focal	10	1973
PV	Extended Data Fig. 8	10x	Soma-targeted	10	1973
PV	Extended Data Fig. 8	10x	Membrane-focal	10	3947
PV	Fig. 6	10x	Soma-targeted	7~8	1973
PV	Extended Data Fig.9	25x	Soma-targeted	8	1973

Supplementary Table 3. Summary of the conditions for *in vivo* imaging

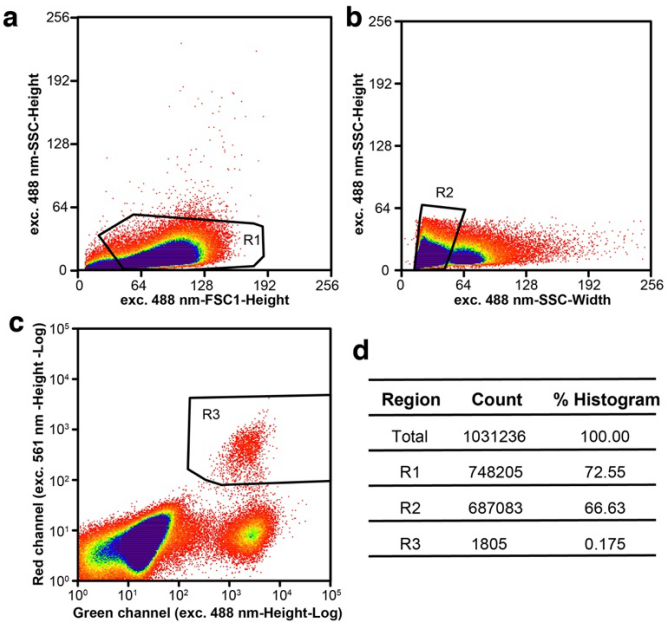

Region	Count	% Histogram
Total	1031236	100.00
R1	748205	72.55
R2	687083	66.63
R3	1805	0.175

Supplementary Figure 1. The FACS gating strategy to isolate the phototagged library cells. FSC: forward Scatter. SSC: side-scatter. After removal of cell debris (**a**), cells within R1 were further purified to remove doublet cells (**b**). Cells within R2 were selected based on the green channel (exc.488 nm) and red channel (exc.561 nm) signal (**c**). The double-positive cells within in R3 were collected and cultured. **d**. Statistics for each Region of Interest.

```
                1                                                          60
Arch(D95N)      MDPIALQAGYDLLGDGRPETLWLGIGTLLMLIGTFYFLVRGWGVTDKDAREYYAVTILVP
QuasAr1         MDPIALQAGYDLLGDGRPETLWLGIGTLLMLIGTFYFLVRGWGVTDKDAREYYAVTILVS
QuasAr2         MVSIALQAGYDLLGDGRPETLWLGIGTLLMLIGTFYFLVRGWGVTDKDAREYYAVTILVS
QuasAr3         MVSIALQAGYDLLGDGRPETLWLGIGTLLMLIGTFYFLVRGWGVTDKDAREYYAVTILVS
paQuasAr3       MVSIALQAGYDLLGDGRPETLWLGIGTLLMLIGTFYFLVRGWGVTDKDAREYYAVTILAS
NovArch         MVSIALQAGYDLLGDGRPETLWLGIGTLLMLIGTFYFLVRGWGVTDKDAREYYAVTILAS
Archon2         MVSIALQAGYDLLGDGRPETLWLGIGTLLMLIGTFYFLVRGWGVTDKDAREYYAVPILVS
Archon1         MVSIALQAGYDLLGDGRPESLWLGIGTLLMLIGTFYFLVRAWGETDKDAREYYAVTILVS
QuasAr6a        MVSIALQAGYDLLGDGRPESLWLGIGTLLMLIGTFYFLVRAGGETDKDAREYYAVTILVS
QuasAr6b        MVSIALQAGYDLLGDGRPESLWLGIGTLLMLIGTFYFLVRAGGETDKDAREYYAVTILVS

                61                                                         120
Arch(D95N)      GIASAAYLSMFFGIGLTEVTVGGEMLDIYYARYANWLFTTPLLLLDLALLAKVDRVTIGT
QuasAr1         GIASAAYLSMFFGIGLTEVSVGGEMLDIYYARYAHWLFTTPLLLLHLALLAKVDRVTIGT
QuasAr2         GIASAAYLSMFFGIGLTEVSVGGEMLDIYYARYAQWLFTTPLLLLHLALLAKVDRVTIGT
QuasAr3         GIASAAYLSMFFGIGLTEVSVGGEMLDIYYARYAQWLFTTPLLLLHLALLAKVDRVTIGT
paQuasAr3       GIASAAYLSMFFGIGLTEVSVGGEMLDIYYARYAQWLFTTPLLLLHLALLAKVDRVTIGT
NovArch         GIASAAYLSMFFGIGLTEVSVGGEMLDIYYARYAQWLFTTPLLLLHLALLAKVDRVTIGT
Archon2         GIASAAYLSMFFGIGLTEVPVGGEMLDIYYARYAHWLFSTPLLLLDLALLAKVDRVIIGT
Archon1         GIASAAYLSMFFGIGLTEVPVGGEMLNIYYARYAQWLFTTPLLLLHLALLAKVDRVTIGT
QuasAr6a        GIASAAYLSMFFGIGLTEVPVGGEILNIYYARYAQWLLTTPLLLLHLALLAKVDRVTIGT
QuasAr6b        GIASAAYLSMFFGIGLTEVPVGGEILNIYYARYAQWLLTTPLLLLHLALLAKVDRVTIGT

                121                                                        180
Arch(D95N)      LVGVDALMIVTGLIGALSHTAIARYSWWLFSTICMIVVLYFLATSLRSAAKERGPEVAST
QuasAr1         LVGVDALMIVTGLIGALSHTAIARYSWWLFSTICMIVVLYVLATSLRSAAKERGPEVAST
QuasAr2         LVGVDALMIVTGLIGALSHTAIARYSWWLFSTICMIVVLYVLATSLRSAAKERGPEVAST
QuasAr3         LVGVDALMIVTGLIGALSHTAIARYSWWLFSTICMIVVLYVLATSLRSAARERGPEVAST
paQuasAr3       LVGVDALMIVTGLIGALSHTAIARYSWWLFSTICMIVVLYVLATSLRSAARERGPEVAST
NovArch         LVGVDALMIVTGLIGALSHTAIARYSWWLFSTICMIVVLYVLATSLRSAARERGPEVAST
Archon2         LVGVDALMIVTGLIGALSHTAIARYSWWLFSTICMIVVLYVLATSLRSAAKERGPEVAST
Archon1         LVGVDALMIVTGLIGTLSHTAIARYSWWLFSTICMIVVLYVLATSLRSAAKERGPEVAST
QuasAr6a        LVGGDALMIVTGLIGTLSHTAIARYSWCLFSTICMIVVLYVLATSLRSAAKERGPEVAST
QuasAr6b        LVGGDALMIVTGLIGTLSHTAIARYSWCLFSTICMIVVLYVLATSLRSAAKERGPEVAST

                181                                                        240
Arch(D95N)      FNTLTALVLVLWTAYPILWIIGTEGAGVVGLGIETLLFMVLDVTAKVGFGFILLRSRAIL
QuasAr1         FNTLTALVLVLWTAYPILWIIGTEGAGVVGLGIETLLFMVLDVTAKVGFGFILLRSRAIL
QuasAr2         FNTLTALVLVLWTAYPILWIIGTEGAGVVGLGIETLLFMVLDVTAKVGFGFILLRSRAIL
QuasAr3         FNTLTALVLVLWTAYPILWIIGTEGAGVVGLGIETLLFMVLDVTAKVGFGFILLRSRAIL
paQuasAr3       FNTLTALVLVLWTAYPILWIIGTEGAGVVGLGIETLLFMVLDVTAKVGFGFILLRSRAIL
NovArch         FNTLTALVLVLWTAYPILWIIGTEGAGVIGLGTETLLFMVLDVTAKVGFGFILLRSRAIL
Archon2         FNILTALVLVLWTAYPIIWIIGTEGAGVVGLGIETLLFMVLDVTCKVGFGFILLRSRAIL
Archon1         FNILTALVLVLWTAYPIIWIIGTEGAGVVGLGIETLLFMVLDVTAKVGFGFILLRSRAIL
QuasAr6a        FNILTALVLVLWTAYPIIWIIGTEGAGVVGLGIETLLFMVLDVTAKVGFGFILLRSRSIL
QuasAr6b        FNILTALVLVLWTAYPIIWIIGTEGAGVVGLGIETLLFMVLDVTAKVGFGFILLRSIAIL

                241         253
Arch(D95N)      GDTEAPEPSAGAD
QuasAr1         GDTEAPEPSAGAD
QuasAr2         GDTEAPEPSAGAD
QuasAr3         GDTEAPEPSAGAD
paQuasAr3       GDTEAPEPSAGAD
NovArch         GDTEAPEPSAGAD
Archon2         GDTEAPEPSAGAD
Archon1         QDTEAPEPSAGAD
QuasAr6a        QDTEAPEPSAGAD
QuasAr6b        QDTEAPEPSAGAD
```

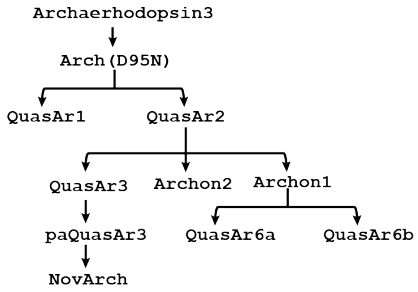

Supplementary Figure 2. Alignment of the amino acid sequences of representative Arch-based GEVIs. Lower right: lineage tree indicating the historical development of different GEVIs. The amino acid substitutions that distinguish each GEVI from its parent are highlighted in red.

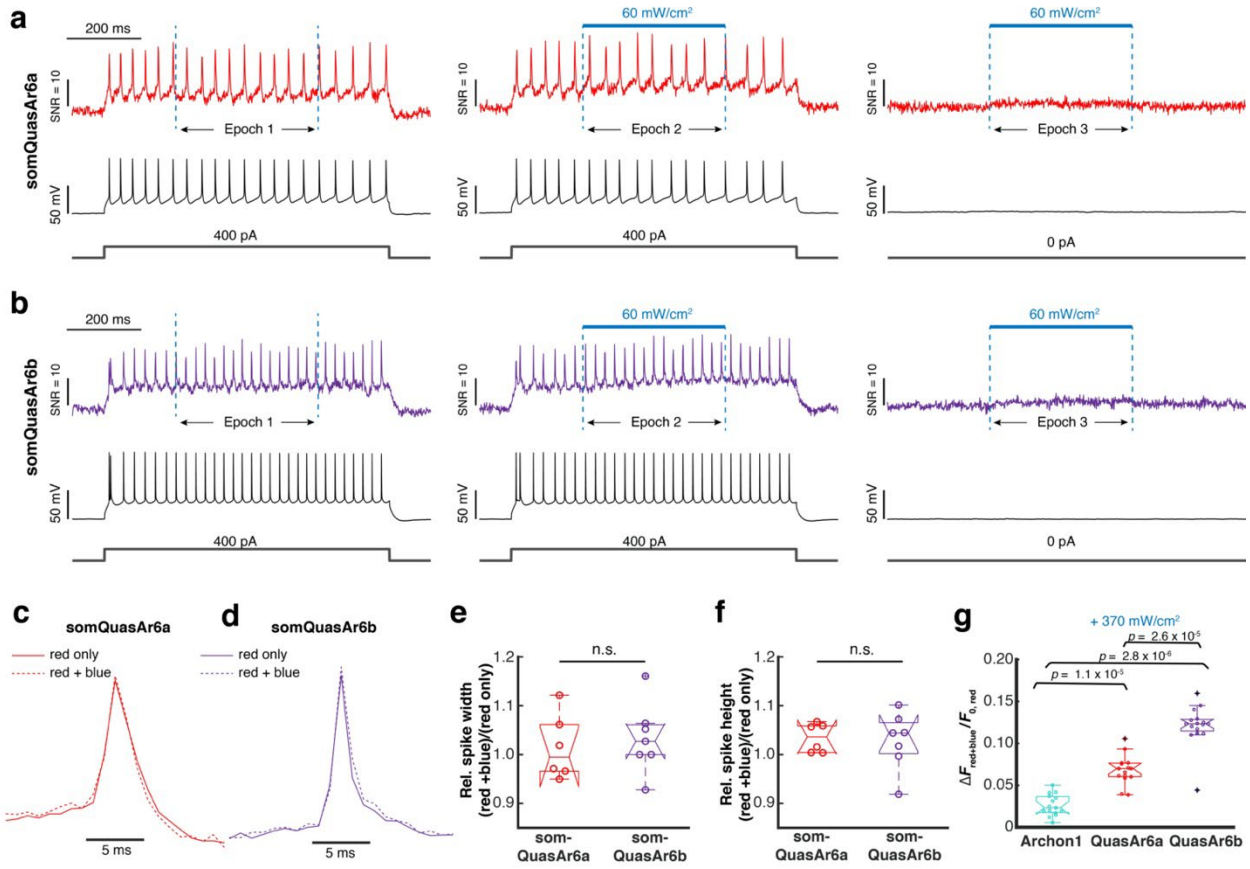

Supplementary Figure 3. Effect of blue light on far-red optical spike waveform. Concurrent fluorescence and voltage recordings were performed for mouse L2/3 cortical neurons expressing somQuasAr6a-EGFP or somQuasAr6b-EGFP in acute slice. **a, b**. Example fluorescence traces with and without the blue light. Spikes were evoked via current injection. The blue light intensity (exc. 488 nm, 60 mW/cm^2) was within the range needed for optogenetic activation. To control for spike waveform adaptation during steady current injection, only the spikes from Epoch 1 (red-only) and Epoch 2 (red + blue) were used to calculate the average fluorescence waveforms. The fluorescence traces in Epoch 3 showed that blue light crosstalk was negligible under these conditions. **c, d**. Spike-triggered average fluorescence waveforms calculated from the traces shown in **a**, **b**. **e**. Relative optical spike widths ((red + blue)/(red-only)) of somQuasAr6a-expressing neurons (mean ± S.D., 1.01 ± 0.07, *n* = 6 cells) and somQuasAr6b-expressing neurons (mean ± S.D., 1.03 ± 0.08, *n* = 7 cells). n.s., not significant (Wilcoxon rank-sum test). **f**. Relative optical spike heights ((red + blue)/(red-only)) of somQuasAr6a-expressing neurons (mean ± S.D., 1.03 ± 0.03; *n* = 6 cells) and somQuasAr6b-expressing neurons (mean ± S.D., 1.03 ± 0.06, *n* = 7 cells). n.s., not significant (Wilcoxon rank-sum test). **g**. Quantification of blue-light induced photoactivation (635 nm, 420 W/cm^2; 488 nm, 0.37 W/cm^2) in HEK cells. The blue-

activation coefficient is defined as the Arch-channel fluorescence signal change under both blue and red excitation ($F_{ex488+ex635}$ - F_{ex488} - F_{ex635}), normalized by the baseline Arch-channel fluorescence ($F_{0,\ ex635}$) [4]. Blue-activation coefficient (mean ± S.D.): 0.02 ± 0.01 for Archon1 (n = 15 cells); 0.07 ± 0.02 for QuasAr6a (n = 15 cells); 0.12 ± 0.02 for QuasAr6b (n = 16 cells), two-sided Wilcoxon rank-sum test. Box plots: central mark indicates median, bottom edge 25th percentile, top edge 75th percentile, whiskers most extreme data points excluding outliers, '+' symbol outliers.

SUPPLEMENTARY METHODS

Molecular cloning

Restriction endonucleases were purchased from New England BioLabs (NEB). Non-mutagenic PCR reactions were performed with Phusion® High-Fidelity DNA Polymerase (NEB, Cat. # M0530L). Synthetic DNA oligonucleotides used for cloning were purchased from Integrated DNA Technologies (IDT). Opsin sequences containing a single point mutation were generated through site-directed mutagenesis (QuikChange Lightning Single or Multi kit, Agilent Technologies, Part # 210518 or 210519). Opsin sequences containing multiple point mutations were synthesized *de novo* as gBlocks (IDT). Error-prone PCR was performed with GeneMorph II Random Mutagenesis Kits (Agilent Technologies, Part # 200552) or home-made PCR cocktail (NEB Taq polymerase, 5 mM $MgCl_2$, 0.2 mM each of dGTP and dATP, and 1.0 mM each of dCTP and dTTP). Small-scale isolation of plasmid DNA was performed in house with GeneJET miniprep kit (Thermo Scientific, Cat.# K0503). Large-scale isolation of plasmid DNA was outsourced to Genewiz. The design of the soma-targeted QuasAr6a and QuasAr6b AAV was similar to that of somArchon1. [5] The design of the cre-on bicistronic Optopatch construct of QuasAr6b and QuasAr6b (pAAV_hSyn-DiO-SomQuasAr6-EGFP-P2A-somCheRiff_HA) was based on Optopatch4 that used Archon1 as the voltage indicator [3].

HEK cell culture

Wild-type or engineered HEK293T cell lines were maintained at 37 °C, 5% CO_2 in Dulbecco's Modified Eagle Medium (DMEM) supplemented with 10% fetal bovine serum, 1% GlutaMax-I, penicillin (100 U/mL), streptomycin (100 mg/mL). For maintaining or expanding the cell culture, we used TC-treated culture dish (Corning). For all the imaging experiments, cells were plated on glass-bottomed dish dishes (Cellvis, Cat.# D35-14-1.5-N). Before optical stimulation and imaging, the medium was replaced with extracellular (XC) buffer containing 125 mM NaCl, 2.5 mM KCl, 3 mM $CaCl_2$, 1 mM $MgCl_2$, 15 mM HEPES, 30 mM glucose (pH 7.3). We found that the XC buffer maintained the cell adhesion and response to optogenetic stimulation for at least 7 - 8 hours.

Lentivirus packaging

All the lentivirus preparations were made in house. HEK293T cells were co-transfected with the second-generation packaging plasmid psPAX2 (Addgene #12260), envelope plasmid VSV-G (Addgene #12259) and transfer plasmids at a ratio of 9:4:14. In this study, we generally used FCMV, sometimes pLenti-CMV, as the transfer vector for HEK cell experiments. We used FSyn for cultured neuron experiments [6]. Both FCMV and FSyn were modified from a previously

described FCK lentivirus vector [7] by replacing the original CaMKII with a CMV or a hSyn promoter, respectively. For lentivirus intended for HEK cell transduction, 2.7 µg total plasmids for a small culture (300k cells in 35-mm dish) gave sufficient yield of lentivirus. For cultured neuron transduction, larger cultures in 15-cm dish or 10-layer HYPER Flasks (CheRiff construct, Corning #10030) were used, and HEK cells were transfected with PEI using established protocols [8]. The harvested vrus was concentrated 10-fold (voltage sensors) or 30-fold (CheRiff) using a cationic polymer (Takara Lenti-X Concentrator).

In-house AAV packaging

AAV2/9 hSyn-DiO-SomQuasAr6a-EGFP and AAV2/9 hSyn-DiO-SomQuasAr6b-EGFP were packaged in house based on a published protocol [9]. Briefly, 50~70% confluent HEK293T cells grown in DMEM supplemented with 5% FBS were triple transfected with pHelper, pAAV ITR-expression, and pAAV Rep-Cap plasmids using acidified PEI (DNA-to-PEI ratio = 1: 3) in 1~2 T175 flasks (~ 2 x 10^7 cells each flask). The AAV-containing medium was harvested on Day 3, and the AAV-containing medium and cells were harvested on Day 5. For the second cell-containing harvest, AAVs were released from the cells with citrate buffer (55 mM citric acid, 55 mM sodium citrate, 800 mM NaCl, 3 mL per flask). The two harvests were then combined and precipitated with PEG/NaCl (5x, 40% PEG 8000 (w/v), 2.5 M NaCl, 4°C overnight). The low-titer virus was then purified with chloroform extraction (viral suspension and chloroform 1:1 (v/v)), aqueous two-phase partitioning (per 1 g of the AAV-containing supernatant, add 5 g of 20% (NH4)2SO4 solution and 1.5 g of 50% PEG 8000 solution, and iodixanol discontinuous gradient centrifugation (15%, 25%, 40%, and 54% iodixanol gradient prepared from OptiPrep (60% (w/v) Iodixanol, Axis-Shield PoC AS). The purified AAV was tittered with qPCR (SYBR Green, primer for forward ITR: 5'-GGAACCCCTAGTGATGGAGTT-3'; primer for reverse ITR sequence 5'-CGGCCTCAGTGAGCGA-3').

Engineering monoclonal spiking HEKs

All the spiking HEK cells were engineered on HEK293T background (ATCC CRL-3216). First, $Na_V1.5$-Puro$^+$ HEK293T cells were generated as previously described [10]. The tet-inducible expression system was designed by the Eric Campeau lab and obtained through Addgene. $K_{ir}2.1$-CFP was cloned into the open reading frame of pLenti-CMVtight-EGFP-Neo vector (Addgene Plasmid #26586). pLenti-CMV-rtTA3-Blast (Addgene Plasmid #26429) was used directly to package lentivirus. $Na_V1.5$-Puro+ HEK293T cells were simultaneously infected with pLenti-CMV-rtTA3-Blast and pLenti-CMVtight-$K_{ir}2.1$-CFP-Neo (TDG004). The cells were first selected with three antibiotics (2 µg/mL puromycin, 5 µg/mL blasticidin, 200 µg/mL Geneticin/G418), then

induced with doxycycline (2 μg/mL) for ~30 hours before FACS purification. The CFP$^+$ cells were seeded into 96-well plates (1 cell per well) and cultured 3 - 4 weeks under the standard conditions for HEK cell culture. The expanded monoclonal cells were screened with current clamp. The clone that showed robust spike upon current injection was termed tet-on spiking HEK cell and used to engineer the CheRiff-CFP$^+$ spiking HEK cells.

CheRiff-CFP was cloned into FCMV lentivirus vector (HT041). After lentiviral infection and monoclonal selection, the CheRiff-CFP$^+$ spiking HEK cells were optically screened. The spikes were evoked with optogenetic stimulation (exc. 490 nm) and visualized using a voltage-sensitive dye (BeRST, exc. 635 nm) [11]. The CheRiff-EGFP$^+$ spiking HEK cells were engineered differently. Nav1.5-Puro/rtTA3-Blast/K_{ir}2.1-CFP-Neo$^+$ polyclonal HEK cells were infected with FCMV-CheRiff-EGFP (HT028) lentivirus. After doxycycline induction, the CFP$^+$/EGFP$^+$ cells were purified by FACS and seeded into 96-well plate for monoclonal selection. The monoclonal cells were validated by patch clamp under optogenetic stimulation.

To enhance genomic stability, the spiking HEK cells can be maintained in antibiotic-containing medium (2 μg/mL puromycin, 5 μg/mL blasticidin, 200 μg/mL Geneticin/G418). However, we found the cell lines reasonably stable even without these antibiotics. To obtain consistent experimental results, we only used low passage-number cells and kept a master plate free of doxycycline.

Tet-on spiking HEK cell and CheRiff-EGFP$^+$ tet-on spiking HEK cell are available from ATCC (CRL-3479; CRL-3480).

Photoselection system

Optical system

The optical system was described in an earlier publication [2] with a few modifications for the present use. The microscope was in an inverted configuration to facilitate imaging of cultured cells in glass-bottomed dishes. The system was equipped with several light sources delivered to the sample through free-space optics: 1) a 635-nm laser (DILAS 8 Watts, MB-638.3-8C-T25-SS4.3) sent to the sample plane from below through a near-total internal reflection (near-TIR) configuration for imaging archaerhodopsin-derived GEVIs; 2) LEDs mounted from the above for optogenetic stimulation and imaging fluorescent proteins; 3) a 405-nm laser (MDL-W-405-1W) projected to a micromirror-array device (Digital light innovations, Discovery D4100 with DLP9500 chip and ALP 4.1 High-Speed control software) for photoselection. The patterned light was collected with a tube lens (Olympus MVX, 0.63×) and directed to the sample by a small 45° mirror

(4 mm mirror, Tower Optical, MPCH-4.0) inserted into the infinity space. The emission fluorescence was collected with a low-magnification (2×) and high-numerical aperture (NA 0.5) objective lens and filtered with wavelength-specific filters inserted into the infinity space. The emission filter wheel was tilted by a small angle to avoid reflection of light between the sample dishes and filters. After filtering, the emission light was reimaged through a tube lens (Zeiss, Milvus 2/135) and recorded with a scientific CMOS camera (Hamamatsu, ORCA-Flash 4.0). The system was controlled by custom-made LabView codes.

Calibration of patterned illumination

We used a digital micromirror array device (DMD) to illuminate target cells, and calibrated it for precise optical targeting of single cells over a large field of view (2.3 mm × 2.3 mm, Extended Data Fig. 1a). The DMD comprised a 1920 ×1080 array, which did not provide 1:1 correspondence with the camera chip (1024×1024 at binning = 2). Moreover, small alignment errors and optical aberrations could manifest as substantial projection errors. To register the DMD array with the camera pixel coordinates, we projected an equally spaced (d = 50 pixels), 11×11 array of dots (20 pixels interval) onto a fluorescent exposure target (exc. 405-nm; CFP emission filter). The dimension of this test pattern (500 × 500 pixels) was intended to cover the field of view (FOV) for GEVI screening. The center of each dot in the camera image was determined by 2D Gaussian fitting of the point-spread function. The transformation relationship between actual projection and the expected projection was determined using Matlab Image Processing Toolbox (imwarp, piecewise linear transformation).

Comparison of different phototaggable FPs

We evaluated three candidate phototaggable FPs for Photopick (Extended Data Fig. 1b): mEos4a, a green-to-red photoconvertible FP [12]; PA-mCherry, a red photoactivable FP [13], and PA-GFP, a green photoactivable FP [14]. Phototransformation was most efficient for mEos4a (fluence at 405 nm for 50% phototagging: 5.4 ± 0.3 J/cm^2 for mEos4a; 18 ± 4 J/cm^2 for PA-mCherry; 140 J/cm^2 for PA-GFP, Extended Data Fig. 1c), and mEOS4a had a spectral window compatible with Arch-derived GEVIs, so we selected this protein as our photo-tag.

Calibration of selection efficiency and fidelity

We evaluated the efficiency and fidelity of Photopick. We plated a mixture of mEos4a$^+$ cells (green-to-red), PA-mCherry$^+$ cells (dark-to-red) and blank HEK cells (approximate final ratio 1:2:50) in a monolayer on the glass-bottomed dish (Fig. 1b). The ratios of cell numbers were selected to approximate the conditions in subsequent experiments. We sought to photoconvert

the mEos4a$^+$ cells while not converting the PA-mCherry$^+$ cells. We imaged the green (mEos4a) fluorescence and then applied patterned illumination of violet light targeted to the mEos4a$^+$ pixels (Fig. 1c). FACS analysis showed that the fidelity (phototagged mEos4a$^+$ cells/(phototagged mEos4$^+$ cells + phototagged PA-mCherry$^+$ cells)) was approximately 96% and efficiency (phototagged mEos4a$^+$ cells/all mEos4$^+$ cells) was approximately 85% (Fig. 1d; see also Extended Data Fig. 1d.). We concluded that the Photopick system had sufficient precision for phenotype-activated photoselection at cellular resolution.

Video-based pooled screening for engineering improved GEVIs

Generation of the library cells

Archon1 sequence was a gift from Ed Boyden at MIT. Previously, we found that a fluorescent protein tag could significantly enhance the membrane localization of Archaerhodopsin-derived GEVIs in mammalian cells. In particular, a combination of Citrine and multiple repeats of trafficking sequence (TS-Citrine-TS×3-ER2) improved the voltage imaging SNRs in cultured neuron [15]. Initially, we attempted to substitute Citrine with mEos4a. However, this substitution resulted in poorly trafficked protein. Therefore, we switched to a bicistronic construct, in which GEVI and mEos4a were linked with a self-cleaving P2A peptide [16]. Because Citrine and mEos4a share the same spectral window, a single point mutation (Y67G) was introduced into Citrine to create a non-fluorescent protein tag, “dark Citrine” [6].

Random mutations were introduced into Archon1 using error-prone PCR. Then the mutated opsin sequences were fused to the rest of the coding sequence (TS-dark Citrine-TS×3-ER2-P2A-mEos4a) using fusion PCR and purified with agarose gel electrophoresis. The purified DNA fragment was inserted into the FCMV lentivirus vector using Gibson assembly, transformed into DH5α *E*. coli competent cells (NEB), and plated on ampicillin-containing (Amp+) agar plates. We used Sanger sequencing to analyze the mutation rate of a small number (<10) of clones. Each mutant included 0, 1, or 2 amino acid substitutions (average number ~ 1). The colonies were scraped from the agar plates, transferred into Amp+ LB medium, allowed to grow at room temperature for approximately 1 hour before miniprep. The plasmid library was then used for lentivirus preparation. CheRiff-CFP$^+$ spiking HEK cells were infected with the lentivirus library at a low titer (MOI ~ 0.01). The mEos4a$^+$ cells were purified with FACS and cultured with the standard HEK cell culture protocol. In this study, we generated two random mutagenesis libraries based on Archon1. Each was independently evolved and analyzed on the Photopick platform.

Image segmentation and ROI selection

The 500 × 500-pixel FOV (2.3 mm × 2.3 mm in the sample plane) was segmented based on the mEOS-channel (excited with 490-nm LED) image using custom Matlab code. Briefly, the mEos4a-channel image was corrected for baseline and segmented with Watershed algorithm. Only ROIs larger than 5 pixels were accepted as "cells", and smaller ROIs were rejected. We observed that after 2 days of culture, the library cells often showed small clusters, primarily due to cell division. We reasoned that since the neighboring cells descended from the same parent cells, it was acceptable to treat small clusters as a single genotype.

In pilot experiment in Extended Data Fig. 2c, the library cells were replaced with the monoclonal CheRiff$^+$/Archon1-Citrine$^+$ spiking HEK cells. We found that even a monoclonal population showed substantial variation in F_0 and ΔF, possibly due to variations in protein expression or trafficking. Thus, we concluded that 1) there were non-genetic factors underlying the broad distribution of expression level, and 2) setting a stringent threshold for F_0 was unlikely to be meaningful. In our experiments, we set a 50th percentile threshold for $F_{0,Arch}$, and 75th percentile cut-off for $\Delta F_{Arch}/\sqrt{F_{0,Arch}}$. These top 12.5% of ROIs were selectively illuminated with violet light to create a binary marker.

Fluorescence-activated cell sorting (FACS)

FACS was performed on a BD FACS Aria Cell Sorters. The gating strategy is shown in Supplementary Figure 1. The data was analyzed with FCSExpress 7 Research Edition.

Illumina sequencing

16k - 20k library cells were collected into PCR tubes and boiled (98 °C, 5 min) to release their genomes as the PCR template. The opsin sequences were amplified from the genome (forward primer: GACCTCCTCGGAGATGGTAGA; reverse primer: AGCTGAAGGTTCAGGTGCTTC). The primer pair used here gave a 720-bp amplicon that covered the 31-750 nt of Archon1 CDS, which effectively provided single nucleotide polymorphism (SNP) information for 52-729 nt. We also attempted primers designed to cover the entire 759 nt of Archon1 CDS. However, we found that full-coverage primers did not result in robust PCR amplification. We reasoned that as the N-terminus and C-terminus are distant from the retinal chromophore and unlikely to modulate the voltage-sensitive fluorescence, the omission of the terminal sequence information should not severely negatively impact our screening efforts. In the earlier efforts to optimize archaerhodopsin-derived GEVIs, no beneficial mutations have been identified in the missing regions [7, 17].

The 720-bp amplicon were then segmented into 3 smaller amplicons with high-fidelity PCR:

Fwd1: TCGTCGGCAGCGTCAGATGTGTATAAGAGACAG-GACCTCCTCGGAGATGGTAG,
Rev1: GTCTCGTGGGCTCGGAGATGTGTATAAGAGACAG-TGTAGTGAACAGCCACTGTG;
Fwd2: TCGTCGGCAGCGTCAGATGTGTATAAGAGACAG-CTGAACATCTACTACGCAAG,
Rev2: GTCTCGTGGGCTCGGAGATGTGTATAAGAGACAG-CTGGGCCTCTCTCCTTAGCG;
Fwd3: TCGTCGGCAGCGTCAGATGTGTATAAGAGACAG-GTCCTGGCCACTTCTCTGCG;
Rev3: GTCTCGTGGGCTCGGAGATGTGTATAAGAGACAG-AGCTGAAGGTTCAGGTGC).

We chose 2 x 150 bp paired-end MiSeq (Harvard Medical School Biopolymer Facility) to analyze the SNPs. We obtained a sequencing depth of 2 - 5 $\times 10^5$ reads per nt (filtered for Illumina Q score > 30). VCF data were generated from the FASTAQ data with a custom pipeline that included Trimomatic [18], NGmerge [19], BWA [20], samtools [21], and Pilon [22]. The VCF data were subsequently analyzed with custom Matlab code.

Simulation of the selection threshold

To determine the probability that a mutation could be enriched in the selection by chance alone, we performed a Matlab simulation of the selection process, assuming random selection for a mutant with starting frequencies of 0.002%, 0.004%, 0.006%, 0.008%, 0.01%, 0.02%, 0.03%, 0.04%, 0.05%, 0.06%,0.07, 0.08%. The upper limit of 0.08% was chosen based on the sequencing result of the starting library. The initial number of library cells was set to be 50,000. We randomly allowed 5,000 – 12,000 “cells” to pass the selection. These numbers were determined by the actual numbers of cells collected from FACS (5,000 ~12000 cells after each round). We then expanded the population 100-fold and repeated the sampling and expansion process two more times. The 95% confidence threshold on the prevalence of a mutational frequency arising by chance was determined from 2,000 iterations of the simulation.

High-throughput imaging of hippocampal neurons

Functional Optopatch imaging was performed after 14 days in culture on the Firefly microscope [8]. The Firefly microscope was fully automated and ran with no human intervention. Imaging was performed at room temperature and no extra heating was provided so as to reduce evaporation-related artifacts. The whole plate was scanned automatically with motorized stages so that the three FOVs within each well were evenly spaced. Focus was also automatically adjusted for each FOV. Optogenetic stimulus to CheRiff was generated by a blue LED, filtered (Semrock No. FF01-470/28), and delivered to a large area with intensity ranging from 2 to 88 mW/cm^2. 638 nm red laser light was applied through a prism in near-TIR, so the beam transmitted into the imaging media and propagated nearly parallel to the surface. The illumination intensity was 200 W/cm^2

(neglecting beam intensification by refraction at the imaging buffer/COC substrate). Fluorescence was imaged at 2.7× magnification onto an sCMOS camera (Hamamatsu ORCA-Flash 4.0 V2) through a near-infrared emission filter (Semrock #FF02-736/128) and data was collected at a 1 kHz frame rate. The FOV for 1 kHz recording was 0.39 mm x 3.9 mm (800 x 80 pixels in 2 x 2 binning).

Confocal imaging of QuasAr6a and QuaAr6b expressed in cultured rat hippocampal neuron

To sparsely expression QuasAr6b-Citrine or QuasAr6b-Citrine, rat hippocampal neuron cultures were transfected with Fsyn plasmids (HT111, HT114) encoding the constructs via Ca-Phos. Before imaging, the medium was replaced with transparent XC buffer. The confocal images were acquired on LSM880 Airyscan with an air 20× objective. Citrine fluorescence was excited with 488-nm laser.

Characterization of QuasAr6a and QuasAr6b in brain slice

Voltage imaging in acute slice

The imaging set-up was originally described in [15] with a few modifications. For the red laser path, the 639 nm laser source (CNI Lasers, MLL-FN-639, l = 639 nm, 1 W single transverse mode) was attenuated with a half-wave plate and polarizing beam splitter and directed to the center of the FOV. The size of the beam was adjusted to be slightly larger than the size of a typical neuron soma. The blue laser path included a laser source, the blue laser (Coherent, OBIs, l = 488 nm, 60 mW), an acousto-optic tunable filter (AOTF; Gooch and Housego TF525-250-6-3-GH18A) for modulating the laser intensity, and a digital micromirror device with a resolution of 1024×768 pixels (Vialux, V-7000 UV, 9515)). The waveforms of optogenetic stimulation sequence and voltage imaging sequencing were controlled via a National Instruments DAQ (NI PCIe-6363). The movies were acquired at 996.3 Hz (1 kHz) with a sCMOS camera (Hamamatsu ORCA-Flash 4.0). A Cy5 emission filter was used in the Arch-channel. The camera's internal 100 kHz clock was used as the master clock to synchronize all the DAQ inputs and outputs. The system was controlled with a custom software developed in Matlab. This Matlab-based control software includes modules interfaced with 1) the sCMOS camera, 2) DAQ; 3) DMD; 4) amplifier. Imaging was performed with a 25× water immersion objective (Olympus XLPLN25XSVMP2) with a 4-mm working distance and a numerical aperture of 1.0.

***In vivo* all-optical electrophysiology**

Cranial window surgery for imaging visual cortical L1

For experiments in Fig. 4a-e, the window was comprised of two 3-mm round #1 cover glasses and one 5-mm round #1 cover glass (Harvard apparatus) cured together with UV curable adhesive (Norland Products, NOA 81). For experiments in Fig. 4f-i, one 3-mm round #1 cover glass was glued to a custom-made stainless-steel adapter. The adapter has an outer diameter of 5 mm and inner diameter of 2.7 mm.

The cranial window surgery for imaging L1 was performed as described previously [23]. In brief, 10 - 16 weeks-old NDNF-Cre$^{+/-}$ mice (male or female) were induced with > 2% isoflurane and maintained in deep anesthesia with 1% isoflurane throughout the surgery. A heating pad (WPI, ATC2000) was placed beneath the mice to main the body temperature at 36 - 37 °C. Ophthalmic eye ointment was applied on the eyes to keep them moist. An approx. 3-mm craniotomy was created on the left visual cortof the exposed skull (AP: 2.5 - 2.6-mm lateral, 0.8-mm anterior of lambda) with a dental drill. The Optopatch virus was diluted to a final titer of 1×10^{13} GC/mL for experiments in cortical NDNF neurons, or to a final titer of 0.5 - 1.0×10^{13} GC/mL for experiments in hippocampal PV neurons. The diluted virus was injected at 7 - 8 sites across the craniotomy (80 and 160 μm beneath dura; 40 - 60 nL each depth; 30 - 60 nL/min). After virus injection, the craniotomy was covered with the glass window. The edge of the window was glued to the skull with cyanoacrylate adhesive (3M Vetbond). Next, a titanium headplate (designed based on [23]) was attached to the exposed skull with dental cement (C&B metabond, Parkell, No. 242-3200). Special care was taken to ensure that the dental cement filled the space between the rim of the window and the skull and covered all the exposed area of the skull. Animal typically recover from anesthesia within 20 min. Then they were returned to their home cage and administrated with Carprofen (5 mg/kg) and Buprenorphine (0.1 mg/kg) on post-surgery Day 0, 1, 2.

Window surgery for imaging hippocampus CA1

The window surgery for imaging hippocampus CA1 was performed based on previous reports [15, 24]. In brief, the cannula window was comprised of a 1.5-mm segment of a 3-mm outer diameter thin-walled stainless steel tube (MicroGroup) and 3 mm #1 round cover glass (Harvard Apparatus) glued to one end of the tube using UV-curable adhesive (Norland Products, NOA 81). 8 - 12 weeks old PV-Cre$^{+/-}$ mice (male or female) were used for imaging. A 3-mm craniotomy was created on the left hemisphere (1.8 mm lateral, 2.0 mm caudal of bregma) with a biopsy punch (Miltex). Optopatch virus was diluted to 2.5 ~ 5 $\times10^{12}$ GC/mL and injected into three sites near the center of the craniotomy (1.0 mm to 1.4 mm beneath dura with 0.1 mm increment; 40 nL each depth; 60 nL/min). After virus injection, the cortwas carefully aspirated, and the center region of the external capsule was removed to expose the hippocampus CA1. The cannula was then

lowered onto the CA1 surface until the window touched the tissue. The remaining outer surface of the cannula was sealed to the exposed skull with dental cement (C&B Metabond). Finally, a titanium head plate was fixed onto the exposed skull. The post-surgery care was identical to that of the cranial window surgery for L1 imaging.

Optical systems for in vivo all-optical electrophysiology

The imaging set-up was originally described in [3] with a few modifications. For the red laser path, the 639 nm laser source (CNI Lasers, MRL-FN-639, l = 639 nm, 700 mW single transverse mode, later replaced by a Coherent OBIS, l = 637 nm 140mW Laser) was attenuated with a half-wave plate and polarizing beam splitter, expanded to a collimated beam of ~10 mm diameter, then projected onto the surface of a reflection-mode liquid crystal spatial light modulator (SLM, Meadowlark 1920SLM VIS) with a resolution of 1920×1152 pixels. For the blue laser path, the blue laser (Coherent OBIS, l = 488 nm, 100 mW) was modulated in intensity via an acousto-optic tunable filter (AOTF; Gooch and Housego TF525-250-6-3-GH18A) and collimated to a beam of ~17 mm in diameter before being directed onto the reflective surface of a digital micromirror device with a resolution of 1024×768 pixels (DMD, Vialux, V-7001 VIS). The waveforms of optogenetic stimulation sequence and voltage imaging sequencing were controlled via a National Instruments DAQ (NI PCIe-6363). The movies were acquired at 1,000 - 4,000 Hz with a sCMOS camera (Hamamatsu ORCA-Flash 4.0). A Cy5 emission filter was used in the Arch-channel. The camera's internal 100 kHz clock was used as the master clock to synchronize all the DAQ inputs and outputs. The system was controlled with a custom software developed in Matlab. This Matlab-based control software includes modules interfaced with 1) the sCMOS camera, 2) DAQ; 3) DMD, and 4) SLM. The software also includes routines for registration of SLM, DMD and camera.

Data analysis

Data were analyzed and plotted with homemade code written in MATLAB.

Extracting the voltage-sensitive fluorescence from in vitro and ex vivo imaging

We used a previously described maximum-likelihood pixel-weighting algorithm [25] to define the mask for voltage-sensitive fluorescence. Whole-cell masks were initially manually defined. Then the raw whole-cell fluorescence from the cell masks was used to guide the algorithm to automatically find the pixels carrying the most information. Based on the weighting information, new masks excluding the least informative pixels were created. Then the pixel-selective masks were applied to the original movie to calculate fluorescence from the unweighted mean of pixel

values within the selected ROIs. For GEVIs like QuasAr6 with good trafficking, we often found that the pixel-selective masks correspond to the cell membranes. For calculations of Δ*F*/*F* in HEK293T and neuron culture, fluorescence from a cell-free region was deemed as the baseline signal of the cell and extracted from each trace.

In our experiences, the value of Δ*F*/*F* is highly variable in tissue slice and live brain, where multiple factors such as the depth of the cell, light scattering, the intensity of autofluorescence, and patterned illumination, may affect baseline determination. Thus, for voltage imaging in slice and in the brain, we mostly used either signal-to-noise ratio (SNR) or relative signal normalized to the full spike height to represent the voltage-sensitive fluorescence change. In Fig. 3m, p, no baseline correction was applied, and the Δ*F*/*F* in these plots are not accurate measurements of the *V-F* relationship.

Extracting the voltage-sensitive fluorescence from in vivo imaging

Movies were corrected for motion using the NoRMCorre algorithm [1]. Next, photobleaching was corrected using mono-exponential fit. Next, masks for each cell were manually defined, and the movie was divided into sub-movies based on the contour of the cell masks. To accurately extract the subthreshold dynamics, we performed activity-based image segmentation separately in each sub-movie. Our assumption was that while subthreshold voltages could be correlated between a cell and out-of-focus background cells, spike dynamics are unlikely to be correlated with background. We also assumed that spiking dynamics and the true subthreshold dynamics would share the same spatial footprint. The sub-movies were filtered in time with a 50 Hz high-pass filter, and then segmented semi-automatically using principal components analysis followed by time-domain independent components analysis (PCA/ICA). The spatial masks from PCA/ICA were then applied to the original movies without high-pass filtering to extract fluorescence traces that included both spike and subthreshold dynamics.

We found that the quality of the spatial masks generated by PCA/ICA depended on the SNR of the raw movie, as well as the number of spikes in the raw movie. In general, the stronger SNR in the raw movie, and the more spikes in the segmented epoch, the more likely we obtain high-quality spatial masks. For some recordings where the SNR was good enough for accurate detection of spikes (SNR > 4), but did not give high-quality PCA/ICA masks, these recordings were only used to analyze spike dynamics, but not for extracting subthreshold dynamics. Because PCA/ICA is biased towards high-SNR recordings, in Fig. 4 and Extended Data Fig. 8 where the *in vivo* SNR were compared, we used the manually-created mask to extract the fluorescence trace.

Spike detection and trace normalization

Fluorescence traces were first high-pass filtered (medfilt1, window = 25 ms unless otherwise indicated). We used two complementary methods for spike detection. First, a simple threshold-and-maximum procedure was applied on the high-pass filtered fluorescence trace. The initial threshold was set at 3 times of the noise level and adjusted if necessary. Second, we performed wavelet transformation on the high-passed filtered traces to extract the signals based on the time-domain (Matlab Wavelet toolbox). Specifically, we performed the maximal overlap discrete wavelet transform (modwt, wavelet type = ''sym4', computed to level 8). We next projected the higher-frequency wavelets (level 2, 3, 4) into a time trace (imodwt,'sym4'), then applied a threshold-and-maximum procedure to identify the peaks in the projected traces Compared to Fourier transformation, wavelet decomposition allows the expansion of signals in terms of finite time functions, which gives higher selectivity to impulse-like events such as action potentials. A fluorescence impulse was accepted as spikes only if it stood out in both spike detection methods. We found the wavelet transformation particularly helpful to spike detection in PV neurons because PV neurons' characteristically narrow spikes were much faster than most sources of noises. All fluorescence traces were then normalized to spike height for spike triggered average.

Calculation of spike SNRs and waveforms

We define SNR as the ratio of the height of spike (fluorescence signal above the subthreshold) to the high-frequency noise. The high-frequency noise was defined as the standard deviation of the non-spiking epoch of the high-pass filtered (medfilt1, window = 25 ms) fluorescence trace. Because the intensity of photocurrent modulated the height and waveform of the spike, we only used the ramp epoch to calculate spike height and waveforms. For PV spikes, we used all the spikes from the upward- and downward- ramps. For the NDNF spikes, because the ramp of the blue light was steeper, we found the spike height and waveform varied quickly. Thus, we only used the first three spikes from the ramp for the calculation.

Estimation of spike rate with Bayesian Adaptive Kernel Smoother

In the double Optopatch experiments on the NDNF+ cells, the duration of the stimulation was short so the total number of the spikes were limited. As a result, the calculation of the spike rate was sensitive to the choice of integration window. Thus, we used a Bayesian Adaptive Kernel Smoother (BAKS) [26] to convert discrete spike raster into continuously varying spike rate. The Matlab function was downloaded from https://github.com/nurahmadi/BAKS. The shape parameter (a) and the scale parameter (b) were both set to 40. As a quality control, we compared the average

of the BAKS-derived spike rate against the average spike rate directly calculated from the spike raster. We found the two methods in good agreement.

Test for bias for or against reciprocal connections

Consider measurements on N cell pairs (N = 22 in our data), which yield n_2 reciprocally connected pairs (n_2 = 8), n_1 unidirectionally connected pairs (n_1 = 10), and n_0 unconnected pairs (n_0 = 4). We have $n_0 + n_1 + n_2 = N$ and the total number of directed connections is $M = 2n_2 + n_1$. In our dataset, M = 26.

The number of ways of selecting n_1 single and n_2 double connections is:

$$\Gamma(n_1, n_2) = \binom{N}{n_2}\binom{N-n_2}{n_1} 2^{n_1} ,$$

where $\binom{X}{Y} = \frac{X!}{Y!(X-Y)!}$.

This expression simplifies to:

$$\Gamma(n_1, n_2) = \frac{N!}{n_2! n_1! n_0!} 2^{n_1}.$$

The total number of ways of arranging the M connections among the N cell pairs is

$$\Gamma_{tot} = \binom{2N}{M}.$$

Under the null hypothesis that connections are distributed independently, then the probability of observing n_2 reciprocal and n_1 unidirectional connections, given M total connections, is:

$$P_M(n_1, n_2) = \frac{\Gamma(n_1, n_2)}{\Gamma_{tot}} .$$

The probability distribution $P_{26}(n_1, n_2)$ is maximal at n_1 = 10 and n_2 = 8, which are precisely the numbers we measured.

Estimate of optical crosstalk between PV pairs

We reasoned that the upper limit of optical crosstalk between cell pairs could be estimated using the fluorescence signal extracted from an intervening mask midway between the two cells. The intervening mask was created as follows. First, the area and centroid of the cell masks was determined with Matlab function regionprops. Second, a circular mask was created, with its center coordinates at the mid-point between the centroids of the two cell masks, and its area set to be the sum of the areas of both cell masks. However, when the cells were too close, the intervening mask may overlap with the cell mask. Thus, the pixels located within the circular mask radius from the cell mask centroid were removed from the middle mask. The resulting masks generally had comparable, or larger size than the cell masks. The fluorescence signal was extracted by applying the intervening mask to the motion-corrected movie, corrected for any photobleaching and high-pass filtered, and normalized with the voltage fluorescence traces. The optical crosstalk was

calculated as the average fluorescence waveform triggered by the same set of spikes used in calculating cross-triggered average.

Quantifying the gap junction-induced spikelet

The spike-triggered voltage waveform (STVW) was calculated using the PCA/ICA extracted fluorescence trace. For the cross spike-triggered voltage waveform (STVW), only events where only one cell spiked (spike peaks in the two cells separated by > 10 ms) were included in the analysis to avoid spurious contributions to a short-time peak from near-coincident spikes. The same set of spikes were used to calculate the self-STVW. The cross-STVW were then normalized with the height of the post-synaptic self-STVW. In Fig. 6c, to preserve the low subthreshold coupling, the fluorescence trace was high-passed filtered with a window of 25 ms. In the double Optopatch experiment in PV cells where the aim was to analyze the fast optogenetically evoked coupling, the fluorescence traces were high-pass filtered with a smaller window of 8 ms. The self- and cross-STVW were calculated over the window from -100 ms to 100 ms (401 data points). The height of the spikelet was determined from the normalized signal at $t = 0$. The p-value was calculated as follows. First, an empirical null distribution was computed using the STA measurements at times $t \neq 0$ ($n = 400$ time-points). This distribution reported fluctuations due to noise. Next, a p-value for the STA measurement at time $t = 0$ was computed as $p = r / n$, where r is the rank of the STA measurement at time $t = 0$ (higher values correspond to lower ranks), and n is the number of STA measurements. This p-value corresponds to the null hypothesis that the STA measurements at $t \neq 0$ are greater than or equal to the STA measurements at $t = 0$. Spikelets are defined as those events with $p < 0.05$ and amplitudes > 2% of the action potential amplitude.

REFERENCES

1. Pnevmatikakis, E.A. & Giovannucci, A. NoRMCorre: An online algorithm for piecewise rigid motion correction of calcium imaging data. *J Neurosci. Methods* **291**, 83-94 (2017).
2. Werley, C.A., Chien, M.P. & Cohen, A.E. Ultrawidefield microscope for high-speed fluorescence imaging and targeted optogenetic stimulation. *Biomed. Opt. Express* **8**, 5794-5813 (2017).
3. Fan, L.Z. et al. All-Optical Electrophysiology Reveals the Role of Lateral Inhibition in Sensory Processing in Cortical Layer 1. *Cell* **180**, 521-535 e518 (2020).
4. Chien, M.P. et al. Photoactivated voltage imaging in tissue with an archaerhodopsin-derived reporter. *Sci. Adv.* **7**, eabe3216 (2021).
5. Piatkevich, K.D. et al. Population imaging of neural activity in awake behaving mice. *Nature* **574**, 413-417 (2019).
6. Fan, L.Z. et al. All-optical synaptic electrophysiology probes mechanism of ketamine-induced disinhibition. *Nat. Methods* **15**, 823-831 (2018).

7. Hochbaum, D.R. et al. All-optical electrophysiology in mammalian neurons using engineered microbial rhodopsins. *Nat. Methods* **11**, 825-833 (2014).
8. Nguyen, C. et al. Simultaneous voltage and calcium imaging and optogenetic stimulation with high sensitivity and a wide field of view. *Biomed. Opt. Express* **10**, 789-806 (2019).
9. Kimura, T. et al. Production of adeno-associated virus vectors for in vitro and in vivo applications. *Sci. Rep.* **9**, 13601 (2019).
10. Zhang, H., Reichert, E. & Cohen, A.E. Optical electrophysiology for probing function and pharmacology of voltage-gated ion channels. *eLife* **5**, e15202 (2016).
11. Huang, Y.L., Walker, A.S. & Miller, E.W. A Photostable Silicon Rhodamine Platform for Optical Voltage Sensing. *J. Am. Chem. Soc.* **137**, 10767-10776 (2015).
12. Paez-Segala, M.G. et al. Fixation-resistant photoactivatable fluorescent proteins for CLEM. *Nat. Methods* **12**, 215-218 (2015).
13. Subach, F.V. et al. Photoactivatable mCherry for high-resolution two-color fluorescence microscopy. *Nat. Methods* **6**, 153-159 (2009).
14. Patterson, G.H. & Lippincott-Schwartz, J. A photoactivatable GFP for selective photolabeling of proteins and cells. *Science* **297**, 1873-1877 (2002).
15. Adam, Y. et al. Voltage imaging and optogenetics reveal behaviour-dependent changes in hippocampal dynamics. *Nature* **569**, 413-417 (2019).
16. Kim, J.H. et al. High cleavage efficiency of a 2A peptide derived from porcine teschovirus-1 in human cell lines, zebrafish and mice. *PLoS One* **6**, e18556 (2011).
17. Piatkevich, K.D. et al. A robotic multidimensional directed evolution approach applied to fluorescent voltage reporters. *Nat. Chem. Biol.* **14**, 352-360 (2018).
18. Bolger, A.M., Lohse, M. & Usadel, B. Trimmomatic: a flexible trimmer for Illumina sequence data. *Bioinformatics* **30**, 2114-2120 (2014).
19. Gaspar, J.M. NGmerge: merging paired-end reads via novel empirically-derived models of sequencing errors. *BMC Bioinformatics* **19**, 536 (2018).
20. Li, H. & Durbin, R. Fast and accurate short read alignment with Burrows-Wheeler transform. *Bioinformatics* **25**, 1754-1760 (2009).
21. Li, H. et al. The Sequence Alignment/Map format and SAMtools. *Bioinformatics* **25**, 2078-2079 (2009).
22. Walker, B.J. et al. Pilon: an integrated tool for comprehensive microbial variant detection and genome assembly improvement. *PLoS One* **9**, e112963 (2014).
23. Goldey, G.J. et al. Removable cranial windows for long-term imaging in awake mice. *Nat. Protoc.* **9**, 2515-2538 (2014).
24. Dombeck, D.A., Harvey, C.D., Tian, L., Looger, L.L. & Tank, D.W. Functional imaging of hippocampal place cells at cellular resolution during virtual navigation. *Nat. Neurosci.* **13**, 1433-1440 (2010).
25. Kralj, J.M., Douglass, A.D., Hochbaum, D.R., Maclaurin, D. & Cohen, A.E. Optical recording of action potentials in mammalian neurons using a microbial rhodopsin. *Nat. Methods* **9**, 90-U130 (2012).
26. Ahmadi, N., Constandinou, T.G. & Bouganis, C.S. Estimation of neuronal firing rate using Bayesian Adaptive Kernel Smoother (BAKS). *Plos One* **13**, e0206794 (2018).

nature portfolio

Corresponding author(s): Adam E. Cohen

Last updated by author(s): Nov 7, 2022

Reporting Summary

Nature Portfolio wishes to improve the reproducibility of the work that we publish. This form provides structure for consistency and transparency in reporting. For further information on Nature Portfolio policies, see our Editorial Policies and the Editorial Policy Checklist.

Statistics

For all statistical analyses, confirm that the following items are present in the figure legend, table legend, main text, or Methods section.

n/a	Confirmed
☐	☒ The exact sample size (*n*) for each experimental group/condition, given as a discrete number and unit of measurement
☐	☒ A statement on whether measurements were taken from distinct samples or whether the same sample was measured repeatedly
☐	☒ The statistical test(s) used AND whether they are one- or two-sided *Only common tests should be described solely by name; describe more complex techniques in the Methods section.*
☐	☒ A description of all covariates tested
☒	☐ A description of any assumptions or corrections, such as tests of normality and adjustment for multiple comparisons
☐	☒ A full description of the statistical parameters including central tendency (e.g. means) or other basic estimates (e.g. regression coefficient) AND variation (e.g. standard deviation) or associated estimates of uncertainty (e.g. confidence intervals)
☐	☒ For null hypothesis testing, the test statistic (e.g. *F*, *t*, *r*) with confidence intervals, effect sizes, degrees of freedom and *P* value noted *Give P values as exact values whenever suitable.*
☒	☐ For Bayesian analysis, information on the choice of priors and Markov chain Monte Carlo settings
☒	☐ For hierarchical and complex designs, identification of the appropriate level for tests and full reporting of outcomes
☒	☐ Estimates of effect sizes (e.g. Cohen's *d*, Pearson's *r*), indicating how they were calculated

Our web collection on statistics for biologists contains articles on many of the points above.

Software and code

Policy information about availability of computer code

Data collection	All the data needed to understand and assess the study are included in the figures (main text, extended data, and supplementary).We have the raw data well organized on our lab server and prefer to direct interested parties to make a request so we can provide contextual information and possibly also share additional datasets that did not make it into the paper.
Data analysis	The data were analyzed with Matlab (2016-2021). FACS data were analyzed with FCSExpress 7 Research Edition.

For manuscripts utilizing custom algorithms or software that are central to the research but not yet described in published literature, software must be made available to editors and reviewers. We strongly encourage code deposition in a community repository (e.g. GitHub). See the Nature Portfolio guidelines for submitting code & software for further information.

Data

Policy information about availability of data

All manuscripts must include a data availability statement. This statement should provide the following information, where applicable:

- Accession codes, unique identifiers, or web links for publicly available datasets
- A description of any restrictions on data availability
- For clinical datasets or third party data, please ensure that the statement adheres to our policy

Data and materials used in the analysis are available upon reasonable request to Adam E. Cohen. The crystal structure PDB: 6GUY is from the Protein Data Bank.

Human research participants

Policy information about studies involving human research participants and Sex and Gender in Research.

Reporting on sex and gender	NA
Population characteristics	NA
Recruitment	NA
Ethics oversight	NA

Note that full information on the approval of the study protocol must also be provided in the manuscript.

Field-specific reporting

Please select the one below that is the best fit for your research. If you are not sure, read the appropriate sections before making your selection.

☒ Life sciences ☐ Behavioural & social sciences ☐ Ecological, evolutionary & environmental sciences

For a reference copy of the document with all sections, see nature.com/documents/nr-reporting-summary-flat.pdf

Life sciences study design

All studies must disclose on these points even when the disclosure is negative.

Sample size	Sample size for screening was selected to achieve at least 10-fold coverage of all possible single point mutations in the Archon1 scaffold. At 253 amino acids, there are ~5,000 single point mutations, leading to a screening population of at least 50,000. For patch clamp experiments and in vivo recordings, sample sizes were as large as could be practically attained.
Data exclusions	Recordings of non-spiking neurons were excluded from analysis.
Replication	For in vivo recordings, 2 or more animals were used in each experiment. Every replicate where the virus expressed and data were acquired was successful. Cases where there were problems with the surgery (no virus expression, cortical window falling off, animal died) did not lead to data acquisition.
Randomization	For comparisons between GEVI variants animals were selected at random to receive one GEVI treatment or the other.
Blinding	During the screen, the investigators were blind to the genotypes of the selected cells until after the selection was complete. For the in vivo experiments comparing GEVIs, blinding was not practical because the same person performed the surgery, data acquisition, and analysis.

Reporting for specific materials, systems and methods

We require information from authors about some types of materials, experimental systems and methods used in many studies. Here, indicate whether each material, system or method listed is relevant to your study. If you are not sure if a list item applies to your research, read the appropriate section before selecting a response.

Materials & experimental systems

n/a	Involved in the study
☐	☒ Antibodies
☐	☒ Eukaryotic cell lines
☒	☐ Palaeontology and archaeology
☐	☒ Animals and other organisms
☒	☐ Clinical data
☒	☐ Dual use research of concern

Methods

n/a	Involved in the study
☒	☐ ChIP-seq
☐	☒ Flow cytometry
☒	☐ MRI-based neuroimaging

Antibodies

Antibodies used	HA Tag recombinant rabbit monoclonal antibody (ThermoFisher, Clone RM305). Goat anti-Rabbit IgG (H+L) cross-adsorbed secondary antibody conjugated with Cy-5, ThermoFisher Cat# A10523.

Validation	This antibody was verified by the vendor via Western blot analysis against HE-H3-FLAG.

Eukaryotic cell lines

Policy information about cell lines and Sex and Gender in Research

Cell line source(s)	HEK293T ATCC CRL-3216;
Authentication	The cell line was validated by STR profiling at ATCC
Mycoplasma contamination	All cell lines were tested negative of mycoplasma
Commonly misidentified lines (See ICLAC register)	None

Animals and other research organisms

Policy information about studies involving animals; ARRIVE guidelines recommended for reporting animal research, and Sex and Gender in Research

Laboratory animals	Mice were C57BL/6 wild-type, NDNF-Cre+/- (JAX #028536), or PV-Cre+/- (JAX #017320). Acute slice patch clamp experiments were performed in mice of postnatal day 14 - 25. In vivo imaging experiments were performed in mice age 6 weeks - 8 months.
Wild animals	No wild animals were used in this study.
Reporting on sex	Mice of both sexes were used without regard to sex in this study.
Field-collected samples	No field-collected samples were used in this study.
Ethics oversight	All procedures involving animals were in accordance with the National Institutes of Health guide for the care and use of laboratory animals and were approved by the Institutional Animal Care and Use Committee at Harvard University.

Note that full information on the approval of the study protocol must also be provided in the manuscript.

Flow Cytometry

Plots

Confirm that:

☒ The axis labels state the marker and fluorochrome used (e.g. CD4-FITC).

☒ The axis scales are clearly visible. Include numbers along axes only for bottom left plot of group (a 'group' is an analysis of identical markers).

☒ All plots are contour plots with outliers or pseudocolor plots.

☒ A numerical value for number of cells or percentage (with statistics) is provided.

Methodology

Sample preparation	The samples were cell lines cultured in dishes. The cells were enzymatically dissociated from the culture dish and resuspended in phosphate saline buffer before sorting.
Instrument	BD FACS Aria Cell Sorters
Software	FCSExpress
Cell population abundance	in a typical run, the total number of cells ranged between 1E6 - 1E7. The target population to be recovered ranged from 1E3 - 1E4.
Gating strategy	Forward scatter (FSC) and side scatter (SSC) to find viable, single cell events. The gating thresholds are shown in Fig. 1d and Fig. 2f.

☒ Tick this box to confirm that a figure exemplifying the gating strategy is provided in the Supplementary Information.